NUMERICAL TECHNIQUES FOR NEAR-FIELD ACOUSTIC HOLOGRAPHY

A thesis by Nadia Mohamed Abusag submitted in partial fulfilment of the requirements of Nottingham Trent University for the degree of Doctor of Philosophy.

Department of Physics and Mathematics
Nottingham Trent University

September 2019

Copyright Statement

Contents

List of Figures

List of Tables

Abstract

Near-field acoustic holography (NAH) has proved to be an enormously successful sound source identification technique, which is widely used in field of acoustics and noise control. The work presented in this thesis aims at developing a novel method for modelling near-field acoustic holography, where the particle velocity on the surface of a vibrating structure is recovered from measurements taken in the exterior field. The model developed will form a powerful predictive tool for identifying sources of acoustic radiation for applications in mechanical and audio engineering.

Inspired by advances in the solution of ill-posed problems in imaging science using the so-called compressed sensing, we seek to develop new compressed or sparse reconstruction methods for the NAH problem. A sparse superposition method will be developed and implemented based on the inverse method of superposition (MoS), or equivalent source method as it is often known. The method should be able to reconstruct the normal velocity of a vibrating object using a very small number of charge points. Two primary reasons this is beneficial are; one can potentially reduce the amount of measured data required, and one could also detect sources of noise when small clusters of charge points are identified. The sparse inverse MoS will then be applied to reconstruct the surface velocity of a loudspeaker from measurements of the sound pressure field taken in a semi-anechoic chamber. The development of the new sparse inverse MoS and its experimental verification form the primary contributions to knowledge of this thesis.

Acknowledgements

First and foremost, thanks to God to whom my accomplishment is due.

I am grateful to the Libyan Government for the scholarship which enabled me to undertake a PhD program at the Nottingham Trent University.

I would like to express my deepest gratitude to my supervisor, Dr David Chappell, for his kind support and guidance to finish my PhD programme. His encouragement and detailed advice during the programme has been a good channel for me to have a successful completion of this research work.

I also wish to thank Dr Jonathan Hargreaves and Dr Rob Oldfield from the University of Salford for their hard work and support during the experimental work.

I have to thank my parents especially my father Dr Mohammed Abusag and my mother Aisha Abusag, and my children; Hawazen, Hagoud, Mohammed and Hajd for their love and support throughout my life. Thank you all for giving me strength to reach for the stars and chase my dreams.

There is one person I need to thank most of all whom I am truly and forever thankful; my husband Dr Tarek M. Eshahawi.

Declaration

I declare that the presented work in this thesis is the original work of the author except where explicitly stated otherwise in the text. I declare that this thesis as well as the materials contained in the thesis have not been used in any other submission for an academic award.

Parts of the work presented in the thesis have been published in:

Paper 1: Abusag N. M., Chappell D. J. On Sparse Reconstructions in Near-Field Acoustic Holography Using The Method of Superposition, Journal of Computational Acoustics, published 20 January 2016.

Paper 2: Chappell D.J., Abusag N.M. (2017) The Method of Superposition for Near-Field Acoustic Holography in a Semi-anechoic Chamber. In: Constanda C., Dalla Riva M., Lamberti P., Musolino P. (eds) Integral Methods in Science and Engineering, Volume 2. Birkhauser, Online ISBN 978-3-319-59387-6.

Chapter 1

General introduction

1.1 Introduction

The problem of Near-field Acoustic Holography (NAH) is to reconstruct the vibrational response of a structure from measurements of its radiated exterior acoustic field. The aim of the research presented in this thesis is to develop improved and novel methods for modelling NAH. The importance of such models arises in their application to inverse acoustics problems from mechanical, naval and audio engineering. In fact, we consider several methods to reconstruct the vibrations of an object's surface such as Fourier acoustics, inverse boundary element methods and the inverse Method of Superposition (MoS). Fourier methods are limited to specific geometries and the inverse boundary element method is complicated and requires a large number of measurement points to reconstruct the vibration of an object's surface with appropriate accuracy, which makes it difficult to apply in practice. The main aim will therefore be to find a practical method to model NAH with a relatively small number of measurement points, low computational overheads and reasonable accuracy.

The methodological approach taken to meet these aims will be based on the inverse MoS together with modern sparse regularisation procedures in order to achieve a relatively straightforward and efficient numerical method. We will demonstrate that for the forward Neumann boundary value problem associated to NAH, the MoS outperforms the boundary element method in terms of accuracy, requires far lower computational times and is simpler to implement due to not having to calculate singular integrals. In addition, the MoS shares the advantage of the boundary element method in terms of not being limited to simple geometrical settings like the Fourier based methods. Furthermore, the combination of the inverse MoS with sparse regularisation methods allows the reconstruction of the vibrational behaviour of a structure using relatively few degrees of freedom in the model and is also robust to reduced measurement data sets.

In Chapter 1, we will give a thorough literature review of numerical methods for near-field acoustic holography. The review includes several important points of reference, from the first study on NAH in the early eighties, until the present day state-of-the-art.

In Chapter 2, the boundary element method will be considered for the solution of the Helmholtz equation in an unbounded exterior domain. Then, a direct boundary integral representation of the solution will be detailed and followed by the numerical solution using the collocation method.

In Chapter 3, the concept of Fourier acoustics methods for solving the inverse problem of NAH will be described, and the vibrational behaviour of a structure will be reconstructed from acoustic pressure data in the near-field. Then, Fourier transforms and the convolution theorem will be applied to solve this integral equation for either the pressure or the Neumann data on the plate, given the acoustic pressure data in the near-field above the plate.

Chapter 4 will extend the methods in Chapter 2 to give a reformulation of the boundary integral equation for the Helmholtz equation, for solving the inverse problem of NAH. Reconstructions of the Neumann boundary data will then be computed on general three-dimensional structures, given noisy acoustic pressure data in the exterior domain.

Chapter 5 will describe the method of superposition (MoS) and its numerical application to solve both the forward Neumann problem, and the inverse NAH problem. The numerical results of using the MoS for the forward Neumann problem and for the inverse problem of NAH will be compared with the BEM results from Chapters 2 and 4, respectively.

In Chapter 6, the theory of compressive sampling, including the key concepts of sparsity and incoherence will be introduced. Then, the possibility of a sparse solution representation using ℓ^1 optimization techniques based on the method of superposition applied to three dimensional NAH problems will be discussed. The method of superposition based on compressive sampling will be applied to a cuboid that has similar dimensions to a typical loudspeaker.

In Chapter 7, the validity of the sparse inverse method of superposition for NAH presented in Chapters 5 and 6 will be verified by using measured pressure data for a loudspeaker in a semi-anechoic chamber. The final chapter will conclude our findings and propose several potential areas for further work.

1.2 Background

In the following sections we describe a number of different acoustics models and their applications, before focusing an our problem of interest, NAH. We then survey the current state-of-the-art numerical methods for the NAH problem.

1.2.1 Interior and exterior acoustic problems

A distinction can be made between interior and exterior acoustic problems. For interior problems the acoustic waves are reflected in an enclosure resulting in a sound field which is dominated by resonant behaviour (for example, noise inside an engine). On the contrary, when an object radiates sound into an unconfined free space, the problem is described as an exterior problem (for example, noise radiation from an aircraft). The study of near-field acoustic holography is classed as an exterior problem since it is based on measurements of a sound field taken in an anechoic chamber, and hence the experimental set-up is designed to replicate an unbounded exterior domain [1].

Exterior acoustic problems can be divided into two main types: scattering problems and radiation problems. In scattering problems, the acoustic wave impinges on an object (or scatterer) and the acoustic characteristics of the scattered sound field have to be determined. On the other hand, in radiation problems a non-zero boundary condition on the surface of the object is prescribed and the resulting acoustic field has to be predicted. Near-field acoustic holography falls under the category of a radiation problem, since the acoustic field originates from the object and not from an incident external wave field.

1.2.2 Forward and inverse problems in acoustics

In a forward problem, the solution process involves finding effects based on a complete description of their causes. An inverse problem involves the determination of the unknown causes based on the observation of their effects. The exterior acoustic radiation problem belongs to the class of forward problems because the cause is prescribed (that is the vibration of a structure) and the effects (the sound field) have to be determined. The inverse problem associated with the exterior acoustic

radiation problem is precisely the problem encountered in NAH [2]. In this problem we take measurements of the radiated exterior acoustic field (the effect) and from this we seek to determine the structural vibrations that created this measured field.

1.2.3 Near-field acoustic holography

Near-field acoustic holography has proved to be an enormously useful sound source identification technique, and is widely used in the fields of acoustics and noise control [3]. The first numerical techniques for NAH were developed by Williams and Maynard [1]. In general, acoustic holography involves measuring the sound pressure and analysing the field radiated from an object [4]. Traditionally, measurements were taken on a hologram plane facing a vibrating plate [1], but nowadays a conformal surface is often used for more general geometries [5].

Noise and vibration issues are of great interest across a number of industrial sectors, including automotive, aircraft and home appliance manufacturers. Improving the noise and vibration performance of a product requires a diagnosis of the root causes of any undesirable noise and vibration, as well as knowledge of their interrelationships. A common approach is to scan a structure using a sound intensity probe to identify any regions of significantly high acoustic energy in the surrounding fluid medium [38]. According to Wu [6], the advantage of NAH is that it enables us reconstruct all acoustic quantities, at any point in space and on the source surface, by measuring the acoustic pressure in the near field of the radiating source surface.

This research will focus on developing numerical methods for reconstructing the acoustic field on a radiating structure, such as loudspeaker or an automotive

engine. The normal velocity on the surface and hence the surface pressure can be reconstructed, and from this the acoustic intensity may be calculated. The acoustic intensity is of interest since it gives more information about the acoustic field than the pressure alone. For example, the radiating part of a field can be separated from the reactive part. In this work we focus mainly on reconstructing the normal velocity on the surface, assuming that the surface geometry is known.

1.2.4 Fourier based NAH

Fourier acoustics based NAH uses an acoustic double layer potential to represent the sound radiated from a two-dimensional planar region. Since the double layer potential is essentially the convolution of the normal derivative of the half-space Green's function with the acoustic pressure in the two-dimensional planar region, the latter quantity may be recovered by using Fourier transforms and the convolution theorem. More detail is given in Chapter 3.

Fourier methods were the first numerical techniques to be developed for solving the NAH problem [7]. Note that unlike the other methods discussed in this chapter, Fourier methods are not themselves numerical approximation methods. However, since the reconstructions are based on discrete and finite data sets, then the discrete Fourier transform is used to approximate the Fourier (and inverse Fourier) transform, and in that respect we consider these Fourier methods to be numerical techniques. The acoustic pressure at any point in a source free region can be reconstructed by taking the inverse Fourier transform to obtain the acoustic pressure in the space frequency domain on the two-dimensional planar region. The particle velocity can be reconstructed in a similar way through a different propagator, see Section 3.3.2. Once the acoustic pressure and the particle velocity are reconstructed, the acoustic intensity can be specified. Therefore, once the

acoustic pressure on a hologram surface is measured, then all the other acoustic quantities can be determined [1,8]. Theoretically, the measurement (or hologram) plane must be of infinite extent and without the presence of any other source or boundary surface. However, in reality, such a source free region is non-existent.

In later work, variations of NAH, such as patch NAH have been developed by Williams [9], where measurements are only required on a small region of the total surface. However, the reconstruction accuracy would deteriorate using patch NAH, unless the acoustic field was null away from the patch. In addition, acoustically radiating manufactured structures are rarely as geometrically simple as a planar surface and so Fourier based NAH is limited in its range of applications. Whilst Fourier based NAH can also be applied to separable geometries in other coordinate systems, such as spheres and cylinders, alternative technologies are usually needed to apply NAH to more general structures.

1.2.5 Boundary element method

Numerical approximation methods enable the simulation of sound fields for a wide variety of geometries and boundary conditions. In the low and medium frequency ranges two important methods exist: the Finite Element Method (FEM) and the Boundary Element Method (BEM). Whereas FEM involves numerically solving a differential equation (for example, the Helmholtz equation), the BEM uses a boundary integral formulation as its basis [10]. To reach a reasonable accuracy, a sufficient number of nodes per acoustic wavelength is required for both the BEM and the FEM. Since the wavelength shortens with increasing frequency, the number of elements must increase accordingly to maintain the same level of accuracy. For this reason, these element based approaches are restricted to low and medium frequency applications.

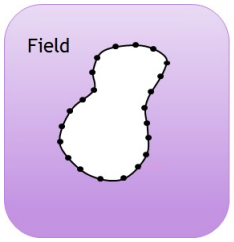

(a) Exterior problem.

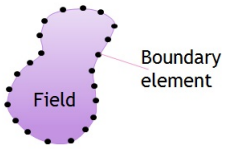

(b) Interior problem.

Figure 1.1: Interior and exterior domain modelling using boundary element methods.

Pederson and Munch [11], and Hodgson and Underwood [12] have applied the BEM to solve a wide range of practical problems in acoustics, such as the modelling of sound generated by loudspeakers or received by microphones [13]. The BEM approach was also adapted by Chandler-Wilde *et al.* [14] to achieve accurate approximations at high frequencies with a relatively low number of degrees of freedom.

Boundary element methods are naturally suited to modelling unbounded domains since they only require the discretization of a finite boundary surface to obtain a solution anywhere in the unbounded domain (see Fig. 1.1). Not only does this reduce the dimensionality of the problem considered by one, but it also eradicates the need for the application of non-reflecting boundary conditions required in full domain discretisation methods such as the finite element and finite difference methods [15–17]. Along with the fact that simple expressions for the fundamental solution are well-known, these factors make the BEM a popular tool for exterior acoustic problems.

The inverse boundary element method (IBEM) is the boundary element method applied to solve the inverse problem of NAH [6]. The IBEM was the first technique for modelling NAH problems with arbitrary geometries. In 1988, Gardner and Bernard [18] applied the IBEM to reconstruct vibroacoustic quantities on an arbitrarily shaped structure. A large number of articles on IBEM have since been published, including [19,20]. More recently the IBEM has been combined in hybrid methods, which use particular solutions of the Helmholtz equation to enrich the measured data [21, 22].

The IBEM has a number of advantages for NAH simulations, including its versatility for general geometries, measurement point locations and solution point locations [6]. However, difficulties can arise at higher frequencies as for the forward BEM discussed above. Another potential difficulty that the IBEM also inherits from the forward BEM is that in their simplest (and most tractable) form, the integral equations for the exterior problem do not have a unique solution at the resonance frequencies of the associated interior problem. This is in contrast with the Helmholtz equation description of the exterior problem, which does have a unique solution [23, 24]. More complex methods and integral equation formulations, such as the Burton and Miller formulation can be used in order to obtain an accurate solution in the vicinity of these problematic frequencies [2]. One further deficiency of the IBEM is that the integral representation of the sound pressure is near singular when the measurement points are taken very close to the surface element to be integrated over. For the forward BEM, this would only affect the accuracy in the very near field [25], but for the application of the IBEM to NAH it imposes a limitation on how close the measurement points can be to the radiating structure.

1.2.6 Basis approximation methods

A number of alternative methods to the IBEM have since been proposed for the numerical solution of NAH problems with arbitrary geometries. These methods effectively fit the measured pressure data to a linear combination of basis functions, and then use the coefficients determined through this approximation to determine the normal velocity of the vibrating object. The most well-known of these methods with respect to NAH are the Helmholtz equation least squares (HELS) method proposed by Sean Wu and co-workers [26, 27] and the method of superposition, which was applied to NAH in Refs. [28, 29], including a comparison against boundary element approaches in the latter case. For HELS, the basis functions are chosen as particular solutions to the Helmholtz equation in an idealized domain, typically a sphere. In the case of the superposition method then it is the free space Green's functions that are usually employed for the basis.

It is shown in Ref. [30] that the superposition method for an exterior acoustic problem is equivalent to the Helmholtz integral equation. This is one reason for favouring the superposition approach to HELS, where the chosen basis is typically only complete outside the minimum sphere enclosing the radiating object [27]. This would be a drawback for approximating near-field radiation from objects that are far from spherical. Koopman *et al.* [30] also argue that the superposition method will not suffer from the same irregular frequency problem as the boundary element method since the set of source points chosen for the superposition (after truncating the superposition integral to a finite sum) will not form a unique boundary surface inside the interior volume. However, the computations in Ref. [30] were only performed with small numbers of source points, and irregular frequency problems may arise should the source points more closely represent an interior boundary surface [31, 32].

One of the main challenges involved in the superposition method is obtaining an optimal choice of source (or charge) points over which to compute the superposition. In particular, research on (forward) interior Helmholtz problems [33] suggests that the source points should be chosen close to the radiating surface so that no singularities of the analytically continued solution lie between the charge points and the radiating surface. However, for the exterior problem, Koopman *et al.* [30] report that choosing the charge points too close to the radiating surface degrades the accuracy of the method, whilst choosing charge points too far from the surface leads to very poor conditioning. Applying the superposition method together with a nonlinear optimization algorithm to optimise the accuracy of the solution over both the charge point strengths and locations is known as the method of fundamental solutions, see for example Refs. [34, 35]. For NAH problems, the charge points are typically chosen as the reflection of the measurement points with respect to the radiating surface [28, 29].

1.2.7 Regularisation

Near-field acoustic holography provides an example of a linear, ill-posed inverse problem due to the existence of evanescent waves that decay rapidly as the distance from the vibrating structure is increased. After discretisation, the problem is reduced to the solution of an ill-conditioned linear system of the form $A\mathbf{x} = \mathbf{b}$. The goal of regularisation methods is to prevent the solution $\mathbf{x}$ from becoming dominated by contributions arising due to noise in the vector $\mathbf{b}$, which typically come from experimental error/noise in NAH. An overview of regularization techniques for NAH is given by Williams in Ref. [36].

A number of regularisation techniques are available for linear inverse problems such as NAH. However, many regularisation schemes, from a practical point of

view, produce the same regularised solutions [37]. Two of the most commonly used methods are the truncated singular value decomposition (SVD) and Tikhonov regularization [36]. Both methods rely on the careful choice of a particular parameter value. In the truncated SVD it is the value of the minimum singular value that should be included in the SVD. For Tikhonov regularization it is the value of the regularisation parameter λ, where instead of $A\mathbf{x} = \mathbf{b}$ we are solving the perturbed linear system

$$\left(A^T A + \lambda^2 L^T L\right)\mathbf{x} \; = A^T \mathbf{b}. \tag{1.1}$$

Here L is known as the Tikhonov matrix, which is most simply taken to be the identity matrix. This is a sound choice when no further information is known about the solution of the unperturbed system (when $\lambda = 0$). Tikhonov regularisation is intrinsically connected to the SVD, and its effect is to filter the smaller singular values to suppress their contribution, rather than to cut them off entirely as in the truncated SVD. A number of methods for choosing the parameter λ exist and are surveyed by Williams in [36]. The best selection method is an open and problem dependent question. For Fourier based NAH, Williams [36] suggests to use generalised cross validation (GCV), which is statistical technique for approximately minimising the mean square error. Hansen [37] suggests to plot the norm of $L\mathbf{x}$ against the norm of the residual $A\mathbf{x} - \mathbf{b}$, for a range of λ values. The plot is known as the L-curve and often has a distinctive corner, where the two norms are approximately minimised, and hence gives the optimum choice of λ. Whilst this process could be computationally expensive for large system, typically this is not a problem for NAH where the size of the system is constrained by the size of the measurement data obtained. Another common method for choosing λ is the Morozov discrepancy principle, however this technique requires prior knowledge of the variance of the noise in the vector $\mathbf{b}$. Therefore, we do not discuss it further here, since in NAH such information is typically not known.

1.2.8 Sparse regularization using compressed sensing

Compressed sensing (CS) was first introduced in 2006 by two groundbreaking papers by Donoho [38] and Candés *et al.* [39]. It is now a widely accepted method that enables a potentially large reduction in the sampling and computation data for sensing signals that have a sparse or compressible representation [40]. Compressed sensing was first applied to NAH problems using a plane wave basis by Chardon *et al.* [41]. They applied compressed sensing based on the sparsity of the normal velocity for convex homogeneous plates with arbitrary boundary conditions to identify the vibrating sources. The results demonstrate that there is potential to reconstruct sparse signals with a small number of measurements and high accuracy. These methods are also related to Tikhonov regularisation as discussed in [41], and the main difference arises from the choice of norm to be minimised. Tikhonov regularisation is based on ℓ^2 norm minimisation, whereas sparse methods seek to minimise ℓ^1 norms.

Over the last few years, a number of publications on compressed sensing for NAH problems have emerged, which use the inverse method of superposition to reconstruct the vibrations of an acoustically radiating structure [42, 43]. The first of these papers, by Jorgen Hald, introduced the wideband acoustical holography method, which makes use of compressed sensing principles [43]. In Ref. [43], wideband acoustical holography was tested on a vibrating plate and successfully located and quantified the main sources of noise.

More recently, CS theory has been applied with the inverse method of superposition to 2D and 3D radiating objects [44, 45]. Fernandez-Grande and Xenaki proposed a wave expansion method, based on measurements with a spherical microphone array, formulated in the framework provided by compressed sensing [46]. Hald also expanded his wideband acoustical holography method to represent the sound field in a given three-dimensional region, with measurements taken using

an irregular two-dimensional array [47]. Active research in this area is ongoing and new sparse methods are frequently being developed, such as the compressed modal equivalent point source method (CMESM) proposed by Bi *et al.* [48], and the improved source optimisation methods recently proposed by Hald [49].

1.3 Summary

In this chapter, we considered the general concept of interior and exterior problems in acoustics and discussed the nature of the problem of NAH as an inverse exterior acoustic problem. We also discussed some numerical techniques for NAH problems, starting with the first technique, Fourier acoustics based NAH. Then we discussed more recent developments, such as the inverse boundary element method, which can be applied to solve the inverse problem of NAH for general geometries. We then detailed a number of approaches that can be described as basis approximation methods. These methods can be used to gain more efficient numerical solutions and shorter computational times. Finally, we discussed regularisation techniques such as the truncated singular value decomposition, Tikhonov regularization and sparse reconstruction methods.

Chapter 2

Exterior acoustic modelling and the boundary element method

2.1 Introduction

In this chapter we present a summary of the boundary element method (BEM) for the solution of the Helmholtz equation in an unbounded exterior domain. We derive a direct boundary integral representation of the solution and discuss its numerical solution via the collocation method. The derived boundary integral representation will also be important for the subsequent chapters on Fourier acoustics based NAH (Chapter 3), as well as the inverse boundary element method based NAH described in Chapter 4. We describe a singularity subtraction method for evaluating the weakly singular integrals that are present in the boundary integral equations, before finally providing some numerical results to demonstrate the capability of the method.

Let $\Omega_- \subset \mathbb{R}^3$ be a domain in $\mathbb{R}^3$, interior to the boundary surface Γ where we assume that Γ is continuous and piecewise C^2. Also, let $\Omega_+ = \mathbb{R}^3 \setminus \bar{\Omega}_-$ denote

the unbounded exterior domain, which is assumed to be filled with a homogeneous compressible acoustic medium with density ρ and speed of sound c.

It is well known that acoustic waves of small amplitude propagate through Ω_+ according to the linear wave equation [50]

$$\triangle\Phi(\mathbf{x},t) = \frac{1}{c^2}\frac{\partial^2\Phi(\mathbf{x},t)}{\partial t^2}, \tag{2.1}$$

where $\Phi(\mathbf{x},t)$ is the excess pressure at $\mathbf{x} \in \Omega_+$ and time t. We require all radiated waves to be outgoing at infinity and this can be expressed by the following radiation condition

$$\lim_{R\to\infty} R\left\{\frac{\partial\Phi}{\partial R} + \frac{1}{c}\frac{\partial\Phi}{\partial t}\right\} = 0, \tag{2.2}$$

where R is the distance from $\mathbf{x}$ to a fixed origin $\mathbf{y} \in \Gamma$, i.e. $R = |\mathbf{x} - \mathbf{y}|$.

In this chapter we assume that $\Phi(\mathbf{x},t)$ has harmonic time dependence with a constant frequency f. This means that we can write $\Phi(\mathbf{x},t) = \phi(\mathbf{x})e^{-i\omega t}$, where $\omega = 2\pi f$ is the angular frequency and $\phi(\mathbf{x})$ is the amplitude of Φ at $\mathbf{x} \in \Omega_+$. Substituting this into (2.1) we obtain the Helmholtz' (or reduced wave) equation

$$\triangle\phi(\mathbf{x}) + k^2\phi(\mathbf{x}) = 0, \qquad \mathbf{x} \in \Omega_+ \tag{2.3}$$

where $k := \omega/c$ is called the acoustic wavenumber. Applying the same (time harmonic) substitution to (2.2), we obtain the Sommerfeld radiation condition

$$\lim_{R\to\infty} R\left\{\frac{\partial\phi}{\partial R} - ik\phi\right\} = 0. \tag{2.4}$$

We also require a boundary condition on Γ and together with (2.3) and (2.4) this defines the governing boundary value problem (BVP) for our exterior acoustic

problem. We assume this boundary condition is one of the following:

$$\begin{aligned}
&\text{(a)} \quad \phi(\mathbf{x}) = f(\mathbf{x}) \quad \mathbf{x} \in \Gamma && \text{(Dirichlet condition)} \\
&\text{(b)} \quad \frac{\partial \phi(\mathbf{x})}{\partial \hat{\mathbf{n}}} = f(\mathbf{x}) \quad \mathbf{x} \in \Gamma && \text{(Neumann condition)} \\
&\text{(c)} \quad \frac{\partial \phi(\mathbf{x})}{\partial \hat{\mathbf{n}}} + h(\mathbf{x})\phi(\mathbf{x}) = f(\mathbf{x}) \quad \mathbf{x} \in \Gamma && \text{(Robin condition),}
\end{aligned} \tag{2.5}$$

where the functions $f, h : \Gamma \to \mathbb{C}$ are known and $\hat{\mathbf{n}}$ is the outward unit normal to Ω_-. The existence and uniqueness of solutions to the BVP (2.3, 2.4, 2.5) given $\mathrm{Re}(k) > 0$ and $\mathrm{Im}(k) \geq 0$ are shown in [24, 51] for (2.5 (a) and (b)). It is also shown for the Robin case in [24] for functions h such that either $\mathrm{Im}(h) > 0$, or $\mathrm{Im}(h) > \dfrac{\mathrm{Im}(k)}{\mathrm{Re}(k)}\mathrm{Re}(h)$. The remainder of this chapter considers how we can use the BEM to numerically solve the exterior acoustic BVP.

2.2 The surface Helmholtz integral equation

There are two methods commonly used to reformulate the above BVP into an integral equation, either indirectly using layer potentials or directly using Green's identities. The indirect formulations are so-called because the resulting integral equation is not solved for a field quantity such as ϕ or $\partial\phi/\partial\hat{\mathbf{n}}$, but for a quantity called a layer density, which in general has no physical significance (see [23] for further details). Since our eventual aim is to model real applications using experimentally obtained data, it would be preferable to obtain a field quantity from our solution which would have some physical meaning. We proceed using the direct formulation for precisely this reason.

We begin by considering the first two Green's identities in three dimensions [52]. We adopt the notation dV to denote a volume integral and $d\Gamma$ to denote a surface integral.

Theorem 2.1 *Green's first identity for the Laplace operator.*

Let $V \in \mathbb{R}^3$ be a domain with closed boundary surface $\Sigma = \partial V$ and let $\phi_1, \phi_2 : V \to \mathbb{C}$ be C^2 functions, then

$$\int_V (\phi_1 \triangle \phi_2 + \nabla \phi_1 \cdot \nabla \phi_2)\, dV = \int_\Sigma \phi_1 \frac{\partial \phi_2}{\partial \hat{\mathbf{n}}} d\Gamma. \tag{2.6}$$

Proof.

Consider the following easily verified identity

$$\phi_1 \triangle \phi_2 + (\nabla \phi_1) \cdot (\nabla \phi_2) = \nabla \cdot (\phi_1 \nabla \phi_2).$$

Integrating over V we obtain

$$\int_V (\phi_1 \triangle \phi_2 + \nabla \phi_1 \cdot \nabla \phi_2)\, dV = \int_V \nabla \cdot (\phi_1 \nabla \phi_2) dV,$$

and so applying Gauss' divergence theorem to the right hand side gives

$$\int_\Sigma (\phi_1 \nabla \phi_2) \cdot \hat{\mathbf{n}}\, d\Gamma = \int_\Sigma \phi_1 (\nabla \phi_2 \cdot \hat{\mathbf{n}})\, d\Gamma.$$

□

Corollary 2.1 *Green's second identity for the Laplace operator.*

Let V, Σ, ϕ_1 and ϕ_2 be as above, then

$$\int_V (\phi_1 \triangle \phi_2 - \phi_2 \triangle \phi_1)\, dV = \int_\Sigma \left(\phi_1 \frac{\partial \phi_2}{\partial \hat{\mathbf{n}}} - \phi_2 \frac{\partial \phi_1}{\partial \hat{\mathbf{n}}} \right) d\Gamma. \tag{2.7}$$

Proof.

Immediate by interchanging ϕ_1 and ϕ_2 in the first identity, then subtracting this from (2.6) and using the symmetry of the scalar product.

□

We cannot apply this result directly on the unbounded exterior region Ω_+ and so we apply it on the region $\mathbb{B}_R \setminus \Omega$ where $\mathbb{B}_R$ is a closed ball of radius R centered at the origin such that $\Omega \subset \mathbb{B}_R$. We set $\phi_1 = \phi$ and $\phi_2 = G_k$, where ϕ is the solution we require from our BVP (2.3, 2.4, 2.5) and G_k is the free space Green's function (or fundamental solution) for Helmholtz' equation in three dimensions given by

$$G_k(\mathbf{x}, \mathbf{y}) = \frac{e^{ik|\mathbf{x}-\mathbf{y}|}}{4\pi|\mathbf{x}-\mathbf{y}|}. \tag{2.8}$$

This means that G_k satisfies

$$\triangle G_k(\mathbf{x}, \mathbf{y}) + k^2 G_k(\mathbf{x}, \mathbf{y}) = -\delta(\mathbf{x}-\mathbf{y}) \tag{2.9}$$

in both variables and the radiation condition (2.4), where δ denotes the Dirac delta function. Physically $G_k(\mathbf{x}, \mathbf{y})$ represents the effect at $\mathbf{y}$ of a unit point source at $\mathbf{x}$ radiating into free-space. Substituting all this into (2.7) we obtain

$$\int_{\mathbb{B}_R \setminus \Omega} (\phi \triangle G_k - G_k \triangle \phi)\, dV = \int_{\Gamma \cup \Sigma_R} \left(\phi \frac{\partial G_k}{\partial \hat{\mathbf{n}}} - G_k \frac{\partial \phi}{\partial \hat{\mathbf{n}}} \right) d\Gamma, \tag{2.10}$$

where $\Sigma_R = \partial \mathbb{B}_R$. Since $\Gamma \cap \Sigma_R = \emptyset$, the union we are integrating over is disjoint and so we can write the RHS of (2.10) as the sum of two integrals with the same integrand, one over Γ and one over Σ_R. Taking the limit $R \to \infty$, $\mathbb{B}_R \setminus \Omega$ becomes Ω_+ and using the radiation condition (2.4) we can show the integral over Σ_R is zero. This follows immediately from the fact that we can rewrite this integral as

$$\int_{\Sigma_R} \left(\phi(\mathbf{y}) \left[\frac{\partial G_k(\mathbf{x}, \mathbf{y})}{\partial \hat{\mathbf{n}}_\mathbf{y}} - ikG_k(\mathbf{x}, \mathbf{y}) \right] - G_k(\mathbf{x}, \mathbf{y}) \left[\frac{\partial \phi(\mathbf{y})}{\partial \hat{\mathbf{n}}_\mathbf{y}} - ik\phi(\mathbf{y}) \right] \right) d\Gamma_\mathbf{y}, \tag{2.11}$$

where $d\Gamma_\mathbf{y}$ and $\hat{\mathbf{n}}_\mathbf{y}$ denote that the surface integral and the outward unit normal taken with respect to the point $\mathbf{y} \in \Sigma_R$ respectively. Hence we are left with

$$\begin{aligned} &\int_{\Omega_+} (\phi(\mathbf{y}) \triangle G_k(\mathbf{x}, \mathbf{y}) - G_k(\mathbf{x}, \mathbf{y}) \triangle \phi(\mathbf{y}))\, dV_\mathbf{y} = \\ &\int_\Gamma \left(\phi(\mathbf{y}) \frac{\partial G_k(\mathbf{x}, \mathbf{y})}{\partial \hat{\mathbf{n}}_\mathbf{y}} - G_k(\mathbf{x}, \mathbf{y}) \frac{\partial \phi(\mathbf{y})}{\partial \hat{\mathbf{n}}_\mathbf{y}} \right) d\Gamma_\mathbf{y}. \end{aligned} \tag{2.12}$$

Using Helmholtz' equation (2.3) we can rewrite the volume integral as

$$\int_{\Omega_+} \phi(\mathbf{y}) \left(\triangle G_k(\mathbf{x}, \mathbf{y}) + k^2 G_k(\mathbf{x}, \mathbf{y}) \right) dV_{\mathbf{y}}. \tag{2.13}$$

The position of the point $\mathbf{x}$ dictates the value of (2.13). If $\mathbf{x} \in \Omega_-$, then G_k satisfies Helmholtz' equation and so (2.13) is just zero. If $\mathbf{x} \in \Omega_+$, then G_k is singular when $\mathbf{x} = \mathbf{y}$ and so we do not satisfy the assumptions needed for the use of Green's identities. However, we can avoid this singularity by taking a closed ball $\mathbb{B}_\varepsilon(\mathbf{x})$ with radius ε, centre $\mathbf{x}$ and boundary surface Σ_ε. We then integrate over the remaining volume and this gives an extra integration over Σ_ε. Taking the limit as $\varepsilon \to 0$ we obtain [51]

$$\int_{\Omega_+} \phi(\mathbf{y}) \left(\triangle G_k(\mathbf{x}, \mathbf{y}) + k^2 G_k(\mathbf{x}, \mathbf{y}) \right) dV_{\mathbf{y}} = \phi(\mathbf{x}), \qquad \mathbf{x} \in \Omega_+. \tag{2.14}$$

If $\mathbf{x} \in \Gamma$ we use a similar procedure as for the exterior case except that now we take the exterior part of the closed ball centered at $\mathbf{x}$ with radius ε. Assuming that Γ is locally differentiable at $\mathbf{x}$ (this will be true at all but a finite number of points by our assumption earlier), Σ_ε becomes a hemisphere when ε is sufficiently small and taking the limit as $\varepsilon \to 0$ gives [51]

$$\int_{\Omega_+} \phi(\mathbf{y}) \left(\triangle G_k(\mathbf{x}, \mathbf{y}) + k^2 G_k(\mathbf{x}, \mathbf{y}) \right) dV_{\mathbf{y}} = \frac{1}{2}\phi(\mathbf{x}), \qquad \mathbf{x} \in \Gamma. \tag{2.15}$$

Combining (2.12), (2.13), (2.14) and (2.15) gives the Helmholtz integral formula for the exterior problem

$$\int_\Gamma \left(\phi(\mathbf{y}) \frac{\partial G_k(\mathbf{x}, \mathbf{y})}{\partial \hat{\mathbf{n}}_{\mathbf{y}}} - G_k(\mathbf{x}, \mathbf{y}) \frac{\partial \phi(\mathbf{y})}{\partial \hat{\mathbf{n}}_{\mathbf{y}}} \right) d\Gamma_{\mathbf{y}} = \begin{cases} 0 & \mathbf{x} \in \Omega_- \\ \frac{1}{2}\phi(\mathbf{x}) & \mathbf{x} \in \Gamma \\ \phi(\mathbf{x}) & \mathbf{x} \in \Omega_+. \end{cases} \tag{2.16}$$

In the case of $\mathbf{x} \in \Gamma$ we can rewrite (2.16) in the form

$$-\frac{1}{2}\,\phi(\mathbf{x}) + \int_\Gamma \phi(\mathbf{y}) \frac{\partial G_k(\mathbf{x}, \mathbf{y})}{\partial \hat{\mathbf{n}}_{\mathbf{y}}} d\Gamma_{\mathbf{y}} = \int_\Gamma G_k(\mathbf{x}, \mathbf{y}) \frac{\partial \phi(\mathbf{y})}{\partial \hat{\mathbf{n}}_{\mathbf{y}}} d\Gamma_{\mathbf{y}}, \tag{2.17}$$

which is commonly referred to as the surface Helmholtz' equation (SHE). If we assume that we have a Neumann boundary condition, then (2.17) is a second-kind Fredholm integral equation for ϕ. This is the case we will consider in our test problems, since it is the forward problem associated with the inverse problem of NAH. Note that both G_k and $\frac{\partial G_k}{\partial \hat{\mathbf{n}}_\mathbf{y}}$ have a weak singularity at $\mathbf{x} = \mathbf{y}$ and so the integrals in (2.17) will need to be evaluated using appropriate quadrature rules.

2.3 Discretisation using the collocation method

In order to solve equation (2.17) numerically we represent the boundary Γ as a triangulated surface consisting of d_n flat three-noded triangles (linear surface interpolation). The solution function ϕ is approximated by

$$\phi(\mathbf{y}) = \sum_{j=1}^{n} \phi_j \psi_j(\mathbf{y}), \tag{2.18}$$

where $\psi_1(\mathbf{y})$, $\psi_2(\mathbf{y})$,... , $\psi_n(\mathbf{y})$ are set of known basis functions and $\phi_1, \phi_2, ...\phi_n$ are set of constants to be determined. Likewise, the normal derivative of ϕ can be approximated using the same basis in the form

$$\frac{\partial \phi(\mathbf{y})}{\partial \hat{\mathbf{n}}} = \sum_{j=1}^{n} v_j \psi_j(\mathbf{y}). \tag{2.19}$$

The simplest collocation scheme to implement is based on a piecewise constant approximation. Denote the d_n triangular sub-surfaces that form Γ as $T_1, ..., T_{d_n}$ and define the basis functions to be

$$\psi_j(\mathbf{y}) = \begin{cases} 1 & \text{if } \mathbf{y} \in T_j \\ 0 & \text{otherwise} \end{cases} \qquad j = 1, ..., d_n. \tag{2.20}$$

In the case of the piecewise constant basis functions above then note that $d_n = n$ since we have exactly one unknown per triangle.

Substituting the piecewise constant basis functions (2.20) and equations (2.18) and (2.19) into equation (2.17) yields

$$\frac{1}{2}\sum_{j=1}^{n}\phi_j\psi_j(\mathbf{x}) = \sum_{j=1}^{n}\int_{T_j}\psi_j(\mathbf{y})\left(\frac{\partial G_k}{\partial \hat{\mathbf{n}}_y}(\mathbf{x},\mathbf{y})\ \phi_j - G_k(\mathbf{x},\mathbf{y})\ v_j\right)d\Gamma_{\mathbf{y}}. \tag{2.21}$$

Since we integrate over T_j, then $\mathbf{y} \in T_j$ and so $\psi_j(\mathbf{y}) = 1$. This means that equation (2.21) can be simplified to

$$\frac{1}{2}\sum_{j=1}^{n}\phi_j\psi_j(\mathbf{x}) = \sum_{j=1}^{n}\int_{T_j}\left(\frac{\partial G_k}{\partial \hat{\mathbf{n}}_{\mathbf{y}}}(\mathbf{x},\mathbf{y})\ \phi_j - G_k(\mathbf{x},\mathbf{y})\ v_j\right)d\Gamma_{\mathbf{y}}, \tag{2.22}$$

where ϕ_j, $j = 1, ..., n$, are unknown, and v_j are provided by the Neumann boundary data.

We move the unknowns to the right and evaluate the solution at the collocation points

$$\mathbf{x} = \mathbf{x}_i \in T_i, \quad i = 1, ..., n.$$

For a piecewise constant basis, the collocation points $\mathbf{x}_i$, $i = 1, ..., n$, are usually taken to be the centroids of the triangles T_i. Making this choice, equation (2.22) can be rewritten as follows

$$\sum_{j=1}^{n} v_j \int_{T_j} G_k(\mathbf{x}_i,\mathbf{y})d\Gamma_{\mathbf{y}} = -\frac{1}{2}\sum_{j=1}^{n}\phi_j\psi_j(\mathbf{x}_i) + \sum_{j=1}^{n}\phi_j\int_{T_j}\frac{\partial G_k(\mathbf{x}_i,\mathbf{y})}{\partial \hat{\mathbf{n}}_{\mathbf{y}}}\ d\Gamma_{\mathbf{y}}\ . \tag{2.23}$$

Finally, we note that because $\psi_j(\mathbf{x}_i) = 0$ unless $i = j$, then

$$\sum_{j=1}^{n} v_j \int_{T_j} G_k(\mathbf{x}_i,\mathbf{y})\ d\Gamma_{\mathbf{y}} = -\frac{1}{2}\ \phi_i + \sum_{j=1}^{n}\phi_j\int_{T_j}\frac{\partial G_k(\mathbf{x}_i,\mathbf{y})}{\partial \hat{\mathbf{n}}}\ d\Gamma_{\mathbf{y}}. \tag{2.24}$$

To solve equation (2.24), we can write it as a matrix-vector equation by setting

$$\begin{aligned} K_{ij} &= \int_{T_j}\frac{\partial G_k}{\partial \hat{\mathbf{n}}_y}(\mathbf{x}_i,\mathbf{y})\ d\Gamma_{\mathbf{y}}, \\ V_{ij} &= \int_{T_j} G_k(\mathbf{x}_i,\mathbf{y})\ d\Gamma_{\mathbf{y}}\ . \end{aligned} \tag{2.25}$$

Hence, Eq. (2.24) may be written in the matrix-vector form

$$V\mathbf{v} = \left(-\tfrac{1}{2}\, I + K\right) \boldsymbol{\phi}, \tag{2.26}$$

where I is the $n \times n$ identity matrix and $\boldsymbol{\phi}$ and $\mathbf{v}$ are vectors of length n given by $\boldsymbol{\phi} = [\phi_1, \phi_2, ..., \phi_n]^T$ and $\mathbf{v} = [v_1, v_2, ..., v_n]^T$, respectively.

2.3.1 Weakly singular integration

We now consider methods for evaluating weakly singular integrals since the second integral (V_{ii}) in Eq. (2.25) has a weak singularity when $\mathbf{y} = \mathbf{x}_i$. If the collocation point is in a different triangle to the one we integrate over, then the integrals are non-singular and so they can easily be evaluated numerically. However, when the collocation point is in the same triangle that we integrate over, then $i = j$ and we have a weak singularity.

In the case of the integral in the definition of K_{ii}, the integrand evaluates to zero on a flat surface since

$$\frac{\partial G_k}{\partial \hat{\mathbf{n}}_\mathbf{y}} = \frac{\partial R}{\partial \hat{\mathbf{n}}_\mathbf{y}} \frac{\partial G_k}{\partial R},$$

where $R = |\mathbf{x}_i - \mathbf{y}|$. On a flat surface

$$\frac{\partial R}{\partial \hat{\mathbf{n}}_\mathbf{y}} = \hat{\mathbf{n}}_\mathbf{y} \cdot \nabla_\mathbf{y} R = 0$$

since

$$\nabla_\mathbf{y} R = \frac{1}{R}(\mathbf{y} - \mathbf{x}_i),$$

and $\hat{\mathbf{n}}_\mathbf{y}$ and $(\mathbf{y} - \mathbf{x}_i)$ are orthogonal vectors. This is because $T_i, i = 1, 2, ..., n$ are flat triangles and the vector $(\mathbf{y} - \mathbf{x}_i)$ lies in the same plane as T_i.

In the case of the integral in the definition of V_{ii} in equation (2.25), we adopt a singularity subtraction technique and rewrite V_{ii} as

$$V_{ii} = \int_{T_i} \frac{(e^{ik|\mathbf{x}_i - \mathbf{y}|} - 1)}{4\pi|\mathbf{x}_i - \mathbf{y}|} \, d\Gamma_{\mathbf{y}} \; + \; \int_{T_i} \frac{1}{4\pi|\mathbf{x}_i - \mathbf{y}|} \, d\Gamma_{\mathbf{y}}. \tag{2.27}$$

Using the Taylor expansion

$$e^{ik|\mathbf{x}_i - \mathbf{y}|} \; = \; 1 \; + \; ik|\mathbf{x}_i - \mathbf{y}| \; + \; O(|\mathbf{x}_i - \mathbf{y}|^2) \tag{2.28}$$

and substituting equation (2.28) into the first term on the right side of equation (2.27) gives

$$\begin{aligned} \frac{e^{ik|\mathbf{x}_i - \mathbf{y}|} - 1}{4\pi|\mathbf{x}_i - \mathbf{y}|} &= \frac{1 \; + \; ik|\mathbf{x}_i - \mathbf{y}| \; + \; O(|\mathbf{x}_i - \mathbf{y}|^2) \; - \; 1}{4\pi|\mathbf{x}_i - \mathbf{y}|} \\ &= \frac{ik \; + \; O(|\mathbf{x}_i - \mathbf{y}|)}{4\pi}. \end{aligned} \tag{2.29}$$

Therefore the first term on the right hand side of equation (2.27) is non-singular and may be evaluated numerically using standard quadrature rules. The second term is weakly singular, but can be evaluated analytically using polar coordinates and trigonometry.

Let us consider integrals of the type arising in the second term of (2.27), where we integrate over a triangle T_i with centroid $\mathbf{x}_i$. The integral over T_i may be rewritten in polar coordinates by setting $r = |\mathbf{x}_i - \mathbf{y}|$ to be the radial distance from the integration point $\mathbf{y}$ to the collocation point $\mathbf{x}_i$, and setting θ to be the angular coordinate defined with respect to a fixed origin at $\mathbf{x}_i$. We obtain

$$\int_{T_i} \frac{1}{|\mathbf{x}_i - \mathbf{y}|} \, d\Gamma_{\mathbf{y}} = \int_0^{2\pi} \int_0^{R_\theta} \frac{1}{r} \, r \, dr \, d\theta = \int_0^{2\pi} \int_0^{R_\theta} 1 dr \, d\theta = \int_0^{2\pi} R_\theta d\theta, \tag{2.30}$$

where R_θ corresponds to the radial distance from $\mathbf{x}_i$ to the edge of the triangle T_i for each angle $0 \leqslant \theta < 2\pi$. We now split the integral with respect to θ into three sub-integrals by subdividing T_i into three smaller triangles formed by connecting

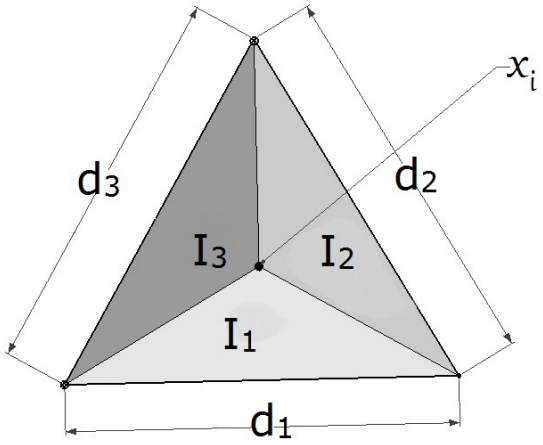

Figure 2.1: Splitting the triangle T_i at the centroid for analytic integration.

the centroid to each vertex as shown in Fig. 2.1. We label these three smaller triangles I_1, I_2 and I_3 and label the edge they share with T_i as d_1, d_2 and d_3, respectively.

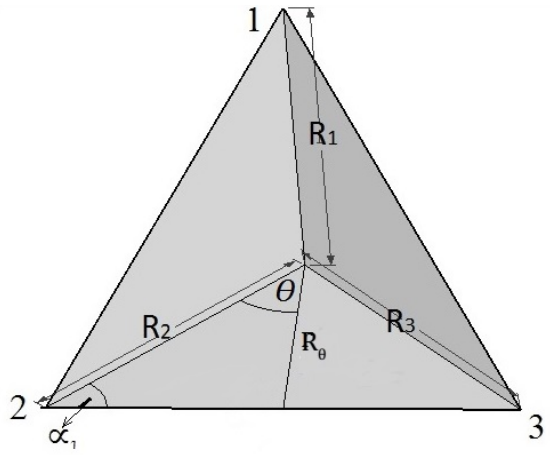

Figure 2.2: Quantities involved in the trigonometric interpretation of the radial distance R_θ.

Referring to Fig. 2.2 and using the sine rule of trigonometry, within sub-triangle I_1 we have that

$$R_\theta = \frac{R_2 \sin(\alpha_1)}{\sin(\pi - \theta - \alpha_1)}.$$

Hence the integral (2.30) restricted to sub-triangle I_1 can be expressed as

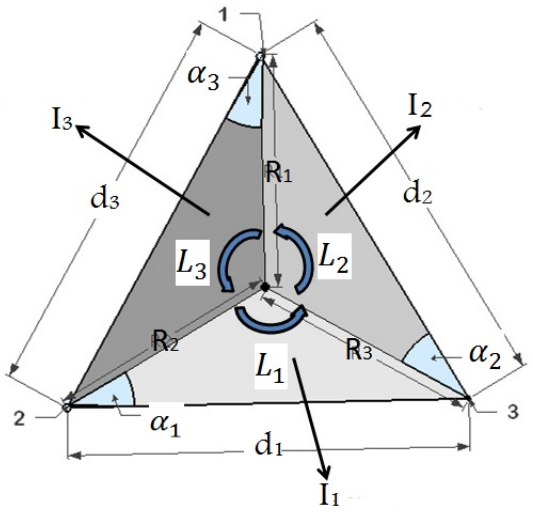

Figure 2.3: Quantities involves in the analytic integration formula for the integrals over I_1, I_2 and I_3 .

$$\int_0^{L_1} R_\theta d\theta = \int_0^{L_1} \frac{R_2 \sin\alpha_1}{\sin(\pi - \theta - \alpha_1)}\ d\theta,$$

where L_1 denotes the range of θ values within I_1 as shown in Fig. 2.3. Finally one integrates the above expression leading to the following formula for the sub-integral over I_1:

$$\begin{aligned}\int_{I_1} \frac{1}{|\mathbf{x}_i - \mathbf{y}|}\, d\Gamma_y \ &= R_2 \sin(\alpha_1)\Big[\log(\mathrm{cosec}(\alpha_1 + L_1) - \cot(\alpha_1 + L_1)) \\ &\quad - \log\left(\frac{(1 - \cot(\alpha_1)\sin(\alpha_1))}{\sin(\alpha_1)}\right)\Big].\end{aligned} \tag{2.31}$$

The integrals over I_2 and I_3 can be done by following the same procedure again. Adding the three integrals together leads to the analytic calculation of the second integral on the right hand side of (2.27).

2.4 Numerical results

In order to generate test problems for an arbitrary geometry, we shall use point sources to generate both the boundary data and the exact solution. Numerical results for the acoustic radiation from two geometrically different problems are considered. First, a unit sphere discretized by flat triangular elements, and second a cuboid of similar dimensions to a typical loudspeaker cabinet $(0.28 \times 0.28 \times 0.42)m^3$. In the case of the unit sphere the interior eigenfrequencies are known *a priori*. These are of interest since one well-known shortcoming of the boundary integral formulation introduced in Section 2.2 is that its solution is not uniquely defined at interior eigenfrequencies. The boundary data will be generated by a single unit point source at $\mathbf{y} = (0, 0, 0.1) \in \Omega_-$, where Ω_- is centred at the origin. All numerically estimated integrals are approximated using product 3×3 point Gaussian quadrature.

Table 2.1: The relative errors for different k values with different numbers of elements on the cuboid.

n	Err $(k = 1)$	Err $(k = 10)$	Err $(k = 17.52)$	Err $(k = 25)$
256	0.005887	0.015854	0.621088	0.058899
576	0.003528	0.008761	0.770646	0.028206
1024	0.002570	0.005796	0.493295	0.017181
1600	0.002078	0.004254	0.260537	0.011819

Table 2.1 shows the values of the ℓ^2 relative errors in the solution on the cuboid for different values of the wavenumber and different numbers of the elements. The

error is computed using the formula

$$\text{Err} = \frac{\sqrt{\sum_{i=1}^{n}(\phi_i - \phi(\mathbf{x}_i))^2}}{\sqrt{\sum_{i=1}^{n}\phi(\mathbf{x}_i)^2}}. \tag{2.32}$$

It was found numerically that $k = 17.52$ corresponds to an interior eigenfrequency of the cuboid and one notices a considerable increase in the error for this value of k. The errors are also approximately halving as n is doubled, which is the expected $O(n^{-1})$ convergence rate for piecewise constant collocation [53]. This is shown in Figure 2.4 for $k = 1, 10$ and 25. We also notice that, in general, the error is larger for larger k values.

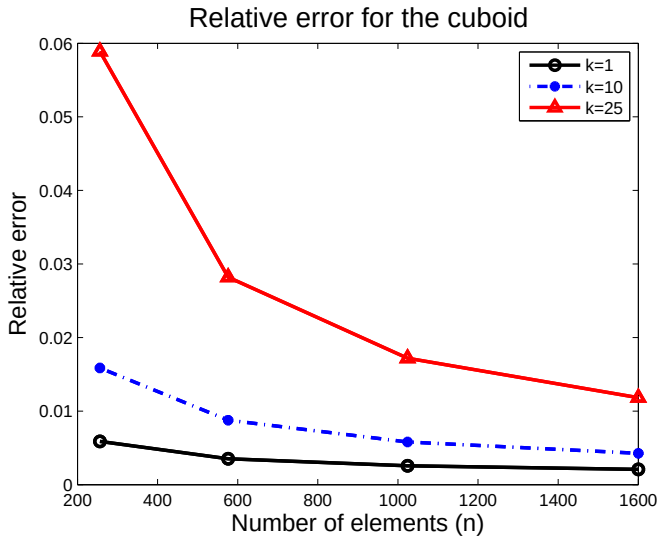

Figure 2.4: Relative error for the cuboid

Table 2.2 shows the relative errors in solutions on the sphere for different values of the wavenumber and different numbers of elements. It is known that $k = \pi$ corresponds to an internal resonance of the unit sphere. However, since here we are using a triangulated representation of the sphere, the problematic wavenumber

Table 2.2: The relative errors for different k values with different number of elements on the sphere.

n	Err $(k = 1)$	Err $(k = 3.19)$	Err $(k = 5)$
80	0.026678	0.120742	0.036765
320	0.006372	27.511925	0.009127
1280	0.001486	0.047489	0.002497
5120	3.32E-04	0.011564	7.51E-04

corresponds to $k = 3.19$ when $n = 320$ triangular elements are used and larger errors are observed in this case. However, $k = 3.19$ does not correspond to an internal resonance for other choices of n and so the results improve for these cases. That is, because the unit sphere has been represented using linear flat triangles, the surface geometry changes each time n changes, which therefore causes the internal resonance positions to change a small amount.

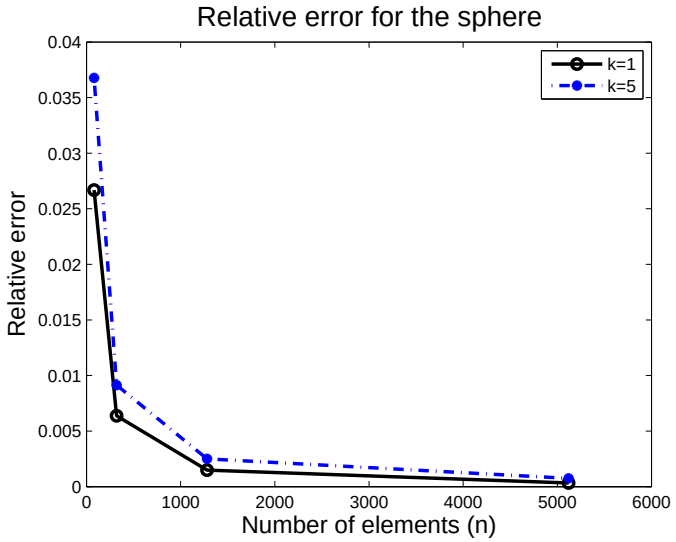

Figure 2.5: Relative error for the sphere

Figure 2.5 illustrates the relative errors in solutions on the sphere for $k = 1$ and $k = 5$ with different numbers of elements. Here we can see the same behaviour as for the cuboid. In general the error is larger for larger k values. We also observe the expected $O(n^{-1})$ convergence rate since the errors are again approximately halving as n is doubled.

2.5 Summary

In this chapter, the surface Helmholtz equation (2.17) for the exterior acoustic problem of the Helmholtz equation has been derived. The discretisation using the collocation method has been detailed for the solution of the surface Helmholtz equation with a given Neumann boundary condition. Moreover, methods for evaluating the arising weakly singular integral have been discussed. Finally, we considered numerical examples on a cuboid and a sphere and obtained accurate results in both cases.

Chapter 3

Fourier acoustics and near-field acoustic holography

3.1 Introduction

In this chapter we will discuss some of the introductory concepts of Fourier acoustics and scrutinise how this theory can be used in formulating models for near-field acoustic holography, that is, the inverse problem of reconstructing structural behaviour from measurements of the surrounding sound field. Here, we refer to Fourier acoustics as the application of Fourier transform based methods to solve the governing boundary integral equations. Fourier acoustics based NAH uses an acoustic double layer potential to describe the sound radiation from a two-dimensional planar region. In view of the fact that the double layer potential is effectively the convolution of the normal derivative of the half-space Green's function with the acoustic pressure in a two-dimensional planar region, the structural data may be obtained by using Fourier transforms and the convolution theorem.

3.2 Integral equations and Green's functions

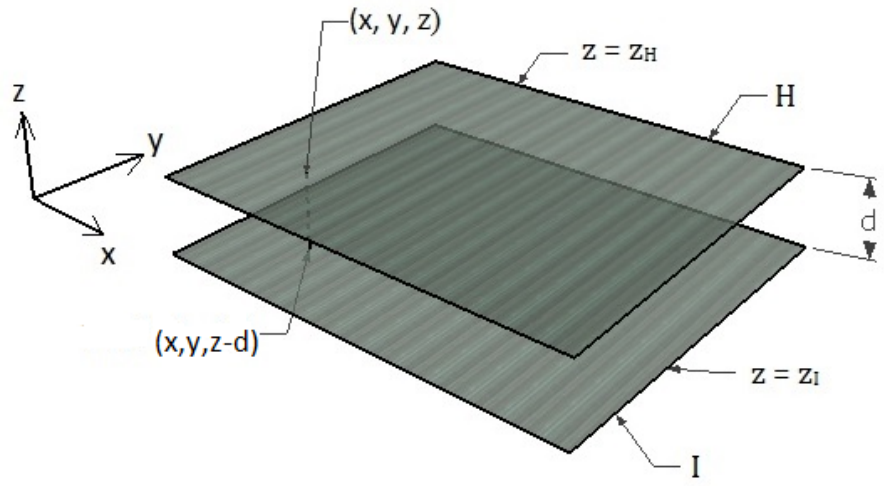

Figure 3.1: A vibrating plate at $z = z_I$ and a parallel hologram plane at $z = z_H$ where the pressure data is sampled in NAH.

Our aim is to reconstruct the surface velocity field on a radiating flat plate from known values of the pressure in a parallel plane at a small distance from the plate. Let the plane $z = z_I$ be the (infinite) surface of the vibrating plate, and the plane $z = z_H$ be the measurement (or hologram) plane, as shown in Figure 3.1. Let us now assume that $\mathbf{x}' = (x', y', z_I)$ is a point on the vibrating plate and $\mathbf{x} = (x, y, z) \in \mathbb{R}^3$ with $z > z_I$.

We consider the sound pressure ϕ at the point $\mathbf{x}$, which is given by the Helmholtz integral equation as follows

$$\phi(\mathbf{x}) = \int_{-\infty}^{\infty}\int_{-\infty}^{\infty} \left(\phi(\mathbf{x}') \, \frac{\partial \tilde{G}_k}{\partial \hat{\mathbf{n}}'}(\mathbf{x}, \mathbf{x}') \; - \frac{\partial \phi}{\partial \hat{\mathbf{n}}'}(\mathbf{x}') \, \tilde{G}_k(\mathbf{x}, \mathbf{x}') \right) dx' dy'. \tag{3.1}$$

Here $\hat{\mathbf{n}}' = (0, 0, 1)$ denotes the unit normal vector to the infinite plate, pointing into the half-space above. Note that (3.1) is simply equation (2.16) for $\mathbf{x} \in \Omega_+$ with $\Gamma = \mathbb{R}^2$ and the free-space Green's function G_k replaced with a half-space Green's function $\tilde{G}_k$. We now discuss how to obtain the half-space Green's function $\tilde{G}_k$ for the plate radiation problem in the half-space $z \geq z_I$ using the so-called method of images. The starting point is to again consider the free-space Green's function for the Helmholtz equation in three dimensions, which is given by

$$G_k(\mathbf{x}, \mathbf{x}') = \frac{e^{ik|\mathbf{x}-\mathbf{x}'|}}{4\pi|\mathbf{x} - \mathbf{x}'|}, \tag{3.2}$$

where $|\mathbf{x}-\mathbf{x}'| = \sqrt{(x - x')^2 + (y - y')^2 + (z - z_I)^2}$. We shall construct the Green's function $\tilde{G}_k$ to represent the physics of our half-space problem and, as a result, simplify the integral equation (3.1). Using the method of images, we consider the Green's function G_k evaluated at the reflection of the point $\mathbf{x}$ in the plane $z = z_I$. This reflection point is located at $\hat{\mathbf{x}} = (x, y, 2z_I - z)$ and hence we obtain

$$G_k(\hat{\mathbf{x}}, \mathbf{x}') = \frac{e^{ik\sqrt{(x-x')^2+(y-y')^2+(z_I-z)^2}}}{4\pi\sqrt{(x - x')^2 + (y - y')^2 + (z_I - z)^2}} = G_k(\mathbf{x}, \mathbf{x}'). \tag{3.3}$$

Subtracting the reflected Green's function from original Green's function yields our modified Green's function

$$\tilde{G}_k(\mathbf{x}, \mathbf{x}') := G_k(\mathbf{x}, \mathbf{x}') - G_k(\hat{\mathbf{x}}, \mathbf{x}'), \tag{3.4}$$

which is therefore zero.

In order to evaluate the integral equation (3.1), then we also need to find $\partial\tilde{G}_k/\partial\hat{\mathbf{n}}' = \partial\tilde{G}_k/\partial z_I$. Using the definition (3.4) leads to

$$\begin{aligned}\frac{\partial\tilde{G}_k}{\partial z_I} &= \frac{\partial G_k}{\partial z_I}(\mathbf{x}, \mathbf{x}') - \frac{\partial G_k}{\partial z_I}(\hat{\mathbf{x}}, \mathbf{x}') \\ &= \frac{\partial G_k}{\partial z_I}(\mathbf{x}, \mathbf{x}') + \frac{\partial G_k}{\partial z_I}(\mathbf{x}, \mathbf{x}'),\end{aligned}$$

since from (3.3)

$$G_k(\hat{\mathbf{x}}, \mathbf{x}') = f(x - x', y - y', z_I - z), \tag{3.5}$$

where

$$f(x, y, z) = \frac{e^{ik\sqrt{(x)^2+(y)^2+(z)^2}}}{4\pi\sqrt{(x)^2 + (y)^2 + (z)^2}} \ , \tag{3.6}$$

whereas

$$G_k(\mathbf{x}, \mathbf{x}') = f(x - x', y - y', z - z_I). \tag{3.7}$$

Note the change of sign in the third argument.

As a result we end up with the expression

$$\frac{\partial \tilde{G}_k}{\partial z_I} = \frac{1}{2\pi}\frac{\partial}{\partial z_I}\left[\frac{e^{ik\sqrt{(x-x')^2+(y-y')^2+(z-z_I)^2}}}{\sqrt{(x - x')^2 + (y - y')^2 + (z - z_I)^2}}\right]. \tag{3.8}$$

Equation (3.1) can now be rewritten using that $\tilde{G}_k = 0$ to give

$$\phi(\mathbf{x}) = \int_{-\infty}^{\infty}\int_{-\infty}^{\infty} \frac{\partial \tilde{G}_k}{\partial \hat{\mathbf{n}}'}(\mathbf{x}, \mathbf{x}')\phi_I(\mathbf{x}')dx'dy', \tag{3.9}$$

and hence from (3.8) we obtain

$$\phi(\mathbf{x}) = \frac{-1}{2\pi}\int_{-\infty}^{\infty}\int_{-\infty}^{\infty} \frac{\partial}{\partial \zeta}\left[\frac{e^{ik\sqrt{(x-x')^2+(y-y')^2+\zeta^2}}}{\sqrt{(x - x')^2 + (y - y')^2 + \zeta^2}}\right]\Bigg|_{\zeta=z-z_I} \phi_I(x', y', z_I)dx'dy'. \tag{3.10}$$

Note that in equation (3.9) and (3.10) we have introduced the notation ϕ_I to specify the acoustic pressure ϕ in the plane $z = z_I$.

3.3 Fourier methods

In this section we describe the application of Fourier transforms and the convolution theorem to solve the integral equation (3.9) for the acoustic pressure ϕ_I in the plane $z = z_I$. A review of some background theory on Fourier transforms is given in Appendix A.

3.3.1 Solution as a convolution equation

We note that equation (3.9) is a two-dimensional convolution integral and may be written in the form

$$\phi = \frac{\partial \tilde{G}_k}{\partial \hat{\mathbf{n}}'} * \phi_I. \tag{3.11}$$

Hence we may evaluate ϕ_I by taking Fourier transforms to give

$$\mathcal{F}\phi = \mathcal{F}\left(\frac{\partial \tilde{G}_k}{\partial \hat{\mathbf{n}}'} * \phi_I\right) = \left(\mathcal{F}\frac{\partial \tilde{G}_k}{\partial \hat{\mathbf{n}}'}\right)(\mathcal{F}\phi_I) \tag{3.12}$$

using the convolution theorem (see Appendix A). Therefore the sound pressure ϕ_I at the surface of the plate is given by

$$\phi_I = \mathcal{F}^{-1}\left[(\mathcal{F}\phi) \,/\, \left(\mathcal{F}\frac{\partial \tilde{G}_k}{\partial \hat{\mathbf{n}}'}\right)\right]. \tag{3.13}$$

Unfortunately, the numerical evaluation of $\mathcal{F}\left(\frac{\partial \tilde{G}_k}{\partial \hat{\mathbf{n}}'}\right)$ using a discrete Fourier transform causes numerical instabilities. Since $\mathcal{F}\left(\frac{\partial \tilde{G}_k}{\partial \hat{\mathbf{n}}'}\right)$ frequently takes values containing small errors and that are approximately zero, division by $\mathcal{F}\left(\frac{\partial \tilde{G}_k}{\partial \hat{\mathbf{n}}'}\right)$ comes instabilities. In Section 3.3.3 we describe how this Fourier transform may be computed exactly using an integral identity known as the Weyl integral.

3.3.2 Neumann boundary data for plane wave radiation

If instead of computing the sound pressure ϕ_I, we wish to reconstruct the Neumann boundary data $\frac{\partial \phi_I}{\partial \hat{\mathbf{n}}'}$ on the flat plate, then we can proceed as follows in the case of plane wave radiation from an infinite flat plate. Let us assume that the radiated wave vector at the point $\mathbf{x}$ has wave vector $\mathbf{k} = (k_x, k_y, k_z)$, which has length $k = |\mathbf{k}|$. Since a radiated plane wave of amplitude A may be written in the form $Ae^{i\mathbf{k}\cdot\mathbf{x}}$, then in the plate at $z' = z_I$ it follows that

$$\frac{\partial \phi_I}{\partial \hat{\mathbf{n}}'} = \frac{\partial \phi_I}{\partial z'} = ik_z\, \phi_I. \tag{3.14}$$

Let k_B be the wavenumber for the flexural vibration of the plate. Then by continuity of the wave vector at the interface between the plate and the acoustic medium above, we have that the wave vector in the plate must be (k_x, k_y) and hence $k_B = \sqrt{k_x^2 + k_y^2}$. On the plate at $z = z_I$, we therefore have that $k_B^2 + k_z^2 = k^2$. Combining this with equation (3.14) leads to

$$\phi_I = \frac{1}{i\sqrt{k^2 - k_B^2}} \frac{\partial \phi_I}{\partial \hat{\mathbf{n}}'}. \tag{3.15}$$

Now substitute equation (3.15) into equation (3.9) and re-arrange to give

$$\phi(\mathbf{x}) = \int_{-\infty}^{\infty}\int_{-\infty}^{\infty} \left[\frac{1}{i\sqrt{k^2 - k_B^2}} \frac{\partial \tilde{G}_k}{\partial \hat{\mathbf{n}}'}(\mathbf{x}, \mathbf{x}') \right] \frac{\partial \phi_I}{\partial \hat{\mathbf{n}}'}(\mathbf{x}')dx'dy'. \tag{3.16}$$

We may evaluate $\frac{\partial \phi_I}{\partial \hat{\mathbf{n}}'}$ by Fourier transforming equation (3.16) and following the procedure outlined in equations (3.11) to (3.13). Letting

$$F_k(\mathbf{x}, \mathbf{x}') = \frac{1}{i\sqrt{k^2 - k_B^2}} \frac{\partial \tilde{G}_k}{\partial \hat{\mathbf{n}}'}(\mathbf{x}, \mathbf{x}'), \tag{3.17}$$

then the result is that

$$\frac{\partial \phi_I}{\partial \hat{\mathbf{n}}'} = \mathcal{F}^{-1}\left[(\mathcal{F}\phi) \,/\, (\mathcal{F}F_k) \right]. \tag{3.18}$$

3.3.3 Application of the Weyl integral

In this section we derive the expression

$$\frac{\partial \tilde{G}_k}{\partial \hat{\mathbf{n}}'}(\mathbf{x}, \mathbf{x}') = \mathcal{F}^{-1}\left[e^{i\zeta\sqrt{k^2 - (k_x^2 + k_y^2)}} \right] \tag{3.19}$$

for the Fourier transform of $\partial \tilde{G}_k / \partial \hat{\mathbf{n}}'$, using a classical result known as the Weyl integral. Here k_x, k_y and k_z are the Fourier k-space coordinates, as before, so that $k_z = \sqrt{k^2 - k_x^2 - k_y^2}$ and $\zeta = z - z_I > 0$. The use of the Weyl integral [54] to derive the identity (3.19) is described in Ref. [55], and the argument given there is expanded below. Weyl's integral provides an expansion of the free space Green's

function in terms of plane waves as follows:

$$\frac{e^{ik|\mathbf{x}-\mathbf{x}'|}}{|\mathbf{x}-\mathbf{x}'|} = \frac{i}{2\pi}\int_{-\infty}^{\infty}\int_{-\infty}^{\infty} \frac{e^{i\zeta\sqrt{k^2-(k_x^2+k_y^2)}}\, e^{ik_x(x-x')}\, e^{ik_y(y-y')}}{\sqrt{k^2-(k_x^2+k_y^2)}} dk_x dk_y. \tag{3.20}$$

First, we differentiate both sides of Eq. (3.20) with respect to $z_I = z - \zeta$ and restrict to $z > z_I$ to give

$$\frac{\partial}{\partial z_I}\left(\frac{e^{ik|\mathbf{x}-\mathbf{x}'|}}{|\mathbf{x}-\mathbf{x}'|}\right) = \frac{1}{2\pi}\int_{-\infty}^{\infty}\int_{-\infty}^{\infty} e^{ik_x(x-x')}\, e^{ik_y(y-y')} e^{i\zeta\sqrt{k^2-(k_x^2+k_y^2)}}\, dk_x dk_y. \tag{3.21}$$

Multiplying both sides by $\frac{1}{2\pi}$ leads to $\partial\tilde{G}_k/\partial\hat{\mathbf{n}}'$ on the left hand side (see equation (3.8) and thus

$$\frac{\partial\tilde{G}_k}{\partial\hat{\mathbf{n}}'}(\mathbf{x},\mathbf{x}') = \frac{1}{4\pi^2}\int_{-\infty}^{\infty}\int_{-\infty}^{\infty} e^{ik_x(x-x')}\, e^{ik_y(y-y')} e^{i\zeta\sqrt{k^2-(k_x^2+k_y^2)}}\, dk_x dk_y. \tag{3.22}$$

Using the definition of the inverse Fourier transform in two-dimensions (see Appendix A) we find

$$\mathcal{F}^{-1}\left[e^{i\zeta\sqrt{k^2-(k_x^2+k_y^2)}}\right] = \frac{1}{4\pi^2}\int_{-\infty}^{\infty}\int_{-\infty}^{\infty} e^{i\zeta\sqrt{k^2-(k_x^2+k_y^2)}}\, e^{ik_x(x-x')}\, e^{ik_y(y-y')}\, dk_x dk_y. \tag{3.23}$$

Now, combining equations (3.22) and (3.23) completes the derivation of the result (3.19). We may use the results given above to solve the NAH problem on an infinite periodic plate as described in the next section.

3.4 Numerical results

We consider the example of modelling plane wave acoustic radiation from an infinite vibrating plate, as discussed in Sect. 3.3.2. As in the previous chapter, we denote the density of the acoustic medium as ρ and use c to denote the speed of sound. We now derive an expression for the acoustic wave radiated by a flexural plane wave propagating within an infinite flat plate lying in the plane $z = z_I$.

Only a sketch is given here; full details are included in Appendix B and can also be found in many texts on structural acoustics, such as [56, 57]. We will then use the derived expressions for the plate velocity and the radiated acoustic pressure to test our Fourier acoustics formulation for the inverse problem of NAH for the same example.

Assuming that the wavenumber of the flexural wave is k_B, that it has amplitude u_0 and that it is directed parallel to the y-axis leads to an expression for the displacement of the plate in the z-direction (i.e. the normal displacement) of the form $u = u_0 e^{ik_B y}$. Since time-harmonic waves of angular frequency ω have a time-dependent factor of the form $e^{-i\omega t}$, then we may write the normal velocity as

$$v = -i\omega u_0 e^{ik_B y} = v_0 e^{ik_B y}. \tag{3.24}$$

Applying continuity of the wave vector at the surface of the plate $z = z_I$, then the radiated acoustic pressure wave can be expressed in the form

$$\phi = \phi_0 e^{ik_B y} e^{ik_z z}, \tag{3.25}$$

where $k^2 = k_B^2 + k_z^2$. The frequency domain form of the linearised Euler's equation

$$\frac{\partial \phi}{\partial \hat{\mathbf{n}}'} = i\omega\rho v \tag{3.26}$$

can then be applied to find a relation between the amplitude coefficients v_0 and ϕ_0. The result is that the radiated pressure must satisfy

$$\phi(\mathbf{x}) = \frac{\omega\rho v_0}{\sqrt{k^2 - k_B^2}} e^{ik_B y} e^{i\sqrt{k^2 - k_B^2}(z - z_I)}. \tag{3.27}$$

Note that the solution is independent of x due the assumed form of the flexural wave in the plate. See Appendix B for further details. The expression (3.27) only describes a propagating acoustic wave for $k > k_B$, since for $k < k_B$ the final exponential term becomes exponentially decaying. This means that ϕ will decay

exponentially in the z-direction. Waves of this type are known as evanescent. At $k = k_B$ the coefficient at the front of the expression (3.27) is undefined, and so for simplicity we will restrict our NAH study in this chapter to the propagating acoustic radiation case $k > k_B$.

We now give numerical results for the NAH problem where the pressure data ϕ is provided by the formula (3.27) with parameters $v_0 = 1$, $\rho = 1.21\text{kg/m}^3$, and $c = 340\text{m/s}$, which are commonly used parameters for air. Figure 3.2 shows the results of using the Fourier acoustics solution (3.18) (right column) in comparison to the exact solution (left column) for the Neumann data on the plate $z = z_I = 0$. Note that this exact solution may be obtained by combining the formulae (3.24) and (3.26). The three rows of the plot show the effect of varying the height of the hologram plane $z = z_H$ (see Fig. 3.1), where the pressure data (3.27) is sampled over a uniform grid $(x, y) \in [-1, 1] \times [-1, 1]$ with 64×64 sample points. In each case we have taken the wavenumbers to be $k = 10$ and $k_B = 2\pi$. The latter choice is important since it means that our sampled domain in the $x - y$ plane from $y = -1$ to $y = 1$ provides a periodic segment of the infinite plane. Hence the solution over this region corresponds to the infinite plane after making repeated copies of the sampled region and placing them side by side. This combination of flexural and acoustic wavenumbers means that $k_z = \sqrt{k^2 - k_B^2} = 2\sqrt{25 - \pi^2} = 7.7796$ and so the wavelength of the propagated acoustic wave in the z-direction is $\lambda_z = 2\pi/k_z = 0.8077$. We investigate choices of the hologram plane $z = z_H$ within the acoustic near-field $0 < z_H < 0.8077$.

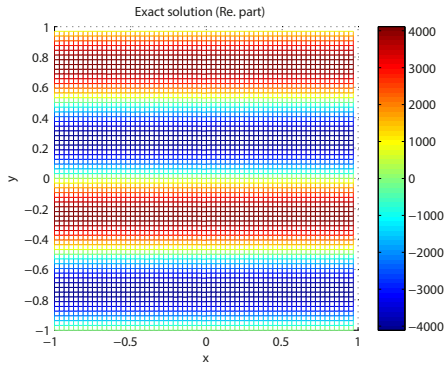

(a) $Z_H = 0.05$

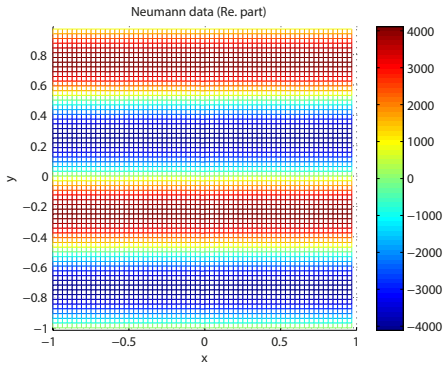

(b) $Z_H = 0.05$

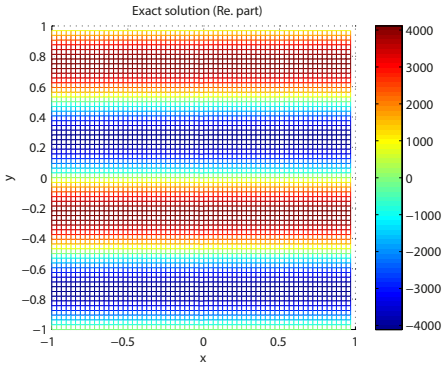

(c) $Z_H = 0.35$

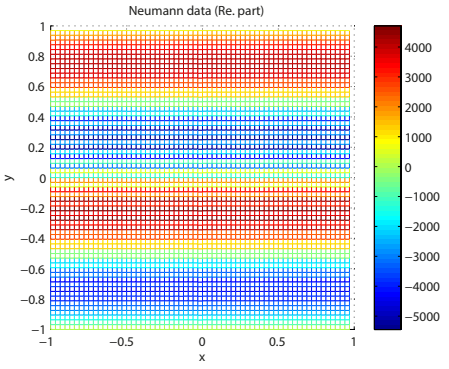

(d) $Z_H = 0.35$

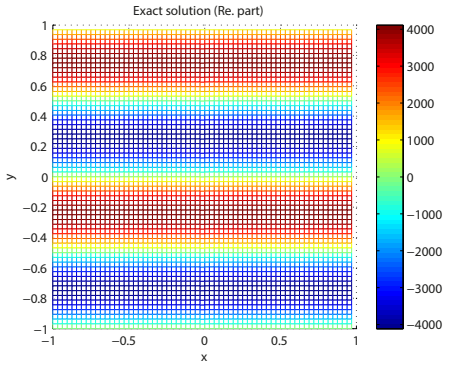

(e) $Z_H = 0.4$

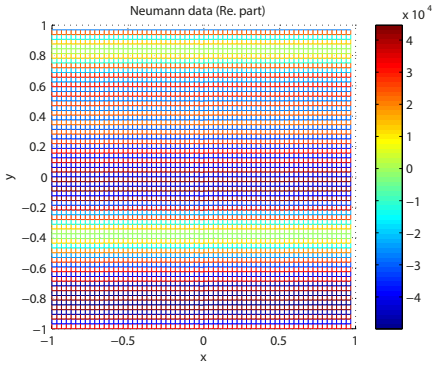

(f) $Z_H = 0.4$

Figure 3.2: Exact and Fourier based NAH results for the Neumann data on an infinite vibrating plate at $z = z_I = 0$. Here we model plane wave radiation with acoustic wavenumber $k = 10$ and flexural wavenumber $k_B = 2\pi$ directed along the y-axis. The results are shown for different positions of the measurement (or hologram) plane at $z = z_H$.

The results in the first row of Figure 3.2 (i.e. plots (a) and (b)), show the case where $z_H = 0.05$ and so the hologram plane is relatively close to the vibrating plate at $z = 0$. In this case, the Fourier acoustics NAH reconstruction matches the exact solution very well. This would be expected since the measurements are taken sufficiently far inside the acoustic near-field. Plots (c) and (d) in the second row of Figure 3.2 show the case when $z_H = 0.35$. The measurements points are now sufficiently far away from the plate to introduce errors into the Fourier NAH reconstructed solution, and one can notice small but visible differences between the plots (c) and (d). In the third row of Figure 3.2 we consider the case when $z_H = 0.4$. Now the distance between the plate and the measurement plane is large enough to have a catastrophic effect on the reconstructed results, and the reconstruction bears no resemblance to the exact solution. Note that since NAH is an ill-posed inverse problem, the reconstruction could potentially be improved by applying a regularisation procedure such as Tikhonov regularisation. This will be discussed further in the next chapter for NAH problems with noisy pressure data. Here we note that in general, even after a regularisation method has been applied, we will still obtain poor results when z_H is taken to be sufficiently large due to the loss of evanescent (exponentially decaying) wave contributions in the pressure data. We also note that the loss of evanescent wave contributions occurs when sampling the acoustic pressure data far from the vibrating plate. In the near-field these waves can still be detected and are therefore included in NAH.

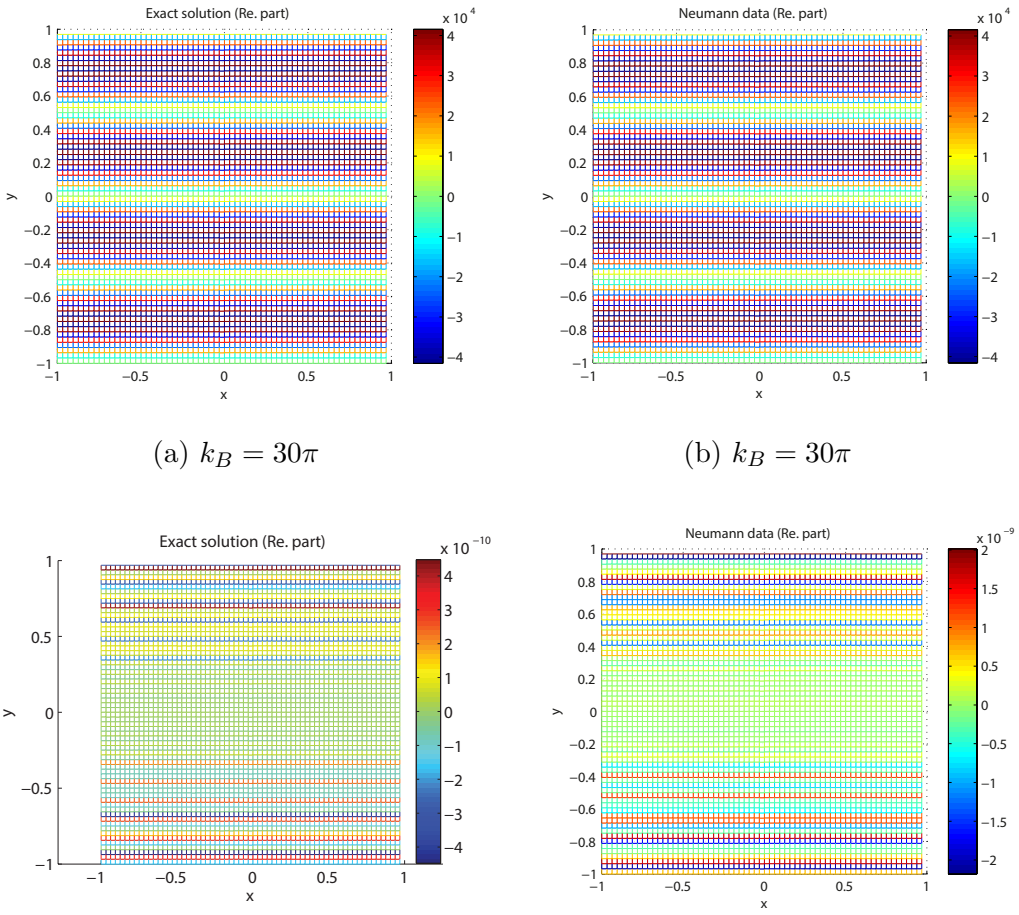

(a) $k_B = 30\pi$ (b) $k_B = 30\pi$

(c) $k_B = 32\pi$ (d) $k_B = 32\pi$

Figure 3.3: Exact and Fourier based NAH results for the Neumann data on an infinite vibrating plate at $z = z_I = 0$. Here we model acoustic radiation at wavenumber $k = 101$ due to a flexural plane wave directed along the y-axis. The measurement data for the acoustic pressure is sampled on a regular grid in the plane $z = z_H = 0.05$. The results are shown for different flexural wavenumbers k_B close to the Nyquist sampling limit.

Figure 3.3 again shows the results of using the Fourier acoustics solution (3.18) (right column) in comparison to the exact solution (left column) for the Neumann data on the plate $z = z_I = 0$. However, now the two rows of the plot show the

effect of increasing the flexural wavenumber k_B to values in the vicinity of the Nyquist limit with a fixed hologram plane at $z = z_H = 0.05$. The pressure data is sampled over a uniform grid $(x, y) \in [-1, 1] \times [-1, 1]$ with 64×64 sample points, as before, meaning that the Nyquist limit for the wavenumber k_B in the y-direction is given by $k_B^{\text{Nyq}} = 64\pi/2 = 32\pi$. Note that a brief introduction to sampling theory and the Nyquist limit can be found in Appendix C. In each case we have taken the acoustic wavenumber to be $k = 101 > 32\pi$ and k_B to be a multiple of 2π. This ensures periodicity of the reconstructed solution, as before.

The results in the first row of Figure 3.3 show the case where $k_B = 30\pi$. Plot (b) in the right column shows the Fourier NAH reconstruction of the Neumann data, which matches very well with the exact solution shown in plot (a). In the second row we see that when the wavenumber is increased to correspond to the Nyquist sampling rate at $k_B = 32\pi$, then the accuracy of the reconstruction is completely lost. The exact solution shown in plot (c) differs from the reconstruction shown in plot (d) by an order of magnitude. We therefore conclude that our implementation of Fourier acoustics based NAH only gives reliable results below the Nyquist sampling rate.

3.5 Summary

In this chapter, we introduced Fourier acoustics methods for solving the inverse problem of NAH on a flat plate, whereby the vibrational behaviour of the plate is reconstructed from acoustic pressure data in the near- field. We first described an integral equation formulation for modelling acoustic radiation from an infinite flat plate using a modified Green's function given by the method of images. We then applied Fourier transforms and the convolution theorem to solve this integral equation for either the pressure or the Neumann data on the flat plate, given acoustic

pressure data in near field above the plate. Finally, we described some numerical experiments for reconstructing flexural plane wave vibrations in the plate, given the associated pressure data in the near-field. We compared our reconstructions with an exact solution to investigate the effect of changing both the location of the given pressure data, and the wavenumber, on the quality of the reconstructed solutions.

Chapter 4

Inverse boundary element method for near-field acoustic holography

4.1 Introduction

In Chapter 2, the application of the BEM to the forward Neumann problem was described. For this problem we computed the acoustic pressure ϕ on Γ and in Ω_+, given $\partial\phi/\partial\hat{\mathbf{n}}$ on Γ. If we instead find the acoustic sources on an emitting object, given the measured sound field surrounding the radiating object, then this is an example of an inverse problem. The reason for our study of BEM for the forward Neumann problem is that the corresponding inverse problem, to determine $\partial\phi/\partial\hat{\mathbf{n}}$ on Γ given a set of values of ϕ in Ω_+, is precisely the NAH problem studied in the previous chapter. Applying the BEM to this inverse problem is known as the inverse boundary element method (IBEM).

4.2 Inverse boundary element method

The first step towards reformulating the boundary integral equations introduced in the Chapter 2 for the inverse problem of NAH is to consider equation (2.16) for $\mathbf{x} \in \Omega_+$ thus

$$-\phi(\mathbf{x}) + \int_\Gamma \phi(\mathbf{y}) \frac{\partial G_k(\mathbf{x},\mathbf{y})}{\partial \hat{\mathbf{n}}_\mathbf{y}} \, d\Gamma_\mathbf{y} = \int_\Gamma G_k(\mathbf{x},\mathbf{y}) \frac{\partial \phi(\mathbf{y})}{\partial \hat{\mathbf{n}}_\mathbf{y}} \, d\Gamma_\mathbf{y}. \tag{4.1}$$

Let us now define the acoustic single and double layer integral operators at $\mathbf{x} \in \Omega_+$ as

$$\mathcal{S}\phi(\mathbf{x}) := \int_\Gamma G_k(\mathbf{x},\mathbf{y}) \phi(\mathbf{y}) d\Gamma_\mathbf{y}, \tag{4.2}$$

and

$$\mathcal{D}\phi(\mathbf{x}) := \int_\Gamma \frac{\partial G_k(\mathbf{x},\mathbf{y})}{\partial \hat{\mathbf{n}}_\mathbf{y}} \phi(\mathbf{y}) d\Gamma_\mathbf{y}, \tag{4.3}$$

respectively. Solve (4.1) for $\phi \in \Omega_+$:

$$\phi(\mathbf{x}) = \mathcal{D}\phi - \mathcal{S}\frac{\partial \phi}{\partial \hat{\mathbf{n}}} \tag{4.4}$$

In the case $\mathbf{x} \in \Gamma$ we make a distinction and instead label these operators as $\mathcal{V}$ and $\mathcal{K}$, respectively. Then, we can write the solution procedure for equations (4.1) and (2.17) together to give ϕ in Ω_+ in terms of these integral operators acting on $\partial\phi/\partial\hat{\mathbf{n}}$ as follows

$$\phi(\mathbf{x}) = \left(\mathcal{D} \left[\left(-\frac{1}{2} I + \mathcal{K} \right)^{-1} \mathcal{V} \right] - \mathcal{S} \right) \frac{\partial \phi}{\partial \hat{\mathbf{n}}}, \qquad \mathbf{x} \in \Omega_+. \tag{4.5}$$

The solution of the inverse problem of NAH is given by solving Eq. (4.5) for $\partial\phi/\partial\hat{\mathbf{n}}$, given a set of known values for ϕ in Ω_+. Unfortunately this inverse problem is ill-posed because the solution $\partial\phi/\partial\hat{\mathbf{n}}$ does not depend continuously on the data $\phi(\mathbf{p}_i)$, where $\mathbf{p}_i$, $i = 1, ..., m$, are a discrete set of points in Ω_+ where ϕ is known. Equation (4.5) may be written in the following discrete form

$$[\phi(\mathbf{p}_i)]_{i=1,\ldots,m} = \left(D \left[\left[-\frac{1}{2} I + K \right]^{-1} V \right] - S \right) \mathbf{v}, \tag{4.6}$$

where K and V are as given in (2.25), $\mathbf{v}$ is the vector of values of $\partial\phi/\partial\hat{\mathbf{n}}$ at the collocation points on Γ and

$$\begin{aligned} D_{ij} &= \int_{T_j} \frac{\partial G_k(\mathbf{p}_i, \mathbf{y})}{\partial \hat{\mathbf{n}}_{\mathbf{y}}} d\Gamma_{\mathbf{y}}, \\ S_{ij} &= \int_{T_j} G_k(\mathbf{p}_i, \mathbf{y}) d\Gamma_{\mathbf{y}}. \end{aligned} \tag{4.7}$$

Recall from Chapter 2 that we are using a piecewise collocation method on a boundary element mesh with (flat triangular) elements T_j, $j = 1, \ldots, n$, and the collocation points are taken at the centroids of these elements.

The solution of the discretised inverse problem (4.6) requires solving an ill-conditioned linear system, even in the case $m = n$. This is a result of the ill-posedness of the underlying continuous inverse problem (4.5) described earlier. In order to overcome this problem we use Tikhonov regularisation as described in the next section.

4.3 Regularisation techniques

In this section we describe the application of Tikhonov regularisation to the ill-conditioned linear system (4.6). We restrict to the case $m = n$ and apply regularisation to improve the stability of the reconstructed solution when noise is present in the acoustic pressure data. For NAH this data is provided by measurements, typically using a microphone array, and so some degree of noise will invariably be present. To simplify notation we write the $n \times n$ matrix given in round brackets on the right of equation (4.6) as A. Then our linear system is given by $A\mathbf{v} = \mathbf{b}$, with $\mathbf{b} = [\phi(\mathbf{p}_i)]^T_{i=1,\ldots,m}$. This is an ill-conditioned linear system meaning that the output is unstable to small changes in the input, and so any noise or infidelity in the pressure data vector $\mathbf{b}$ will badly corrupt the reconstructed Neumann bound-

ary data $\mathbf{v}$. In order to avoid this problem we replace the original linear system with the perturbed system

$$\left(A^T A + \lambda^2 L^T L\right) \mathbf{v} = A^T \mathbf{b}, \tag{4.8}$$

where $\lambda > 0$ is a small parameter to be determined called the regularisation parameter and L is the so-called Tikhonov matrix. In this work we apply a zero order regularisation scheme, which means that we set L to be the $n \times n$ identity matrix. More sophisticated choices of L are possible if we have additional information about the nature of the system to be solved. A zero order scheme is both simple and effective for the problem under consideration here assuming no *a priori* knowledge of the properties of the noise. For details of some higher order schemes that are suitable for NAH applications see Ref. [36].

The choice of the parameter λ is a more important issue to consider. If λ is too small, then we still have an ill-conditioned problem that is difficult to solve accurately. If λ is too large, this leads to change the original problem by a large amount, so the solution is not close to the solution of the original problem. In fact, several methods to predict the best λ exist, such as the L-curve method, Generated Cross Validation (GCV) and the Morozov discrepancy principle. Hansen [37] compared these methods and deduced that the L-curve method is more robust to different types of noise. However, Williams [36] reviewed these methods for NAH applications and reported that a modified GCV based scheme is favourable. In fact, the best choice of method is highly problem dependent. In this work, since the exact solution is known (see Sect. 4.4), an optimal choice of λ can be found by calculating the error in the approximate solution for a range of λ values and then choosing the value to minimise this error.

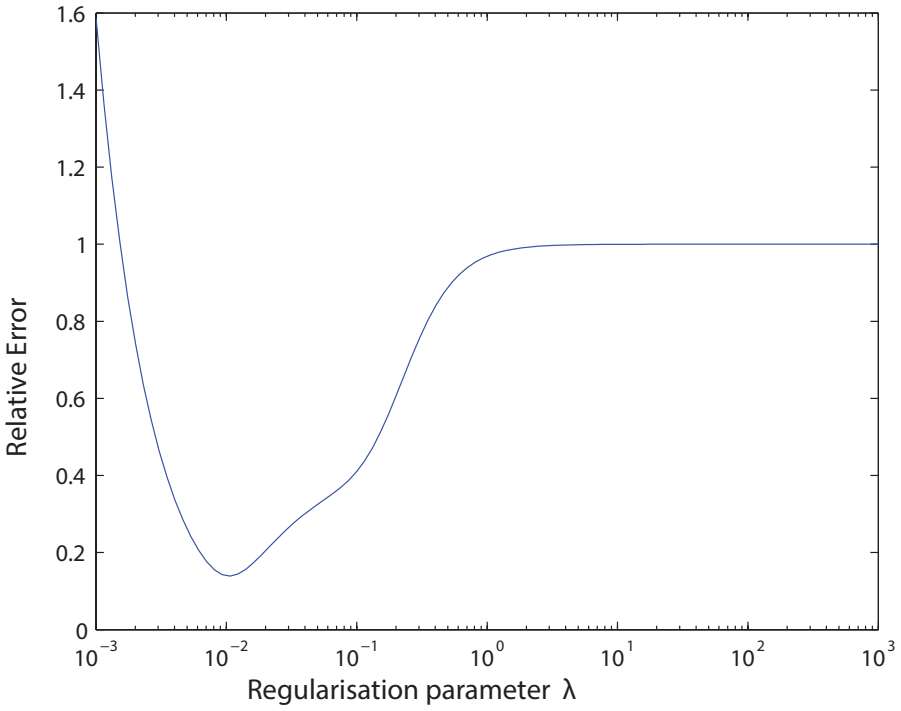

Figure 4.1: The relative error plotted against the regularisation parameter λ for 100 values of λ between 10^{-3} and 10^{3} on a logarithmic scale. For the plot given, we used $k = 1$ and added 5% uniformly distributed white noise to the pressure data vector.

Fig. 4.1 shows an example where the optimum value of λ is chosen to minimize the relative error over a range of regularisation parameters. Here, the minimum error in the reconstructed Neumann boundary data is 0.1388 and the corresponding value of λ is 0.0123. Fig. 4.1 shows how sensitive the error is to the choice of λ and that a poor choice can lead to large errors. In this plot the noise level in the vector of pressure data is set to be 5% of the signal and the wavenumber is taken to be $k = 1$.

4.4 Numerical examples

Two geometrically different test problems are considered here. First, a cuboid of similar dimensions to a typical loudspeaker with dimensions $(0.28 \times 0.28 \times 0.42)\text{m}^3$, discretized by 576 triangular elements and second, a unit sphere discretized by 320 flat triangular elements. In both cases we consider boundary data generated by three different point sources at $(0, 0, 0)$, $(0, 0, 0.1)$ and $(0, 0, -0.1)$, with wavenumber $k = 1$. Uniformly distributed and additive white noise will be applied to the pressure data vector $\mathbf{b}$ in order to more closely replicate experimental observations. The use of Gaussian noise was also considered and, in general, led to slightly more accurate reconstructions than uniformly distributed noise. However, the quality of reconstructions also fluctuated more widely when using different Gaussian noise vectors (of the same norm) than for uniformly distributed noise. Thus, we present the results for uniformly distributed noise since we believe they give a more indicative and repeatable measure of the performance of our reconstruction methods. We denote the added noise vector as $\mathbf{w}$ and specify the ratio

$$w = \frac{\|\mathbf{w}\|_2}{\|\mathbf{b}\|_2}, \tag{4.9}$$

referring to w as the level of added noise in the sequel. The notation $\| - \|_2$ refers to the Euclidean norm.

For the cuboid, the location of the points at which the pressure data are sampled is taken to be at a distance of 0.05m from the centroid of each element in the direction normal to the element surface. The horizontal distance between the centroid of each adjacent triangle is approximately 0.03m. For the sphere, a distance of 0.2m has been considered as the distance from the centroid of each element to the pressure data sampling position in the direction normal to the element surface.

The horizontal distance between the centroid of each adjacent triangle is approximately 0.2m in this case. The wavenumber corresponding to the Nyquist frequency here is $k_{\text{nyq}} = \pi/h$, where h is the distance between adjacent pressure data points, see Appendix C. For the cuboid geometry we have that $k_{\text{nyq}} = \pi/0.03 \approx 104.7\text{m}^{-1}$ and for the sphere, the Nyquist wavenumber $k_{\text{nyq}} = \pi/0.2 \approx 15.5\text{m}^{-1}$. Thus, we note that for both geometries the value of $k = 1$ used here is much smaller than the value of k_{nyq}, meaning that we should expect to be able to obtain good reconstructions from the generated pressure data. Note that we have chosen the data points to lie a similar distance from the object as the collocation points are spaced apart by. This is to avoid problems with near-singular behaviour of the Green's function for points close to the boundary. As discussed in Chapter 3, it is also beneficial to take the data points as close to the object as possible, to avoid the loss of evanescent wave contributions.

Assume that $\mathbf{x} = (x_1, x_2, x_3)$ is the location of a data point in Ω_+ and $\mathbf{x}_p = (0, 0, z)$ is a point source inside the object Ω_-, generating this data. Then the acoustic pressure ϕ at the point $\mathbf{x}$ is given by the free space Green's function as

$$\phi(\mathbf{x}) = \frac{e^{ik|\mathbf{x}-\mathbf{x}_p|}}{4\pi|\mathbf{x}-\mathbf{x}_p|}, \tag{4.10}$$

where

$$|\mathbf{x}-\mathbf{x}_p| = \sqrt{x_1^2 + x_2^2 + (x_3 - z)^2}.$$

We use data generated as described above, including additional noise, to reconstruct $\partial\phi/\partial\hat{\mathbf{n}}$ on Γ using equation (4.6). An exact expression for $\partial\phi/\partial\hat{\mathbf{n}}$ is also available in this case, which will be useful for comparison with our reconstructed solution. The exact solution is found by taking $\mathbf{x} \in \Gamma$ in equation (4.10) and then calculating $(\hat{\mathbf{n}} \cdot \nabla\phi)(\mathbf{x})$ to gives

$$\partial\phi/\partial\hat{\mathbf{n}} = \frac{1}{4\pi}\left(\frac{\mathbf{n}_y \cdot (\mathbf{x}-\mathbf{x}_p)}{|\mathbf{x}-\mathbf{x}_p|^3}(1 - ik|\mathbf{x}-\mathbf{x}_p|)e^{ik|\mathbf{x}-\mathbf{x}_p|}\right) \tag{4.11}$$

We now give numerical results for the NAH problem for the two proposed three-dimensional geometries (spherical and cuboid shapes) using IBEM. As before, all numerically estimated integrals are computed using 3×3 point product Gaussian quadrature

Figure 4.2 shows the reconstructed Neumann data on Γ for the two geometries proposed using different positions of the point sources to generate the exterior pressure data. The values of λ used are stated in the figure. Figure 4.3 displays the exact Neumann data on Γ using different positions of the point sources to generate the exterior pressure data.

The first rows in Figure 4.2 and Figure 4.3 display the reconstructed and the exact Neumann boundary data for a point source at $(0, 0, 0)$, respectively. The corresponding plots show that there is a good agreement between the reconstructed Neumann boundary data and the true solution values. By good agreement, we mean that the accuracy is comparable to the level of noise added, which in the results here is taken to be 15%, i.e., $w = 0.15$, see equation (4.8). The results in the second rows of Figure 4.2 and Figure 4.3 demonstrate a loss of symmetry when the point source is moved from $(0, 0, 0)$ to $(0, 0, 0.1)$, since the point source has moved upwards away from the centre of the object. The third rows of Figure 4.2 and Figure 4.3 illustrate the effect of the downward movement of the acoustic point source to $(0, 0, -0.1)$. Figures 4.2 and 4.3 show that there is a good agreement between the reconstructed Neumann boundary data and the true solution values, particularly for the cuboid case. Therefore the NAH problem has been successfully numerically modelled for general three-dimensional geometries using the IBEM. From the above results, one can see that although NAH is an ill-posed inverse problem, applying a regularisation method such as Tikhonov regularisation can lead to reasonably accurate reconstructions of the boundary data.

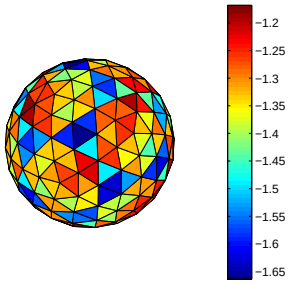

(a) Sphere; point source at (0,0,0), $\lambda = 0.0870$.

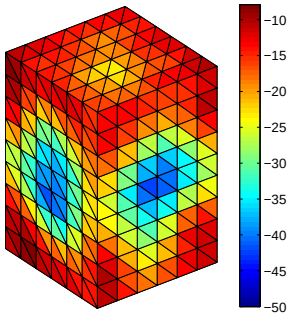

(b) Cuboid; point source at (0,0,0), $\lambda = 0.0107$.

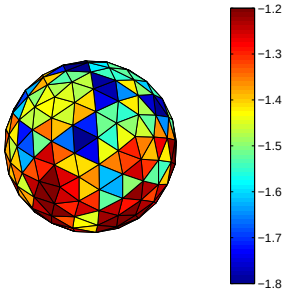

(c) Sphere; point source at (0,0,0.1), $\lambda = 0.0870$.

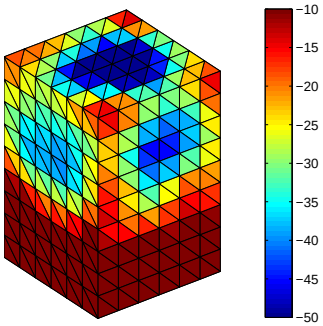

(d) Cuboid; point source at (0,0,0.1), $\lambda = 0.0093$.

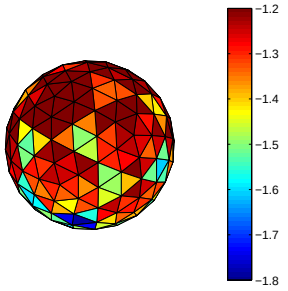

(e) Sphere; point source at (0,0,-0.1), $\lambda = 0.0870$.

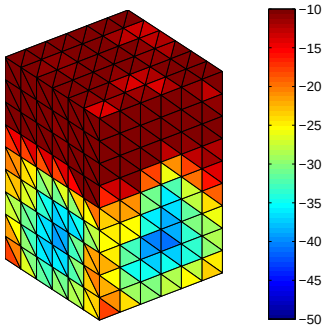

(f) Cuboid; point source at (0,0,-0.1), $\lambda = 0.0093$.

Figure 4.2: The reconstructed Neumann boundary data on Γ for different positions of the point source used to generate the exterior pressure data with $k = 1$.

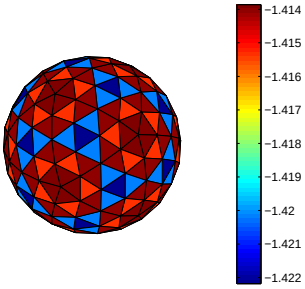

(a) Sphere; point source at (0,0,0).

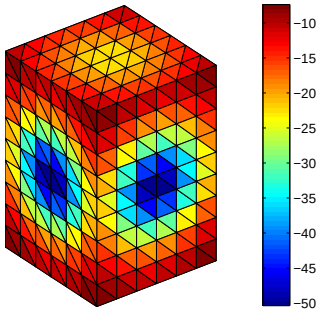

(b) Cuboid; point source at (0,0,0).

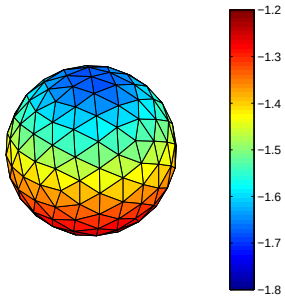

(c) Sphere; point source at (0,0,0.1).

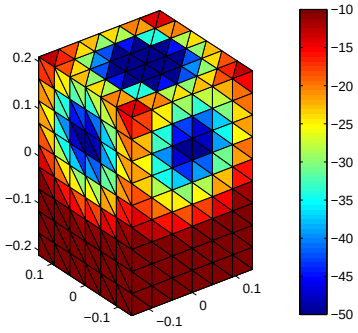

(d) Cuboid; point source at (0,0,0.1).

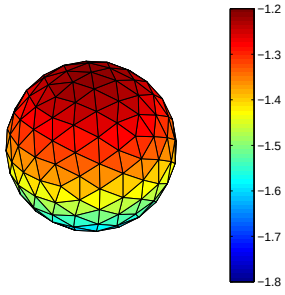

(e) Sphere; point source at (0,0,-0.1).

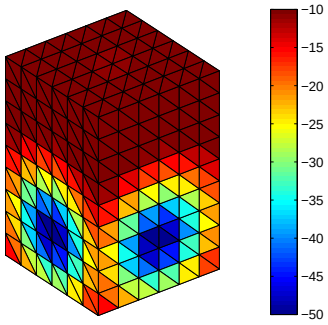

(f) Cuboid; point source at (0,0,-0.1).

Figure 4.3: The exact Neumann boundary data on Γ for different positions of the point source used to generate the exterior pressure data with $k = 1$.

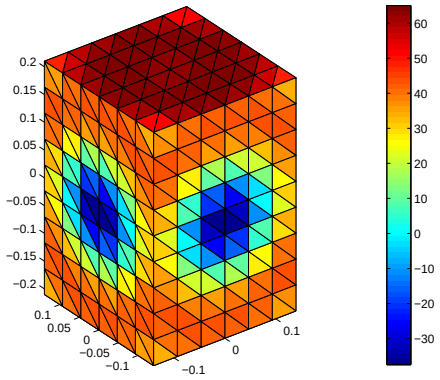

(a) Exact solution; point source at (0, 0, 0).

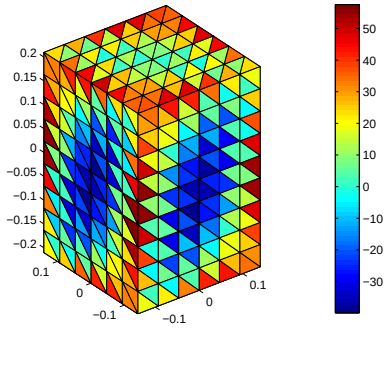

(b) Reconstructed solution; point source at (0,0,0).

Figure 4.4: The exact and reconstructed Neumann boundary data on Γ for exterior pressure data with $k = 17.52$, corresponding to an approximate interior resonance.

We now investigate the behaviour of the method for an alternative value of the wavenumber k. In particular, we consider how the method performs when k is chosen to correspond to a non-uniqueness frequency or resonance of the associated interior problem. That is, a resonance of the interior Helmholtz problem inside Ω_- with homogeneous Neumann boundary conditions. In Chapter 2 we identified one of these critical wavenumbers of the cuboid studied here numerically, at approximately $k = 17.52$. The results shown in Figure 4.4, again with 15% added noise, demonstrate that even though $k < k_{\text{nyq}}$, the accuracy of the model becomes degraded and the interior resonance frequencies pose problems for the IBEM for exterior problems, see also Ref. [2]. It was found in Ref. [2] that these problems can be overcome by using a Burton-Miller type integral equation formulation instead, where one takes a linear combination of the surface Helmholtz integral equation (2.17) and its directional derivative with respect to $\hat{\mathbf{n}}$. Other methods, such as

the Combined Helmholtz Integral Equation Formulation (CHIEF) could also be applied to cure the problem at critical values of k, see Amini *et al.* [23] for a survey of these methods.

4.5 Summary

In this chapter, the boundary integral equations for the Helmholtz equation have been reformulated to solve the inverse problem of NAH. Reconstructions of the Neumann boundary data have been computed on general three-dimensional structures, given noisy acoustic pressure data in the exterior domain. However, the application of IBEM is a complicated and computationally intensive process, particularly if additional measures are required to handle critical values of the wavenumber k. In the next chapter we will aim to develop more easily implementable and computationally efficient approaches by studying the method of superposition.

Chapter 5

Method of superposition

5.1 Introduction

In this chapter, we introduce the method of superposition (MoS) and discuss how it can be applied to numerically solve the forward Neumann problem of the Helmholtz equation. We compute numerical results for the forward Neumann problem given by a single point source in Ω_- using the MoS, with different values of wavenumber k and for different numbers of terms in the superposition. We then reformulate the method of superposition for the inverse problem of NAH. The results of numerical experiments using the MoS for the NAH problem are considered for the two geometrically different test problems given in Chapters 2 and 4. Finally, we compare the results of the MoS with those obtained by the IBEM, and the exact solution described in Chapter 4.

5.2 Method of superposition for the forward Neumann problem

The method of superposition is free from numerical integration and mesh generation, and is a boundary type meshless numerical method. The MoS was first proposed by Kupradze and Aleksidze in Ref. [58]. Mathon and Johnston [59] were among the first to provide the mathematical fundamentals for the MoS. In their work, the source strengths of MoS are considered as unknown variables over which the accuracy of the solution should be optimised. The MoS was first applied in acoustics by Koopman *et al.* in the late eighties [30].

The idea of the MoS is to approximate the solution of Helmholtz equation (2.3) ϕ by a linear combination of fundamental solutions of the form:

$$\phi(\mathbf{x}) \approx \sum_{j=1}^{n} \phi_j \; G_k(\mathbf{x}, \mathbf{y}_j), \tag{5.1}$$

where G_k is the fundamental solution of the Helmholtz equation defined in (2.8). In this section we consider the solution of the forward Neumann problem as discussed in Chapter 2. In this problem, we need to find the source strengths ϕ_j, $j = 1, ..., n$, given the Neumann boundary data $\partial\phi/\partial\hat{\mathbf{n}}$ on Γ.

In order to find ϕ_j for $j = 1, 2, ..., n$ we therefore solve

$$\frac{\partial\phi(\mathbf{x})}{\partial\hat{\mathbf{n}}} = \sum_{j=1}^{n} \phi_j \frac{\partial G_k(\mathbf{x}, \mathbf{y}_j)}{\partial\hat{\mathbf{n}}}, \tag{5.2}$$

where $\mathbf{y}_j$, $j = 1, ..., n$ are the locations of a set of charge points on an interior source surface inside Ω_-. To obtain a set of n equations to solve for our n unknowns ϕ_j, we evaluate (5.2) at a set of collocation points $\mathbf{x} = \mathbf{x}_i \in \Gamma$ for $i = 1, 2, ..., n$. This leads to solving the set of equations

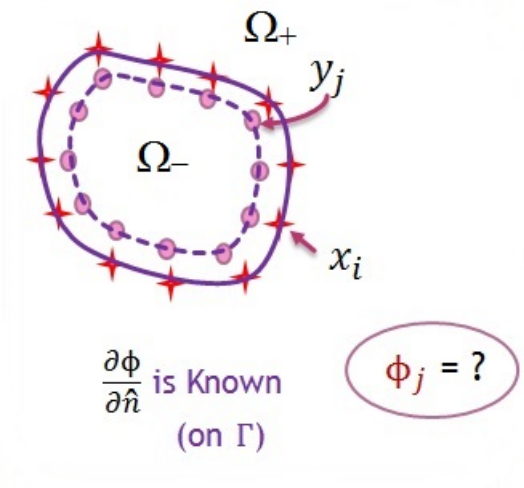

Figure 5.1: Problem setup for the MoS for the forward Neumann problem.

$$\frac{\partial \phi(\mathbf{x}_i)}{\partial \hat{\mathbf{n}}} = \sum_{j=1}^{n} \phi_j \frac{\partial G_k(\mathbf{x}_i, \mathbf{y}_j)}{\partial \hat{\mathbf{n}}}. \tag{5.3}$$

The collocation points are taken to be the centroids of the triangular elements from a BEM mesh. Whilst the MoS is in principle a mesh free method, we find it convenient to make use of the BEM meshes used in Chapters 2 and 4 to help us select the collocation points on our three dimensional objects. Equation (5.3) may be expressed in matrix-vector form by setting $\mathbf{v}$ to be the vector containing the entries $\frac{\partial \phi(\mathbf{x}_i)}{\partial \hat{\mathbf{n}}}$ and $\boldsymbol{\phi}$ to be the vector containing the entries ϕ_i for $i = 1, 2, ..., n$. Setting the matrix K to contain the entries $K_{ij} = \frac{\partial G_k}{\partial \hat{\mathbf{n}}}(x_i, y_i)$ then we obtain the matrix system $\mathbf{v} = K\boldsymbol{\phi}$, which we solve for $\boldsymbol{\phi}$. The internal charge points are positioned on a surface inside Ω_-, which is just a scaled-down version of Γ with scaling factor $\alpha \in (0, 1)$. For example, a value of $\alpha = 0.5$ corresponds to a surface of internal charge points whose dimensions are exactly half those of Γ. Assuming that Ω_- is centred at the origin, we simply take a collocation point $\mathbf{x}_i \in \Gamma$ and

multiply by α to obtain the corresponding internal charge point $\mathbf{y}_i$ thus,

$$\mathbf{y}_i = \alpha \mathbf{x}_i \tag{5.4}$$

for $i = 1, 2, ..., n$. In the next section we put these ideas into practice via a number of numerical experiments.

5.3 Numerical results for the forward Neumann problem

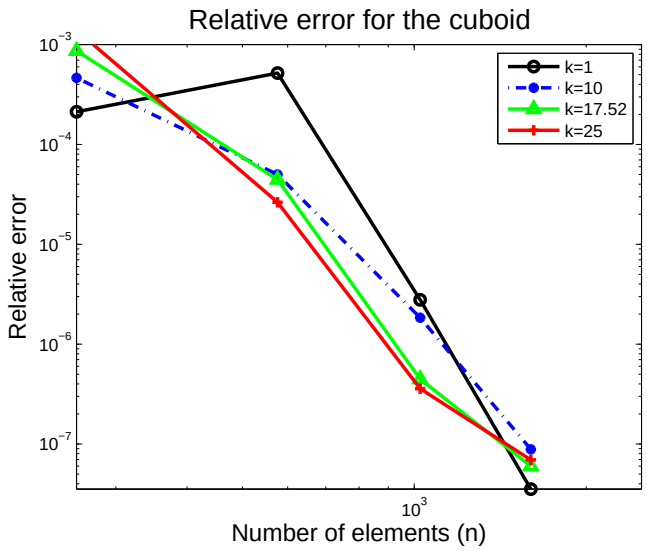

Figure 5.2: Relative error for the cuboid using the MoS.

We again consider numerical results for the acoustic radiation from two geometrically different test problems as described in Section 2.4. As in Chapter 2, the Neumann boundary data will be generated by a single unit point source at $(0, 0, 0.1) \in \Omega_-$, where Ω_- is centred at the origin. Figures 5.2 and 5.3 show the relative errors when using the MoS to solve the exterior Neumann problem with

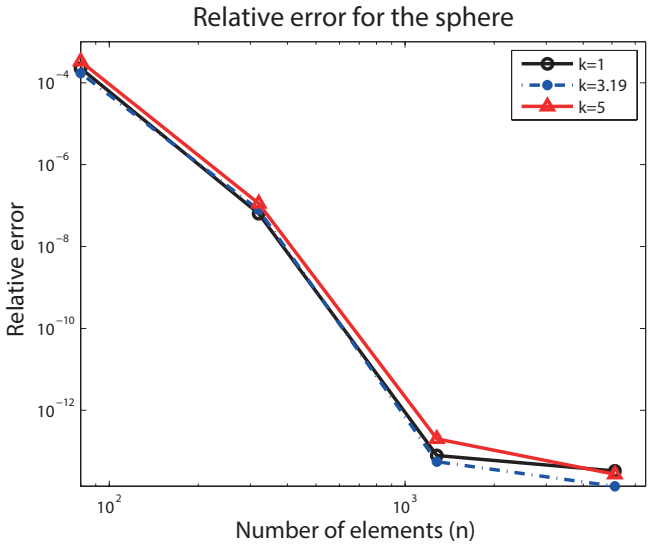

Figure 5.3: Relative error for the sphere using the MoS.

different values of k and n. For the choice of the parameter α, we note that taking too small a value of α will lead to severe ill conditioning as the charge points become very close together [30], but Ref. [30] also suggests that choosing too large a value of α will lead to poor results. A choice in the range $\alpha = (0.1, 0.6)$ is advised in Ref. [30]. For all the numerical results in this section we therefore set the parameter $\alpha = 0.5$.

We notice in both cases that the errors are generally decreasing as the number of charge points n is increased, with the exception of one anomalous case. The results are plotted on a log-log scale and the errors become very small indeed for $n > 1000$. For the case of the sphere shown in Fig. 5.3, the errors are close to machine precision. Note that these errors are far smaller than those arising in the BEM, as can be seen from the results in Tables 2.1 and 2.2. This increase in accuracy compared with the BEM is a great advantage when one also considers the relative simplicity and efficiency of the corresponding computations. Figures 5.2 and 5.3 also show results for wavenumbers k corresponding to internal resonances

of the radiating objects, as discussed in Chapter 2. We notice that for the MoS, it is not the resonances internal to Γ that pose problems. Instead, it is the interior resonances of the surface of charge points inside Ω_- where issues can arise. For $\alpha = 0.5$ as used in these examples, an interior resonance for the surface of charge points inside the cuboid will be found at approximately $k = 17.52/\alpha \approx 35$.

Table 5.1: The relative errors for different k values, including the interior resonance at $k = 35.08423$ with different numbers of charge points n inside the cuboid.

n	Err $(k = 17.52)$	Err $(k = 35.08423)$	Err $(k = 36)$
256	1.439e-03	0.0851	7.327e-04
576	2.637e-05	0.2661	2.162e-05
1024	3.582e-07	0.1069	4.403e-07
1600	6.929e-08	0.1269	3.559e-07

Table 5.1 compares the relative errors for different numbers of interior charge points n, including at a wavenumber $k = 35.08423$ corresponding to an approximate interior resonance of the surface of charge points for the cuboid example. The errors at $k = 17.52$, corresponding to an approximate interior resonance of the cuboid Ω_- and for a larger wavenumber $k = 36$ are also given for reference. One can clearly see a significantly larger error for $k = 35.08423$ and the peak in the error is local to this value of k. For $k = 17.52$ and $k = 36$, the errors are far lower and the fast convergence and small errors are similar to the results shown in Figure 5.2. Figure 5.4 shows the results of Table 5.1 in graphical form, including the large errors at $k = 35.08423$. For this choice of wavenumber there is also no evidence of convergence since the error actually increases as n is increased from 256 to 576 and from 1024 to 1600. However, it is very simple to obtain accurate results with the MoS for $k = 35.08423$. All that we need to do is change the value

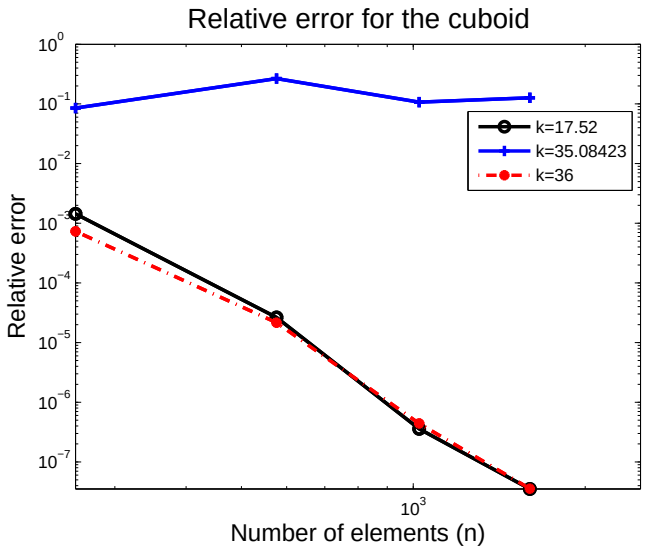

Figure 5.4: relative error for the MoS for the forward Neumann problem including a problematic k value.

of α. Doing this leads to the results shown in Table 5.2, which repeats the results of Table 5.1, but with $\alpha = 0.4$. In this case the results all reflect those shown in Figure 5.2.

Table 5.2: The relative errors for different k values, with $\alpha = 0.4$ and for different numbers of charge points n inside the cuboid.

n	Err $(k = 17.52)$	Err $(k = 35.08423)$	Err $(k = 36)$
256	2.702e-04	1.408e-03	2.333e-03
576	1.084e-05	8.161e-06	8.613e-06
1024	6.113e-07	2.162e-07	4.948e-07
1600	1.637e-07	1.168e-07	3.818e-08

5.4 Method of superposition for the inverse NAH problem

In the NAH problem, we are given values of the acoustic pressure ϕ at a discrete set of points in the acoustic near field within Ω_+. We will assume that the data points $\mathbf{x}_i$, $i = 1, ..., m$ lie on a surface $\Gamma^* \subset \Omega_+$. Note that the pressure data is usually obtained from measurements using a microphone array. However, in this chapter, we generate the pressure data numerically as described in Section 4.4. The NAH problem is to use the given pressure data to recover the Neumann boundary data on Γ. Solving this problem via the method of superposition is then a matter of finding the set of source strengths ϕ_j, $j = 1, ..., n$, that reproduce the acoustic pressure data to some desired accuracy in the least squares sense. That is, ϕ_j are chosen so that the ℓ^2 norm of the residual vector $\mathbf{r}$, with entries given by

$$r_i = \phi(\mathbf{x}_i) - \sum_{j=1}^{n} \phi_j G_k(\mathbf{x}_i, \mathbf{y}_j) \tag{5.5}$$

for $i = 1, .., m$, is smaller than a desired error tolerance. Once the source strengths have been obtained then the Neumann boundary data can be recovered from

$$\frac{\partial \phi}{\partial \hat{\mathbf{n}}}(\mathbf{x}) \approx \sum_{j=1}^{n} \phi_j \frac{\partial G_k}{\partial \hat{\mathbf{n}}}(\mathbf{x}, \mathbf{y}_j), \tag{5.6}$$

where $\hat{\mathbf{n}}$ is the outward unit normal to Γ. As shown in Appendix B, the linearized Euler equation for time harmonic waves leads to the following simple relationship between the Neumann boundary data computed here, and the normal velocity v of the radiating object:

$$\frac{\partial \phi}{\partial \hat{\mathbf{n}}} = i\omega\rho v. \tag{5.7}$$

As described in Section 4.3, regularization is always required in general, even for $n = m$, since NAH is an ill-posed inverse problem (see for example [2]). For experimental problems, the pressure measurements will contain errors and the

ill-posedness of the problem means that these errors are amplified in the (unregularized) solutions, often rendering them meaningless. Most previous work on NAH has concentrated on using Tikhonov regularization, together with generalized cross validation (GCV) [36]. We will therefore use this combination of methods for the numerical results in the next section.

5.5 Numerical results for the inverse problem

In this section, the results of numerical experiments using the method of superposition for the NAH problem are considered. The same two three-dimensional geometries described in Section 4.4 are considered for verification of the MoS method. That is, a cuboid and a unit sphere with the same dimensions and the same numbers of charge and collocation points are treated. As in the case of the forward Neumann problem described in Section 5.2, we choose the parameter $\alpha = 0.5$, which governs the locations of the MoS internal charge points. The results obtained using the MoS are compared to the IBEM, using the same three point sources to generate the pressure data with wavenumber $k = 1$, as described in Section 4.4. The locations of the external pressure data sampling points are also chosen as described in Section 4.4. That is, in the case of the cuboid they are placed at a distance 0.05m from Γ in the direction normal to the surface. For the sphere, they are placed at 0.2m from Γ, again in the direction normal to the surface. We also introduce uniformly distributed white noise to the generated pressure data as before, where the ℓ^2 norm of the added noise vector is 5% of the ℓ^2 norm of the noise free data vector.

In order to treat the ill-posedness of the inverse NAH problem, we apply Tikhonov regularisation as described in Section 4.3. However, rather than use

the exact solution to determine the regularisation parameter λ that leads to the minimal error, we instead apply Generalised Cross Validation (GCV). The reason for this is to provide a fair means of comparison for the sparse regularization methods to be introduced in the next chapter. The GCV is the most popular method for selecting the parameter λ for NAH applications [36]. The main advantage of the GCV is that it does not require prior knowledge of the noise variance. This method eliminates a measurement point at a time and compares the reconstruction at the missing data point with the real data there, minimizing this difference [36]. The function to be minimized for the standard form of Tikhonov regularization is [36, 60]

$$J(\lambda) = \frac{\|\mathbf{r}\|^2}{[Tr(I - AR_\lambda)]_2^2}, \tag{5.8}$$

where the entries of the matrix A are given by

$$A_{ij} = G_k(\mathbf{x}_i, \mathbf{y}_j) \tag{5.9}$$

and

$$R_\lambda = (A^T A + \lambda^2 L^T L)^{-1} A^T, \tag{5.10}$$

using the notation of Section 4.3. We take L to be the identity matrix as before and note that $\mathbf{r}$ is the residual vector defined in equation (5.5), where $\|\mathbf{r}\|$ denotes its ℓ^2 norm. The notation Tr refers to the trace of the matrix, meaning the sum of its diagonal entries. A derivation of (5.8) can be found in Section 2 of [60], and is based on the definition of the GCV as the minimiser of

$$\|AR_\lambda \mathbf{b} - \mathbf{b}\|_2 = \|(I - AR_\lambda)\mathbf{b}\|_2, \tag{5.11}$$

where $\mathbf{b}$ is the vector of pressure data values as before. We implement the above described regularisation procedure very simply by making use of the 'Regtools' Matlab toolbox by Hansen [61].

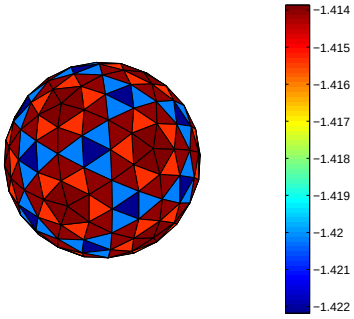

(a) Sphere; point source at (0,0,0)

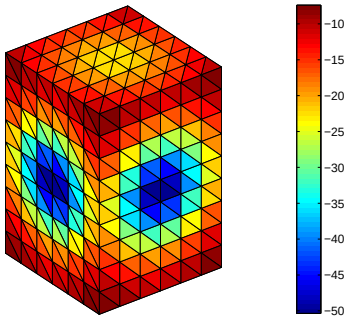

(b) Cuboid; point source at (0,0,0)

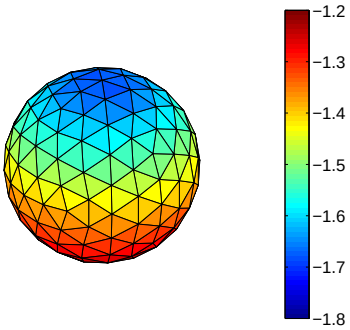

(c) Sphere; point source at (0,0,0.1)

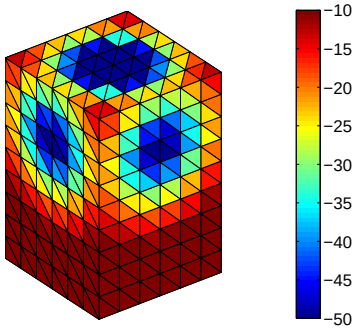

(d) Cuboid; point source at (0,0,0.1)

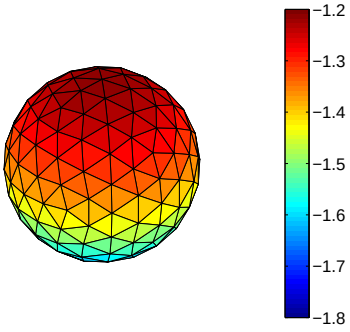

(e) Sphere; point source at (0,0,-0.1)

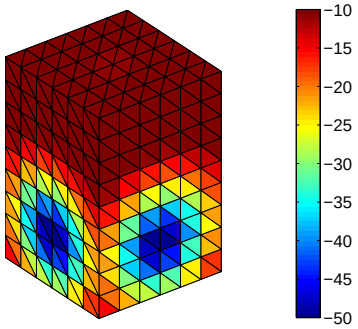

(f) Cuboid; point source at (0,0,-0.1)

Figure 5.5: The reconstructed Neumann boundary data using the MoS for different positions of the point source used to generate the exterior pressure data with $k = 1$.

We now give the numerical results for the NAH problem using the MoS and compare with the results that are obtained by the IBEM and the exact solution shown in Figures 4.2 and 4.3, respectively. The first rows in Figure 5.5 and Figure 4.3 demonstrate the reconstructed solution using the MoS and the exact solution for a point source at (0,0,0), respectively. The comparison between these two plots shows that there is a good agreement between the solutions obtained by the MoS method and the true solution values. The results shown in the middle rows in Figure 5.5 and Figure 4.3 display the reconstructed solution found by the MoS and the exact Neumann boundary data for the second point source at (0,0,0.1). In both cases, we can see that the peak moved upwards away from the centre of the object and this result is as would be expected. The last row in Figure 5.5 and Figure 4.3 shows the comparison between the solution obtained by the MoS method and the exact solution for the point source at (0,0,-0.1). Comparing Figures 5.5 and 4.3 clearly demonstrates that the MoS is effective and gives a precise result for both the cuboid and the sphere. It is also evident from comparing Figure 5.5 with both Figure 4.2 showing the IBEM results, and Figure 4.3 showing the exact solution, that the MoS gives more accurate reconstructions than the IBEM. This is particularly evident for the case of the sphere.

Table 5.3 compares the IBEM and the MoS with respect to the computational time to obtain the results, and the errors. The comparison was made for both geometrical configurations (cuboid and sphere), using a Windows laptop with an Intel Core i5, 2.5 GHz processor. For the cuboid shape, the first three columns show that the error using the IBEM is much greater than the error for the MoS. The errors for the MoS are typically around half the errors for the IBEM. Furthermore, for the IBEM the computational time is approximately twenty times as long as

for the corresponding experiment using the MoS. Clearly the MoS is much faster and reaches a superior result compared to the IBEM. A similar pattern of results an be observed for the sphere, except now the improvement in the error values is even more stark. Again, the computations are faster using the MoS by a factor of approximately twenty. We can also notice from Table 5.3 that the smallest errors and computational times are observed when the source point generating the pressure data is in the centre (0,0,0). This can possibly be attributed to the fact that the solution to be reconstructed has more symmetry and less local variability in this case.

Table 5.3: Comparison between the MoS and IBEM in regards to the computational time and the error.

Cuboid ($n = 576$)				
Source Point Position	IBEM		MoS	
	Error	Time (sec)	Error	Time (sec)
$(0, 0, 0)$	0.1509	224.46	0.05090	11.46
$(0, 0, 0.1)$	0.1707	228.27	0.0899	11.47
$(0, 0, -0.1)$	0.1781	237.87	0.0979	11.36
Sphere ($n = 320$)				
Source Point Position	IBEM		MoS	
	Error	Time (sec)	Error	Time (sec)
$(0, 0, 0)$	0.0871	19.97	0.0065	1.08
$(0, 0, 0.1)$	0.0858	19.35	0.0074	1.14
$(0, 0, -0.1)$	0.0915	19.39	0.0099	1.16

5.6 Summary

In this chapter we introduced the MoS and applied it to numerically solve both the forward Neumann problem, and the NAH problem. The numerical results of using the MoS for the forward Neumann problem showed fast convergence leading to smaller errors than the corresponding numerical experiments using the BEM in Chapter 2. This provided motivation to further apply the MoS to solve the NAH problem. The results for the numerical experiments utilizing the MoS for the inverse problem of NAH demonstrated that the MoS can give more accurate solutions than the inverse BEM with faster computational times. Moreover, the treatment of non-uniqueness frequencies at interior resonances is simpler for the MoS compared to the BEM. In the next chapter, we will study the combination of the MoS with sparse reconstruction methods with the aim of generating solutions more efficiently using fewer charge points, but without any significant loss of accuracy.

Chapter 6

Sparse reconstructions for the inverse method of superposition

6.1 Introduction

In this chapter we introduce the theory of compressive sampling, including the key concepts of sparsity and incoherence. We then discuss the possibility of a sparse solution representation using ℓ^1 optimization techniques based on the method of superposition applied to three dimensional NAH problems. The results of numerical tests where the exterior acoustic field is generated by a monopole point source inside the structure will be considered for a cuboid that has similar dimensions to a typical loudspeaker. We will also study the case of reconstructing the vibrations of a locally vibrating structure, where only a small region of the structure is vibrating and the location of any singularities of the continuation of the acoustic field into Ω_- are unknown, which is usually the case in practice.

6.2 Compressive sampling

The traditional method of sampling and reconstruction of a desired quantity from the samples follows Shannon's sampling theorem, which states that the sampling rate must not be less than twice the maximum frequency present in the signal (the so-called Nyquist rate): see Appendix C. This principle underlies nearly all signal acquisition procedures in end user audio and visual electronics, medical imaging devices and radio receivers [62], including signal (or pressure data) acquisition in Nearfield Acoustic Holography. Compressive sampling, also known as compressed sensing (CS), is an innovative sensing/sampling paradigm, which goes in contradiction of the common wisdom in data acquisition. The theory of CS declares that one can recover signals and images from far fewer samples or measurements than traditional methods use. In order to make this possible, CS requires two principles: sparsity, which relates to the signals of interest, and incoherence, which relates to the sensing modality.

Sparsity refers to the concept that the "information rate" of a continuous signal may be much smaller than recommended by its bandwidth, or that a discrete signal be dependent on a number of degrees of freedom that is comparably much smaller than its (finite) length. Concisely, CS exploits that many natural signals are sparse or compressible, in the sense that they have concise representations when expressed in an appropriate basis. Incoherence exploits the duplicity between physical space and frequency space (or k-space) and expresses the notion of objects having a sparse representation in a particular basis. Fundamentally, this means that CS exploits that a signal which is spread out in physical space, such as a fixed frequency wave sampled in NAH, has a very localised representation in k-space. In this case it is just a Dirac delta spike corresponding to the single fixed frequency. However, incoherence states that unlike the signal of interest, the sam-

pling/sensing waveforms have a very dense representation. The key observation is that one can design effective sensing or sampling procedures that capture the valuable information content entrenched in a sparse signal and condense it into a small amount of data. These procedures are non-adaptive and just require associating the signal with a small number of fixed waveforms, which are incoherent with the sparsifying basis. These sampling procedures permit a sensor to efficiently seize the information in a sparse signal without trying to understand that signal. Compressive sampling is a very simple and effective signal acquisition procedure which samples in a signal independent fashion, at a low rate and later uses computational power for reconstruction from what appears to be an incomplete set of measurements [62].

6.3 Sparse reconstructions for NAH

The work reported in this section is taken from our paper [44]. Recall that the reconstruction of solutions to the NAH problem using the MoS requires that we somehow control the size of the ℓ^2 norm of the residual vector $\mathbf{r}$ defined in (5.5). In particular, making $\|\mathbf{r}\|_2$ as small as possible would lead to the best possible reconstruction, and this is the aim of Tikhonov regularization. Note that we have introduced the notation $\|\mathbf{r}\|_2$ for the ℓ^2 norm of $\mathbf{r}$, in order to distinguish it from the ℓ^1 norm $\|\mathbf{r}\|_1$ which will also be needed later. The application of Tikhonov regularization to minimise $\|\mathbf{r}\|_2$ may be written concisely as follows [41]:

$$\hat{\boldsymbol{\phi}} = \arg\min_{\boldsymbol{\phi}} \left\{ \|\mathbf{r}\|_2^2 + \lambda^2 \|L\boldsymbol{\phi}\|_2^2 \right\}, \tag{6.1}$$

where L is the Tikhonov matrix (most simply chosen as the identity matrix as before) and $\lambda > 0$ is a regularization parameter to be determined. We have also introduced the notation $\boldsymbol{\phi} = [\phi_1 \ \phi_2 \ \ldots \ \phi_n \,]^T$ for the vector containing the source

strengths, and likewise $\hat{\boldsymbol{\phi}}$ is the vector containing the regularized and reconstructed source strengths for the n interior charge points.

In this chapter, we adopt an alternative regularization approach of Chardon *et al.* [41], which favours sparse representations of the solution. In other words, it (approximately) minimizes $|\boldsymbol{\phi}|_0$, the number of non-zero entries of $\boldsymbol{\phi}$. As noted by Chardon *et al.* [41], the possibility of a sparse reconstruction is highly dependent on the basis functions used to represent the solution. In the superposition method, these basis functions are the fundamental solution of the Helmholtz equation at a set of distinct interior charge points. The results in Koopman *et al.* [30] suggest the feasibility of sparse solution representations for a large range of wavenumbers using the superposition method. The results presented in the next section will investigate the conditions whereby high quality sparse representations are indeed possible. For the examples considered here we expect that the quality of the solutions attainable will be highly dependent on the location of the interior charge points used for the superposition. The acoustic pressure data is created by either a single interior monopole, or by applying the BEM to approximate the acoustic field radiated from a relatively small vibrating patch. We will investigate whether the sparse reconstruction approach can pick out solutions $\boldsymbol{\phi}$ that make use of the underlying sparsity in these examples, where this sparsity arises either due to the low number of monopoles needed to generate the field in the former case, or due to the relatively small region over which the reconstructed field is dominant in the latter case.

Directly minimizing $|\boldsymbol{\phi}|_0$ is often intractable due to non-convexity [41], see Appendix D for a brief introduction to optimization and the importance of convexity. We therefore instead seek to minimize the ℓ^1 norm

$$\|\boldsymbol{\phi}\|_1 = \sum_j |\phi_j|. \tag{6.2}$$

The use of the ℓ^1 norm allows one to apply powerful convex optimization algorithms and still promotes sparsity by making many of the components of $\boldsymbol{\phi}$ negligibly small, meaning that they can be well-approximated by zero without degrading the reconstructed solution. The following procedure will be applied to find a sparse representation $\hat{\boldsymbol{\phi}}$ of the source strengths $\boldsymbol{\phi}$:

$$\hat{\boldsymbol{\phi}} = \arg\min_{\boldsymbol{\phi}} \|\boldsymbol{\phi}\|_1 \;\; \text{subject to} \;\; \|\mathbf{r}\|_2^2 \leq \epsilon. \tag{6.3}$$

This procedure will be implemented using the convex optimization toolbox CVX [63]. This procedure requires a data fidelity constraint ϵ to be specified. Choosing this parameter involves a trade off between allowing sparser solutions with larger values of ϵ and achieving more accurately reconstructed solutions with smaller values of ϵ. Chardon *et al.* [41] recommend a choice of ϵ of the order 20% to 30% of the ℓ^2 norm of the measured pressure data. However, a good choice of ϵ is likely to depend on how noisy the pressure data is and hence will be problem dependent.

For completeness, and to emphasize the links between the ℓ^1 regularization approach and Tikhonov regularization we note that (6.3) may be expressed in the form [41, 64]

$$\hat{\boldsymbol{\phi}} = \arg\min_{\boldsymbol{\phi}} \left\{ \|\mathbf{r}\|_2^2 + \lambda^2 \|\boldsymbol{\phi}\|_1 \right\}. \tag{6.4}$$

This procedure is known as the basis pursuit denoising (BPDN) and is introduced in Section 5.1 of Ref. [64], where the interested reader can find further details, including a discussion of suitable choices of λ in the presence of standard Gaussian noise. Here, we simply note the parallels between the expression (6.4) and Eq. (6.1), and remark that one of the main differences is the norm employed in the final term. In particular, the ℓ^1 norm replaces the square of the ℓ^2 norm in the Tikhonov case, and it is this difference that promotes sparsity in the ℓ^1 approach. Note also that the ℓ^1 approach (6.1) does not seek to minimise $\|\mathbf{r}\|_2$ like Tikhonov regularization (6.4). Instead it seeks out the solution with optimal sparsity, pro-

vided $\|\mathbf{r}\|_2$ is below some acceptable tolerance level controlled by the parameter ϵ. The differences between these two approaches will be investigated numerically in the next section.

6.4 Numerical results

The numerical results reported in this section are taken from our paper [44]. Numerical results will be computed for acoustic radiation from the same cuboid as before, which has similar dimensions to a typical loudspeaker cabinet (0.28m $\times$ 0.28m $\times$ 0.42m). As before, we will use a triangulation of the cuboid to generate the points at which the pressure data are computed, as well as the internal charge points and the points at which we reconstruct the solution on Γ. In particular, for a given triangulation of Γ we reconstruct the Neumann boundary data at the centroid of each triangle and project (from each centroid) a distance δ along the normal vector to Γ into Ω_+ to obtain the points where the exterior pressure data is sampled. The internal charge points are positioned on a cuboid inside Ω_-, which is just a scaled down version of Γ with scaling factor $\alpha \in (0, 1)$, as in Chapter 5.

Initially we reconstruct the boundary data generated by a point source at $\mathbf{x}_0 = (0,\ 0,\ z_0) \in \Omega_-$, where Ω_- is centred at the origin. The pressure data is therefore of the form

$$(\boldsymbol{\phi}_0)_j = a\frac{e^{ik|\mathbf{x}_0-\mathbf{x}_j|}}{|\mathbf{x}_0-\mathbf{x}_j|}, \qquad j = 1, ..., n, \tag{6.5}$$

where $a \in \mathbb{C}$ is the strength of the source, which in these examples is arbitrarily taken to be $a = 3 - i$. The boundary data generated at $\mathbf{y} \in \Gamma$ may also be obtained for the case of a point source at $\mathbf{x}_0 = (0,\ 0,\ z_0)$ by replacing $\mathbf{x}_j$ in (6.5) by $\mathbf{y} \in \Gamma$, differentiating in the direction of $\mathbf{n}_y$ and evaluating at the centroids of the triangulation $\mathbf{y} = \mathbf{y}_j$ for $j = 1, ..., n$ to give

$$(\mathbf{v})_j = a\left(\frac{\mathbf{n}_{y_j}\cdot(\mathbf{x}_0-\mathbf{y}_j)}{|\mathbf{x}_0-\mathbf{y}_j|^3}(1-ik|\mathbf{x}_0-\mathbf{y}_j|)e^{ik|\mathbf{x}_0-\mathbf{y}_j|}\right), \qquad j=1,...,n. \tag{6.6}$$

In equation (6.6), $\mathbf{v}$ is the vector of values of $\partial\phi/\partial\hat{\mathbf{n}}$ at the points $\mathbf{y}_j$ on Γ. Using this calculation it is possible to verify the accuracy of the (Tikhonov or ℓ^1) regularised approximate solutions with different wavenumbers and singularity point positions z_0. We will also investigate the behaviour of the method at irregular frequencies of the volume enclosed by the interior charge points, and the dependence on the dimensions / location of the interior charge point surface controlled by the parameter α.

Uniformly distributed and additive white noise will be applied to $\boldsymbol{\phi}_0$ in order to more closely replicate experimental observations, as in Chapters 4 and 5. We denote the added noise vector as $\mathbf{w}$ and specify the ratio

$$w = \frac{\|\mathbf{w}\|_2}{\|\boldsymbol{\phi}_0\|_2}, \tag{6.7}$$

referring to w as the level of added noise in the sequel.

Finally, we consider the case of reconstructing a locally vibrating structure, where only a small region of the structure is vibrating. Such an assumption is typical for the case of a loudspeaker and also allows us to study a case where the locations of any singularities of the continuation of the acoustic field into Ω_- are unknown, as is usually the case in practice. Here the acoustic pressure data will be generated using the boundary element method applied to the forward Neumann problem as described in Chapter 2. Through this example we demonstrate the broader applicability of the sparse reconstruction algorithm, where the measured signal should have a sparse structure, but not necessarily the basis for the superposition method.

6.4.1 Comparison with Tikhonov regularisation

First consider the case $k = 1$ and $z_0 = 0.05$, where the frequency is relatively low, is not close to an irregular frequency, and $\mathbf{x}_0$ is relatively close to the origin and will lie inside the surface on which the interior charge points are located. Under such conditions the superposition method is expected to work well. Table 6.1 shows the ℓ^2 percentage errors in the reconstructed Neumann boundary data for three different regularisation strategies and differing noise levels. The three solution strategies to be compared are (i) ℓ^1 regularisation and taking the sum over all interior charge points, (ii) sparse ℓ^1 regularisation where only contributions from dominant charge points are considered, and (iii) standard Tikhonov regularisation using GCV (see Section 5.5) to determine the regularisation parameter. In the latter case the computations have been performed using Hansen's regularisation toolbox [61]. In the case of the sparse reconstruction, the criteria used to determine whether the jth charge point is dominant is if

$$\log\left(\frac{|\phi_j|}{\min_i |\phi_i|}\right) > \beta \log\left(\frac{\max_i |\phi_i|}{\min_i |\phi_i|}\right).$$

We will use the notation $N^*(\beta)$ for the number of dominant charge points satisfying this condition, taking $\beta = 0.5$ by default and so we denote $N^* = N^*(0.5)$. The ℓ^2 percentage error in the reconstructed solution $\hat{\mathbf{v}}$ is calculated using

$$\frac{\|\hat{\mathbf{v}} - \mathbf{v}\|_2}{\|\mathbf{v}\|_2} \times 100\%. \tag{6.8}$$

The pressure data are specified at a distance $\delta = 0.035$m from Γ and the internal source surface is scaled down to have dimensions $\alpha = 1/3$ the size of Γ. We note that these choices should lead to good results based on the fact that δ should be chosen small enough to capture evanescent contributions to the pressure field, but still large enough to be a practical distance for taking experimental measurements. For the parameter α, recall that a choice in the range $\alpha \in (0.1, 0.6)$ is advised in

Ref. [30]. It is also beneficial for the charge point surface to enclose any singularities of the associated interior problem [33]. For these experiments the number of charge points, the number of measurement points and the number of points at which we reconstruct the solution are all equal to 576. This is achieved by triangulating the internal source surface in an identical way to Γ and taking the charge points at the triangle centroids.

Table 6.1: The ℓ^2 percentage error in the reconstructed Neumann boundary data generated from a source point on the $z-$axis at $z_0 = 0.05$ with added noise and $k = 1$.

Noise level (%)	% error: ℓ^1 full	% error: ℓ^1 sparse	% error: Tikhonov
0	6.2091E-3	0.1097	1.009E-7
5	3.850	3.850	3.549
15	6.428	6.429	6.017

The results in Table 6.1 show that in the noise free case, the reconstruction errors for both the full ℓ^1 method and Tikhonov regularisation are very small, with Tikhonov reconstruction performing better. A sparse representation of the solution is not feasible here in general unless one of the charge points coincides with the monopole generating the acoustic field; the ℓ^1 optimisation identifies a relatively large number $N^* = 98$ of dominant sources and the error of the 'sparse' reconstruction increases significantly compared with the reconstruction using all 576 source points. However, once noise is present in the pressure data, then sparse representations of the solution can be obtained with a similar level of accuracy to the Tikhonov approach. The reason for this can be explained by considering how

the data fidelity parameter ϵ is chosen in (6.3). In particular we take

$$\epsilon = (\max\{\epsilon_{\min}, w\})^2 \|\phi_0\|_2^2, \tag{6.9}$$

where w is the level of noise added to the pressure data as before. Recall that larger choices of ϵ permit sparser solution representations. However, it only makes sense to choose a larger ϵ for noisy data, otherwise it leads to less accurate reconstructions. The parameter $\epsilon_{\min} \geq 0$ is included as a tolerance level that is used for the low or zero noise case. A relatively large choice of $\epsilon_{\min}$ will lead to sparser reconstructions at the expense of accuracy, and the converse is true for small $\epsilon_{\min}$. The results in this work have been obtained with $\epsilon_{\min} = 1\text{E-}6$.

Figure 6.1 highlights the differing nature of the solutions reconstructed using the Tikhonov and ℓ^1 approaches. The plots show that ℓ^1 regularisation is more effective at promoting sparsity in the case of noisy data, and hence larger values of the data fidelity constraint ϵ. In these cases the distribution of the size of the coefficients $|\phi_j|$, $j = 1, 2, ..., n$, is dominated by only a few values for the ℓ^1 approach, due to the minimisation of $\|\underline{\phi}\|_1$ in (6.3). In particular, when noise is added the solutions can be accurately reconstructed using only 10 to 15 of the 576 source points. For the Tikhonov reconstruction, sparsity is not promoted by the algorithm and the distribution of $|\phi_j|$ is more even. This is further illustrated in Figure 6.2, which shows the reconstructed solution with noise level $w = 0.15$ using each of the three solution strategies described above. The exact solution is also shown for reference.

In all three cases we achieve a faithful reconstruction of the Neumann data on the cuboid since the match to the exact solution is very good. Plots of the cases $w = 0$ and $w = 0.05$ are omitted for brevity, since as shown in Table 6.1, the reconstruction errors in these cases are even smaller and the likeness to the exact solution shown in Figure 6.2 would be even stronger. The main result of this section is that ℓ^1 sparse regularisation can give similar accuracy to Tikhonov

regularisation for noisy data, but with a small fraction of the number of charge points required to produce the reconstruction.

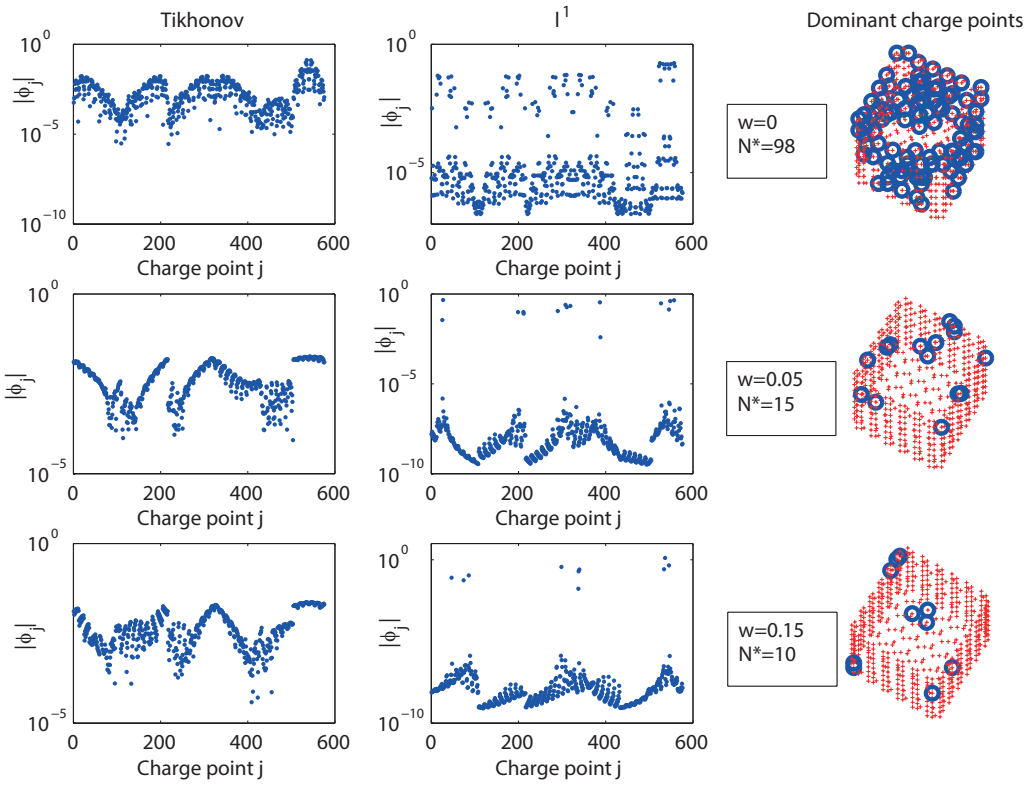

Figure 6.1: Left and centre columns: Comparison of the charge point strengths using the Tikhonov and ℓ^1 approaches for $k = 1$ and exterior pressure data generated by a point source at $(0, 0, 0.05)$. Right column: locations of the dominant charge points for the ℓ^1 approach. The top row shows the case of clean pressure data and the other rows show the results for differing levels of added noise w.

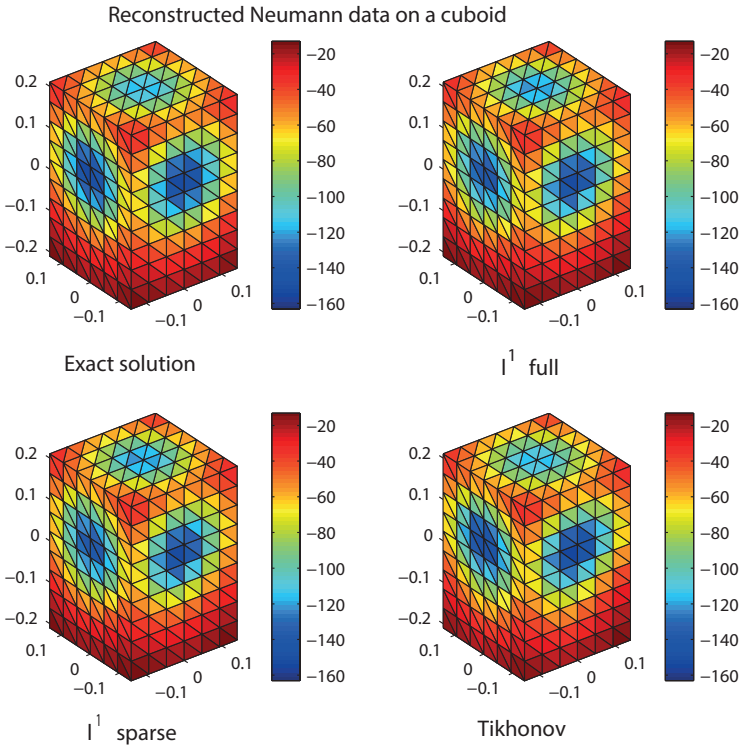

Figure 6.2: Neumann boundary data on a cuboid generated by a point source at $(0, 0, 0.05)$ with wavenumber $k = 1$ and 15% added noise. The plots compare the exact solution against those reconstructed using Tikhonov regularisation, the ℓ^1 approach with all charge points and the sparse ℓ^1 approach using only dominant charge points.

6.4.2 Higher and irregular frequencies

We now investigate the behaviour of the method for some potentially problematic choices of the wavenumber k. First we look at the case when the frequency is increased, including when the Nyquist frequency (see Appendix C) is exceeded. Since our measurements are taken at triangle centroids, then the resulting measurement grid is irregular and so the Nyquist frequency is not well-defined. We therefore

choose the Nyquist frequency associated with the regular grid given by the triangle vertices, as a value approximately representative of the Nyquist frequency. For the discretisation considered in the previous section with 576 triangles, the grid spacing is $\Delta x = 0.04667$, meaning that the wavenumber corresponding to the Nyquist frequency is $k_{\text{nyq}} = \pi/\Delta x = 67.32$. We also investigate the performance of the method close to other typical threshold frequencies for numerical solution approaches, such as the six grid points per wavelength rule of thumb for finite and boundary element methods, which gives a maximum wavenumber of $k = 22.44$ for the grid described above. The performance of the method at irregular frequencies will also be investigated. For the method of superposition, these irregular frequencies are the resonances of the region enclosed by the interior source surface as identified in Chapter 5. Numerical studies indicate that one such frequency is close to $k^* = 17.54/\alpha$, which here is $k = 52.62$. Note that α is the scaling factor for the internal charge point surface, see equation (5.4).

Table 6.2 gives the reconstruction error for a range of wavenumbers k using ℓ^1 reconstruction techniques and compares the accuracy of the reconstruction using all 576 charge points, and using two different values of the sparsity parameter β. In particular, we compare the default choice used in the last section of $\beta = 0.5$ with the choice $\beta = 0.9$, which uses fewer charge points but at the potential cost of poorer accuracy. The maximum wavenumber studied corresponds to the wavelength being close to (but still greater than) the exterior measurement distance δ. The results show that both irregular and high frequencies lead to a degradation in the accuracy of the reconstruction, and lead to a loss of sparsity in the reconstructions. Accurate and reasonably sparse reconstructions can be generated provided there are at least 3 data points per wavelength since for up to $k = 44.88$ we can reconstruct the solution with a smaller error than the level of added noise (15%) and with at least an order of magnitude reduction from the total number

Table 6.2: The ℓ^2 percentage error in the reconstructed Neumann boundary data generated from a source point on the $z-$axis at $z_0 = 0.05$, with internal source surface at $\alpha = 1/3$ and 15% added noise over a range of wavenumbers k.

k	% error: full	% error: $\beta = 0.5$	$N^*(0.5)$	% error: $\beta = 0.9$	$N^*(0.9)$
1	6.428	6.429	10	12.27	6
22.44	2.369	2.369	11	4.752	9
44.88	4.358	4.358	37	6.904	25
52.62	9.458	9.462	162	4797	74
67.32	6.937	6.937	108	17.18	67
134.6	11.15	11.15	189	17.86	128
179	18.89	18.89	324	26.87	212

of charge points (576). These results are consistent with the findings of Ref. [33], where it is also suggested that a superposition method will give accurate results provided there are at least 3 degrees of freedom per wavelength. We note that if the surface of interior charge points includes the location of the monopole generating the acoustic field then one would obtain exact representations for arbitrarily high frequencies.

In addition to the general trend of increased errors for higher frequencies, one also observes a local peak in the error at the characteristic wavenumber $k = 52.62$. Here, by characteristic wavenumber we means a wavenumber corresponding to an internal resonance of the charge point surface. Also, we can see here that the error is particularly poor for the sparse reconstruction with $\beta = 0.9$, and that there is also a local peak in the number of dominant charge points. This suggests that sparse reconstructions are not feasible at higher frequencies or at irregular

frequencies. However, the reconstruction error is lower than the noise level for the schemes using all charge points or with $\beta = 0.5$ for all frequencies tested up to twice the Nyquist frequency. The results of this section therefore suggest that the method of superposition with ℓ^1 regularisation can provide excellent reconstructions for frequencies up to around twice the Nyquist frequency, and that sparse reconstructions are feasible provided we have at least three data points per wavelength. Irregular frequencies degrade both accuracy and sparsity. However, if a more accurate and sparsely reconstructed solution was required at $k = 52.62$, then we could change the scaling of the internal source surface (i.e. change α), which would move the location of the irregular frequency. Changing α from 1/3 to 0.4 leads to a percentage error of 6.131% for both the full reconstruction and the sparse scheme with $\beta = 0.5$, which identifies $N^*(0.5) = 102$ dominant charge points. For $\beta = 0.9$, the error increases to 16.00% with $N^*(0.9) = 63$. Note that these results are far more consistent with the other results shown in Table 6.2 and the removal of the local error peaks is shown more clearly in Fig. 6.3, where the square and diamond symbols show the values computed with $\alpha = 0.4$ for $\beta = 0.5$ and $\beta = 0.9$, respectively.

The results presented by Chardon *et al.* [41] using sparse plane wave reconstructions indicate that randomising the exterior data point locations (measurement locations) within the hologram plane facilitates sparse reconstructions above the Nyquist limit. Unfortunately, the reconstructed solutions using the method of superposition lose their sparsity at frequencies around and above the Nyquist limit and randomising the data point locations has been observed to degrade the accuracy of the reconstructed solution, in general, across the range of wavenumbers studied in Fig. 6.3. These observations are consistent with the findings in Ref. [65]. The main result of this section is that although in certain special cases ℓ^1 sparse regularisation could give exact representations up to arbitrarily high frequencies,

in general the reconstruction accuracy will decrease at higher frequencies. Irregular frequencies can also be treated simply by perturbing the surface of interior charge points.

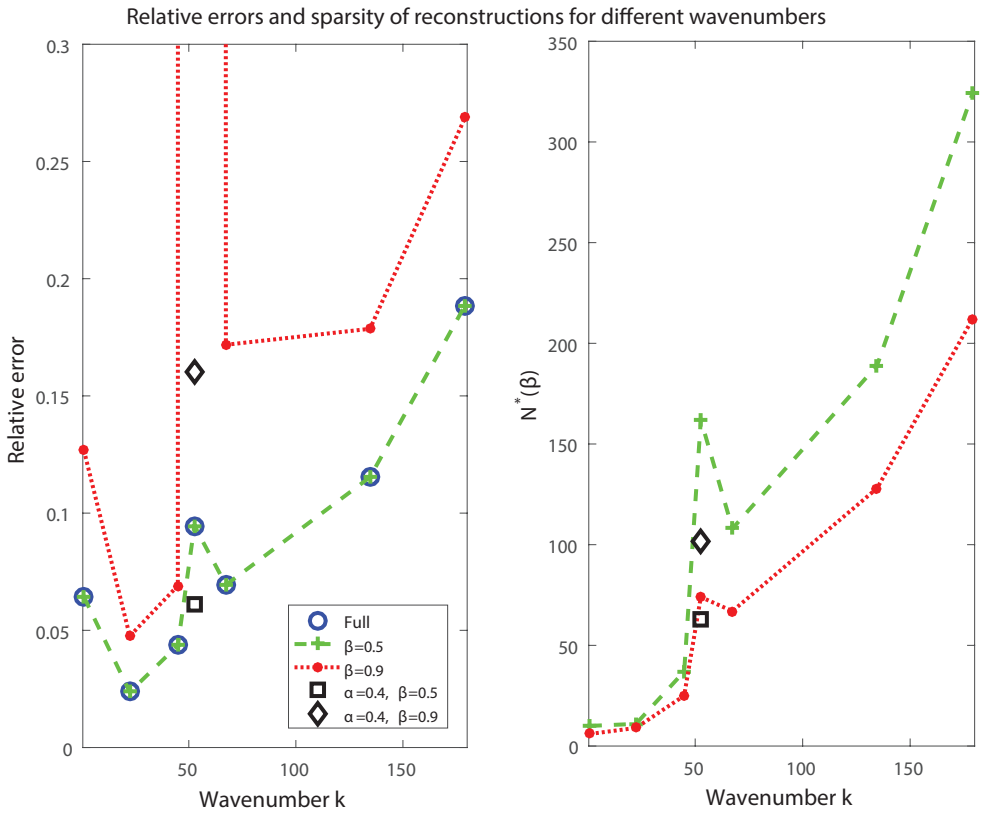

Figure 6.3: The accuracy and sparsity of the reconstructed solutions with 15% added noise, $\alpha = 1/3$ and $z_0 = 0.05$. The plots show the effect of changing the wavenumber k, including the effect of irregular frequencies and values above the Nyquist frequency. The square and diamond symbols in each plot show the results recomputed using $\alpha = 0.4$ when $k = 52.62$ for each value of β.

6.4.3 Dependence on the singularity and charge point locations

The results in the previous subsections all reconstructed the Neumann data generated from a point source located on the $z-$axis at $z_0 = 0.05$. This ensured that the singularity in the solution of the related interior problem was located within the interior charge point surface for $\alpha = 1/3$. We now consider how the accuracy and sparsity of our reconstructed solutions depends on both the position of an interior source point generating the exterior pressure data, and the relative size/position of the internal charge point surface controlled by the parameter α as described by Eq. (5.4).

Fig. 6.4 shows both the percentage errors for the sparse reconstructions and the value of the sparsity parameter $N^*(0.5)$ for different sized interior charge point surfaces and for different positions of the point source generating the exterior data. These quantities have been computed for values of α between 0.1 and 0.8, and for z_0 between $z_0 = 0$ and $z_0 = 0.15$. Instead of showing values of the parameter α, Fig. 6.4 shows the corresponding $z-$coordinate where the interior charge point surface intersects the positive $z-$axis. In this way we are able to indicate the size of the interior charge point surface relative to the location of z_0 on the same axes. Note that since Γ intersects the positive z-axis at $z = 0.21$ (it is centred at the origin with total height 0.42m), then the internal source surface with, for example, $\alpha = 0.5$ will intersect the positive z-axis at $z = 0.105$, and this is the value used along the horizontal axis in Fig. 6.4. In all cases the added noise level is 15%. Note that the relative errors obtained when reconstructing the solution using all charge points differs from that given by the sparse reconstruction by less than 1%.

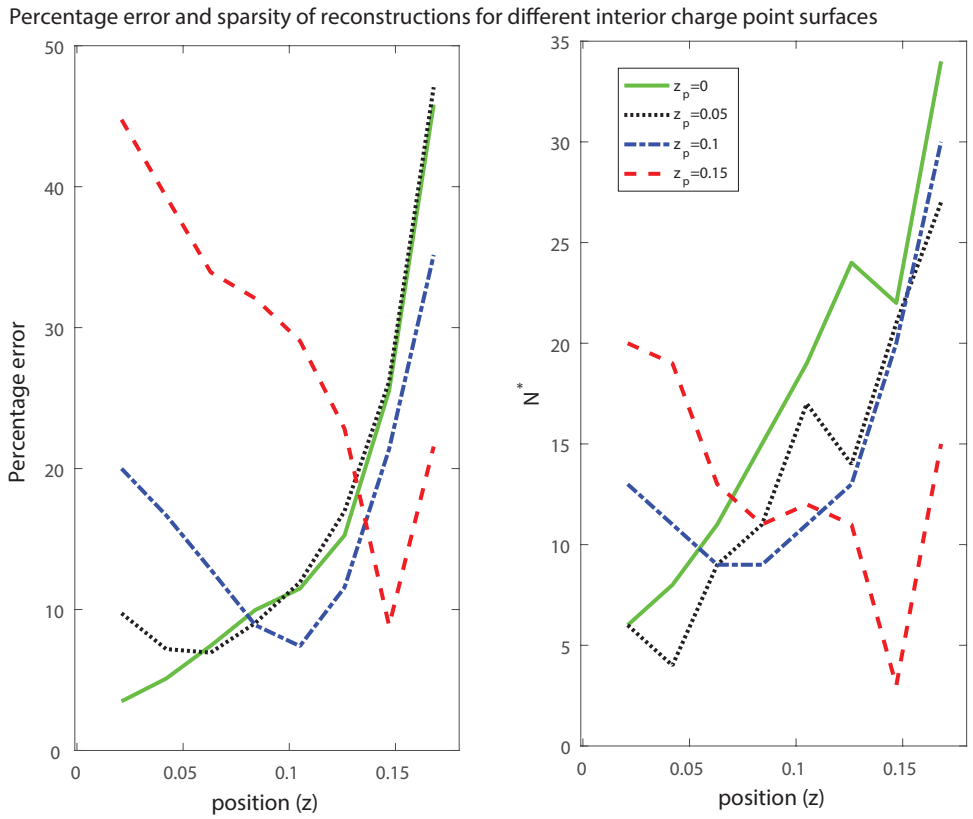

Figure 6.4: The accuracy and sparsity of the reconstructed solutions with $k = 1$ and 15% added noise. The plots show the effect of using a range of different sized interior charge point surfaces and different positions for the source point generating the boundary data.

Each subplot of Fig. 6.4 shows four curves, corresponding to each of four choices of z_0. The left subplot shows the percentage errors for different choices of the interior charge point surface. We notice that the errors are minimised when the size of the interior charge point surface is such that it intersects the positive $z-$axis close to $z = z_0$. Likewise, the right subplot shows that the number of charge points N^* needed to obtain a sparse reconstruction is also minimal when the size of the interior charge point surface is such that it intersects the positive $z-$axis close to

$z = z_0$. In general, the solutions are reasonably accurate for charge point surfaces intersecting the positive $z-$axis between $z = 0.05$ and $z = 0.1$, corresponding to choosing $\alpha = 0.3$ or $\alpha = 0.4$. Choosing $\alpha = 0.8$ so that the charge point surface intersects the positive $z-$axis at $z = 0.168$ gave the worst results in general. The results of this section suggest that it does not seem to be critical whether or not the surface of interior charge points encloses any singularities in the modelled wave field. Furthermore, the results also point to important potential applications of the sparse superposition method developed here for source identification problems in general.

6.4.4 Example of a locally radiating structure

In this section we consider the problem of reconstructing the vibrations of a structure which is rigid, except over a relatively small region. This is both a typical assumption for the application to modelling loudspeakers, and is also typical of problems commonly modelled using the method of patch NAH, whereby measurements and reconstructions only take place in the vicinity of the vibrating region (see for example Refs. [9, 28]). In the present study we use such an example for verification of the sparse superposition method for a problem where the pressure data is not generated by a monopole point source, and hence an optimal choice for the surface of internal charge points would not be related to the location of such a monopole.

We consider reconstructing Neumann boundary data given by a raised cosine function

$$\frac{\partial \phi}{\partial \mathbf{n}_x}(\mathbf{x}) = \frac{1}{2}\left(1 + \cos(10\pi|\mathbf{x} - \mathbf{x}_0|)\right), \tag{6.10}$$

inside the circle defined by $\Gamma \cap \{\mathbf{x} : 10|\mathbf{x} - \mathbf{x}_0| < 1\}$, with $\mathbf{x}_0 = (0.14, 0, -0.0525)$. Outside of this circle we let the Neumann boundary data be zero. The exterior pressure data at a distance $\delta = 0.035$m from Γ are generated using the BEM

as described in Chapter 2. The triangulation has been refined compared to the results in previous sections and now has 1024 triangles / interior charge points and 1024 exterior data points. This has been done to improve the resolution of both the boundary data representation and the BEM approximation of the exterior pressure data. Note that here there is an extra source of noise (in addition to the 15% added noise) in the acoustic pressure data due to the numerical error in the BEM approximation. The results of the sparse reconstruction technique for wavenumber $k = 1$ are shown in Fig. 6.5. We found that a value of α between 0.3 and 0.4 gave the best results, which is consistent with the previous section, and hence we have taken $\alpha = 1/3$.

The upper subplots of Fig. 6.5 show that the sparse superposition method produces a good reconstruction of the vibrating region for the prescribed locally vibrating boundary data. The computations shown use $\beta = 0.5$ to generate the sparse scheme leading to $N^* = 30$ dominant charge points (of 1024 in total). The percentage error in the sparse reconstruction is 21.19%, which is the same (up to the quoted level of accuracy) as the error using all 1024 charge points for the reconstruction. We note that the boundary data to be reconstructed has 52 out of 1024 entries that are non-zero. Relatively significant errors arise in the rigid regions of the locally vibrating object (we consider the entire surface Γ to have unknown Neumann boundary data), close to the edges of the cuboid that are nearest the vibrating region. If we instead assume prior knowledge of the non-vibrating regions and consider only the accuracy of the reconstruction over the vibrating region, then the error reduces to 9.843% for both the sparse and full data reconstructions. A plot of this post-processed result is shown in the lower left subplot of Fig. 6.5.

The lower right subplot of Fig. 6.5 shows the result of reconstructing the Neumann boundary data starting only with the 30 dominant source points identified by the sparse reconstruction method and using a reduced data set sampled from

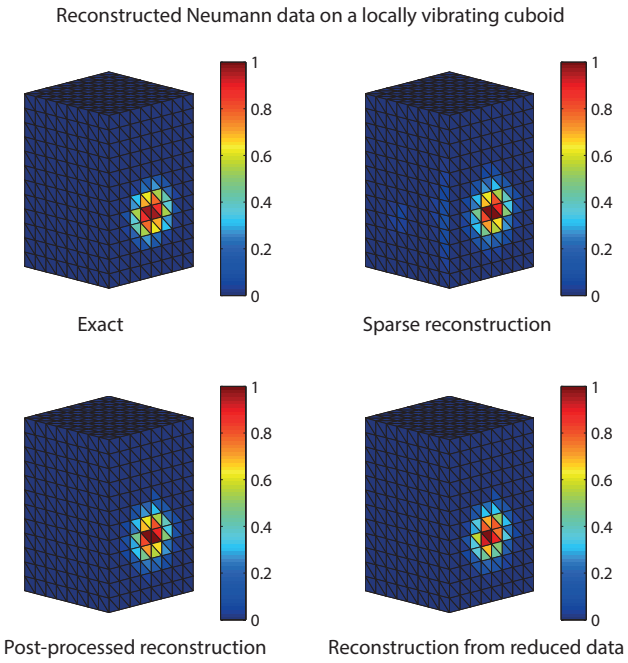

Figure 6.5: The Neumann boundary data for a locally radiating structure with 1024 charge points, 1024 data points, $k = 1$ and $\alpha = 1/3$. Comparison of the exact solution (upper left) with the sparsely reconstructed boundary data (upper right), the sparsely reconstructed boundary data after post-processing (lower left) and a reconstruction using only 28 charge points and a reduced data set with 800 values (lower right).

the full data set at 800 randomly selected points. The same post-processing procedure as described above has been applied to fix the solution in the non-vibrating regions to zero. The results shown are computed using Tikhonov regularisation (with only the 30 charge points identified by the initial sparse reconstruction), which gave slightly better accuracy than using the sparse reconstruction algorithm for a second time. The percentage error in the plotted reconstruction is 18.89%, compared with 26.36% for the reconstruction without post-processing. Using the sparse algorithm to reconstruct the solution instead gave errors around 3% higher

in each case. Note that these results all show an improvement on the reconstruction obtained from the same reduced acoustic data set, but using a basis with all 1024 charge points. In this case the percentage error was more than doubled to 58.87%, and improved to 46.52% after post-processing. We remark that the reconstruction using the full basis with reduced data is an under-determined problem (the acoustic data are fewer than the number of unknowns), whereas the reconstruction from the sparse basis is over-determined. This suggests that reducing the number of charge points and changing the under-determined problem into an over-determined one is an important step for the efficient implementation of NAH with reduced data using the method of superposition.

The main result of this section is that sparse reconstruction methods can still be applied when a suitable choice of dictionary of basis functions for the sparse reconstruction is not obvious, provided there is some inherent sparsity that can be exploited. Sparse reconstructions can also be used in conjunction with reduced acoustic field data sets, giving reasonable results. In particular, the sparse basis representation leads to better accuracy and more efficient calculations than using the full basis with the reduced data set.

6.5 Summary

In this chapter the ideas behind compressive sampling have been introduced, along with the concepts of the sparsity and incoherence. Then, a sparse regularisation procedure using ℓ^1 optimization techniques has been combined with the method of superposition and applied to solve three dimensional NAH problems. The developed sparse superposition method is able to reconstruct the normal velocity of a vibrating object using only a very small number of charge points in many cases, in contrast with a standard Tikhonov reconstruction. In particular,

it appears that competitive sparse reconstructions can be generated provided the wavenumber is not too large and that the data can be assumed to be sufficiently noisy to permit a data fidelity parameter of at least 5% of the size of the ℓ^2 norm of the exterior pressure data. Sparsity also appears to be an important factor when considering reduced acoustic field data sets, where reconstructions using a sparse basis gave a considerable improvement in accuracy over using the full basis with all charge points.

Chapter 7

Experimental verification for a loudspeaker

7.1 Introduction

In this chapter, the validity of the sparse inverse method of superposition for NAH will be verified by using measured pressure data for a loudspeaker in a semi-anechoic chamber. In Section 7.2 we give the details of the experimental set up and the use of a laser vibrometer to measure the normal velocity on the surface of the loudspeaker. Next, in Section 7.3 the method of superposition for NAH in an infinite half-space is detailed. Numerical results for a sparse reconstruction approach computed with synthetic acoustic pressure data from a cuboid of similar dimensions to a typical loudspeaker have then been described in Section 7.4. After that, in Section 7.5 the numerical results for the loudspeaker are presented and the reconstructed surface velocity is compared with the measurements from the laser vibrometer. Finally, in Section 7.6 a summary of possible sources of error is given for both the measurements and the mathematical modelling.

7.2 Experimental set up

In order to verify the inverse method of superposition for near field acoustic holography, experiments to measure the acoustic radiation from a cuboid shaped speaker with similar dimensions to the cuboid described in Chapters 2 and 4 were undertaken. In particular, a loudspeaker with a cabinet of size $0.51\text{m} \times 0.32\text{m} \times 0.305\text{m}$ and a cone of radius 9.5cm has been used. To prevent the sound reflecting back from the walls and the ceiling, experiments have been performed in a semi-anechoic chamber at the Acoustics Research Centre in the University of Salford. The walls and ceiling of the semi-anechoic chamber are covered in absorbent foam and the sound reflections only come from the rigid floor. This makes the room behave approximately as an infinite half-space. In order to implement a MoS model for this type of space we will need to apply the method of images and modify the Green's function as described in the next section.

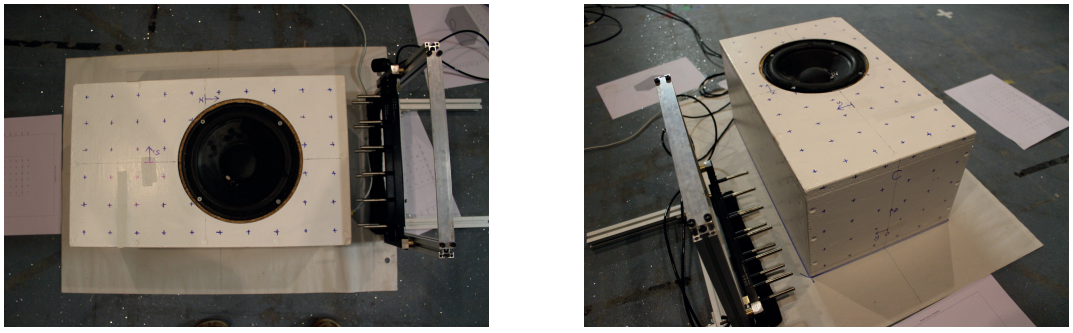

Figure 7.1: The loudspeaker positioned on its back with the cone facing upwards, and the microphones positioned close by.

For all experiments described in this section, the loudspeaker has been positioned on its back with the cone facing upwards as shown in Figure 7.1. The acoustic pressure data were measured via a series of microphones placed in arrays adjacent to the loudspeaker in a matrix form. The top plane was arranged in 10

columns and 6 rows, as shown in Figure 7.1. Faces A and C have been arranged into a matrix with 6 columns and 5 rows, while the faces B and D have been arranged into 10 columns and 5 rows, as shown in Figure 7.2. The pressure measurements have been taken near to each face at a distance of approximately 2cm and always within one wavelength from the surface of the speaker. The array has 12 microphones, as illustrated in Figure 7.2, so the total set of results have been assembled by repeating the measurements many times with the microphones at different locations to cover the entire speaker.

The microphones have been fixed on two types of stands. The first stand consists of bolt holes arranged in an array separated by 328mm horizontally and 82mm vertically for the position adjustments, and a microphone array looking sideways as shown in the left plot of Figure 7.3. The second stand consists of two columns holding the microphone array facing downwards with a fixed height of 325 mm from the ground, as shown in the right plot of Figure 7.3. For both cases, the microphone spacing is fixed at 5cm, which gives a square grid with $k_{\mathrm{nyq}} = 62.8$ for the Nyquist wavenumber, and a corresponding Nyquist frequency of approximately 3.4kHz.

In order to verify the accuracy of the reconstructions from the measured acoustic pressure data, a laser vibrometer was used to measure the normal velocity of the surface of the loudspeaker. The experiments were carried out by placing the loudspeaker on its back as before and the laser vibrometer facing downwards perpendicular to the loudspeaker as depicted in Figure 7.4. The laser vibrometer was directed to points on a rectangular grid on the loudspeaker, where it measures the normal velocity.

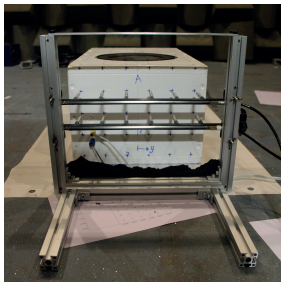

(a) Face A: the measurement points arranged into 6×5 matrix with the array of 12 microphones.

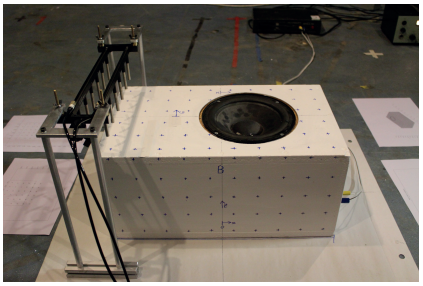

(b) Face B: the measurement points arranged into 10×6 matrix with the array of 12 microphones.

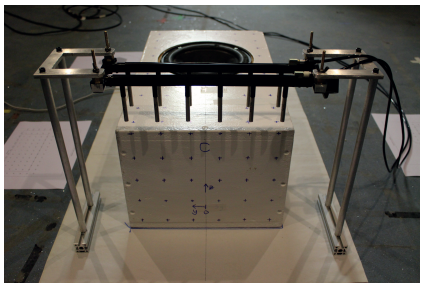

(c) Face C: the measurement points arranged into 6×5 matrix with the array of 12 microphones.

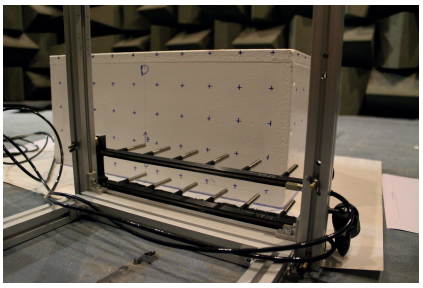

(d) Face D: the measurement points arranged into 10×6 matrix with the array of 12 microphones.

Figure 7.2: The loudspeaker faces with the distribution of the measurement points and the microphones positioned close to each face.

7.3 Method of superposition for NAH in a semi-anechoic chamber

The work reported in this section is adapted from our conference paper [66]. Consider a three-dimensional half-space of the form $H = \{\mathbf{x} \in \mathbb{R}^3 : x_3 > 0\}$, where $\mathbf{x} = (x_1, x_2, x_3)$ and let $\Omega_- \subset H$ be a finite domain with boundary surface $\Gamma \subset \bar{H}$.

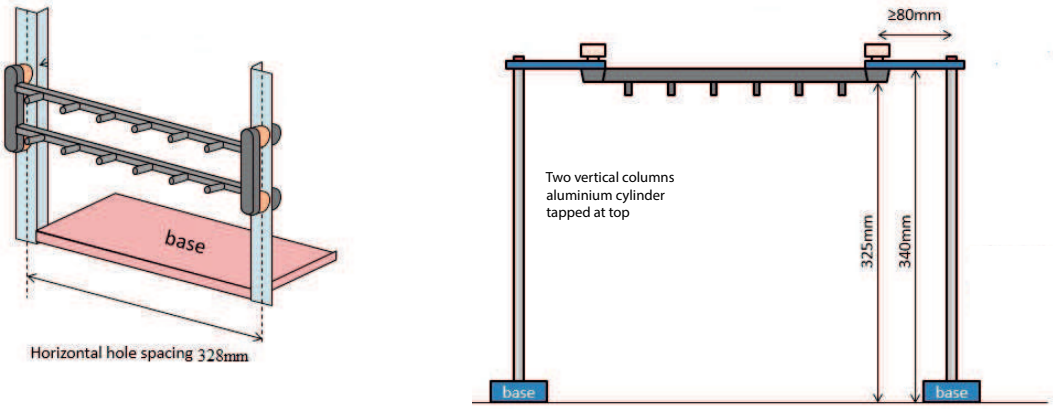

Figure 7.3: Stand 1 (left) with the microphone array looking sideways and stand 2 (right) with the microphone array looking downwards.

One can think of H as the space represented by a semi-anechoic chamber with a rigid floor and fully absorbing walls and ceiling that behaves approximately as an infinite half-space. The object Ω_- represents an acoustically radiating object placed in H, such as the loudspeaker under consideration here. We decompose Γ into two parts, $\Gamma_H \subset H$ and $\Gamma_0 = \Gamma \cap \{\mathbf{x} \in \mathbb{R}^3 : x_3 = 0\}$ so that $\Gamma = \Gamma_0 \cup \Gamma_H$ and $\Gamma_0 \cap \Gamma_H = \emptyset$. In a practical setting, Γ_0 corresponds to the part of the acoustically radiating object that is in contact with the floor of the semi-anechoic chamber.

The superposition method approximates the acoustic pressure ϕ at some point $\mathbf{x} \in H \setminus \bar{\Omega}_-$ using a basis expansion of the form

$$\phi(\mathbf{x}) \approx \sum_{j=1}^{n} \phi_j G_H(\mathbf{x}, \mathbf{y}_j), \tag{7.1}$$

where G_H is the Green's function for the Helmholtz equation in the half-space H, which is given by the method of images as

$$G_H(\mathbf{x}, \mathbf{y}) = \frac{e^{ik|\mathbf{x}-\mathbf{y}|}}{4\pi|\mathbf{x}-\mathbf{y}|} + \frac{e^{ik|\mathbf{x}'-\mathbf{y}|}}{4\pi|\mathbf{x}'-\mathbf{y}|}. \tag{7.2}$$

Figure 7.4: Laser vibrometer facing downwards towards to the loudspeaker below.

Here $\mathbf{x}^{'} = (x_1, x_2, -x_3)$ corresponds to the reflection of the point $\mathbf{x} = (x_1, x_2, x_3)$ in the plane $\partial H = \{\mathbf{x} \in \mathbb{R}^3 : x_3 = 0\}$. The points $\mathbf{y}_j \in \Omega_-$, $j = 1, ..., n$ are the charge point locations and ϕ_j are the corresponding coefficients, which are determined by application of the method. Note that the half-space Green's function G_H corresponds to the Neumann Green's function with

$$\frac{\partial G_H}{\partial x_3}(\mathbf{x}, \mathbf{y}) = 0 \tag{7.3}$$

whenever $\mathbf{x} \in \partial H$. We can show this directly by differentiating (7.2) to give

$$\frac{\partial G_H}{\partial x_3}(\mathbf{x},\mathbf{y}) = \frac{(y_3-x_3)e^{ik|\mathbf{x}-\mathbf{y}|}(1-ik|\mathbf{x}-\mathbf{y}|)}{4\pi|\mathbf{x}-\mathbf{y}|^3} - \frac{(y_3+x_3)e^{ik|\mathbf{x}'-\mathbf{y}|}(1-ik|\mathbf{x}'-\mathbf{y}|)}{4\pi|\mathbf{x}'-\mathbf{y}|^3}. \tag{7.4}$$

For $\mathbf{x} \in \partial H$, then $x_3 = 0$ and the two terms in equation (7.4) cancel. Hence, the Green's function G_H satisfies the rigid floor boundary condition (7.3). As before, the coefficients ϕ_j are chosen so that the ℓ^2 norm of the residual vector $\mathbf{r}$, with entries given by

$$r_i = \phi(\mathbf{x}_i) - \sum_{j=1}^{n} \phi_j G_H(\mathbf{x}_i, \mathbf{y}_j) \tag{7.5}$$

for $i = 1, .., n$, is smaller than a desired error tolerance. Once the coefficients ϕ_j have been obtained, then the Neumann boundary data can be recovered from

$$\frac{\partial \phi}{\partial \hat{\mathbf{n}}}(\mathbf{x}) \approx \sum_{j=1}^{n} \phi_j \frac{\partial G_H}{\partial \hat{\mathbf{n}}}(\mathbf{x}, \mathbf{y}_j). \tag{7.6}$$

We will apply the sparse regularisation approach described in Chapter 6 to minimise $\|\boldsymbol{\phi}\|_1$, the ℓ^1 norm of $\boldsymbol{\phi} = [\phi_1, \phi_2, ..., \phi_n]^T$, for a fixed acceptable discrepancy level $\|\mathbf{r}\|_2^2 \leq \epsilon$. The possibility of a sparse reconstruction is highly dependent on the basis functions used to represent the solution. In the modified superposition method here, these basis functions are the half-space Green's functions for the Helmholtz equation at a set of distinct interior charge points. In the next section we will investigate whether this choice of basis functions can yield a sparse reconstruction for synthetic pressure data generated by an interior point source.

7.4 Numerical results for a cuboid with synthetic pressure data

Before applying the inverse MoS to the experimental data obtained as described in Section 7.2, we first test our reformulated MoS for infinite half-space using

synthetic pressure data, as in Chapter 6. The numerical results reported here are taken from our paper [66] and are computed for acoustic radiation from a cuboid of similar dimensions to a typical loudspeaker cabinet ($0.28\text{m} \times 0.28\text{m} \times 0.42\text{m}$). The base of the cuboid Γ_0 lies in the plane $x_3 = 0$. We will use a triangulation of Γ_H to generate the points at which the pressure data are computed, as well as the internal charge points and the points at which we reconstruct the solution on Γ_H. In particular, for a given triangulation of Γ_H we reconstruct the Neumann boundary data at the centroid of each triangle and project (from each centroid) a distance δ along the normal vector to Γ into Ω_+ to obtain the points where the exterior pressure data are recorded. The internal charge points are positioned inside Ω_-, on a scaled down version of Γ_H with scaling factor $\alpha \in (0, 1)$, as described in Chapters 5 and 6.

We will reconstruct the boundary data generated by a point source at $\mathbf{x}_0 \in \Omega_-$. The pressure data is then constructed using the half-space Green's function as follows:

$$(\boldsymbol{\phi}_0)_j = a\left(\frac{e^{ik|\mathbf{x}_j - \mathbf{x}_0|}}{|\mathbf{x}_j - \mathbf{x}_0|} + \frac{e^{ik|\mathbf{x}'_j - \mathbf{x}_0|}}{|\mathbf{x}'_j - \mathbf{x}_0|}\right), \qquad j = 1, ..., n. \tag{7.7}$$

Here, $a \in \mathbb{C}$ is the strength of the source, which in these examples is arbitrarily taken to be $a = 3 - i$. The boundary data generated at $\mathbf{y} \in \Gamma_H$ may also be obtained for the case of a point source at $\mathbf{x}_0$ by replacing $\mathbf{x}_j$ in (7.7) by $\mathbf{y} \in \Gamma_H$, differentiating in the direction of $\hat{\mathbf{n}}_y$ and evaluating at the centroids of the triangulation $\mathbf{y} = \mathbf{y}_j$ for $j = 1, ..., n$ to give

$$\begin{aligned}\frac{(\mathbf{v})_j}{a} = &\frac{\hat{\mathbf{n}}_{y_j} \cdot (\mathbf{x}_0 - \mathbf{y}_j)}{|\mathbf{y}_j - \mathbf{x}_0|^3}(1 - ik|\mathbf{y}_j - \mathbf{x}_0|)e^{ik|\mathbf{y}_j - \mathbf{x}_0|} \\ &+ \frac{\hat{\mathbf{n}}_{y_j} \cdot (\mathbf{x}'_0 - \mathbf{y}_j)}{|\mathbf{y}'_j - \mathbf{x}_0|^3}(1 - ik|\mathbf{y}'_j - \mathbf{x}_0|)e^{ik|\mathbf{y}'_j - \mathbf{x}_0|}.\end{aligned}$$

Using this calculation it is possible to verify the accuracy of the regularised approximate solutions with different wavenumbers and point source positions $\mathbf{x}_0 \in \Omega$. Uniformly distributed and additive white noise will be applied to $\boldsymbol{\phi}_0$ in order to

more closely replicate experimental observations. We compute the level of added noise w as described previously in equation (6.7).

For these experiments the number of charge points, the number of measurement points and the number of points at which we reconstruct the solution are all equal to 504. This is achieved by triangulating the internal source surface in an identical way to Γ_H and taking the charge points at the triangle centroids. The data fidelity parameter ϵ appearing in equation (6.3) is chosen as

$$\epsilon = (\max\{\epsilon_{\min}, w\})^2 \|\boldsymbol{\phi}_0\|_2^2, \tag{7.8}$$

where w is the level of noise added to the pressure data as before. The results in this section have been obtained with $\epsilon_{\min} = 1\text{E-}6$.

Consider the case $k = 1$ and $\mathbf{x}_0 = (0, 0, 0.1)$, where the frequency is relatively low, is not close to an irregular frequency and $\mathbf{x}_0$ is relatively close to the origin and will lie inside the surface on which the interior charge points are located. Under such conditions the superposition method is expected to work well as noted in Chapter 5. The pressure data are specified at a distance $\delta = 0.035$m from Γ_H and the internal source surface is scaled down to have dimensions $\alpha = 1/3$ the size of Γ. We note that these choices should lead to good results as discussed in Section 6.4.1.

Figure 7.5 shows the sparse reconstruction of the Neumann data with noise level $w = 5\%$. The exact solution is also shown for reference and appears almost identical to the sparse reconstruction. The right sub-plot shows the charge point strengths ϕ_j, $j = 1, \ldots, 504$ given by the sparse reconstruction algorithm. Note that many of the ϕ_j, $j = 1, \ldots, 504$ are suppressed and are close to $\mathcal{O}(10^{-6})$, but 13 dominant terms can be picked out which are close to $\mathcal{O}(10^{-1})$. The sparse reconstruction shown in the left sub-plot was created using only these 13 values. We note that the half-space sparse superposition approach is performing similarly to the free-space method reported in Chapter 6. In particular, parallels can be

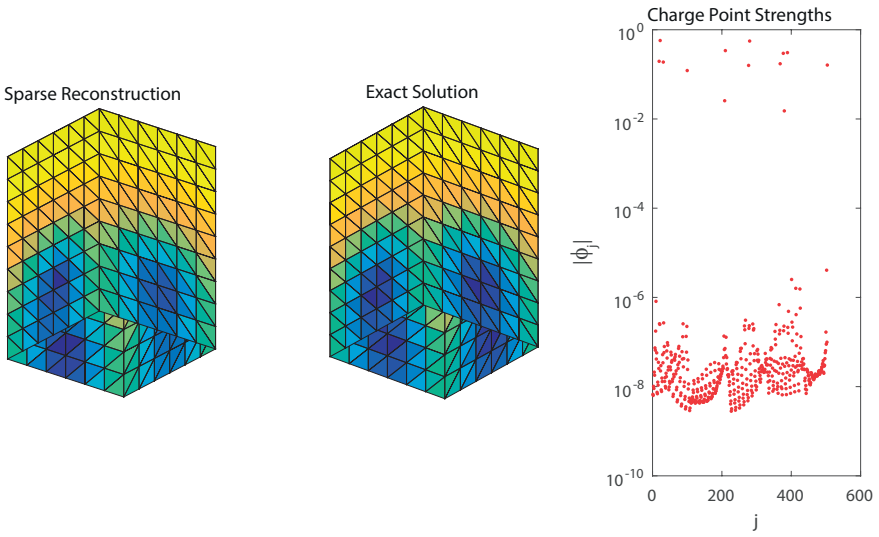

Figure 7.5: Neumann boundary data on a cuboid generated by a point source at $\mathbf{x}_0 = (0, 0, 0.1)$ with wavenumber $k = 1$ and $w = 5\%$ added noise. The plots compare the exact solution against the ℓ^1 reconstruction approach using only the $N^* = 13$ dominant charge points of largest magnitude shown in the right sub-plot.

drawn between Figs. 6.1, 6.2 and 7.5. We are therefore confident that the method is working as expected for the half-space reformulation and in the next section we proceed to apply it to the experimental data described in Sect. 7.2.

7.5 Numerical results for a loudspeaker with measured pressure data

An experimental study was conducted to apply the inverse MoS model for near-field acoustic holography with the acoustic pressure data obtained at the University

of Salford, in order to reconstruct the normal velocity on the surface of a loudspeaker. The loudspeaker geometry with the dimensions described in Section 7.2 was implemented and the corresponding mesh is shown in Figure 7.6. The internal charge points $\mathbf{y}_j$ with $j = 1, 2, ..., 288$ have been generated by taking the location of the measurement points surrounding the loudspeaker and multiplying them by a factor of 0.5. This leads to a set of charge points positioned on the upper five faces of a cuboid in the interior of the loudspeaker, and is analogous to the set up used in Section 7.4. Note therefore that the measurement points and the charge points are not conformal to the geometry of the loudspeaker. This is due to the difficulty involved in placing the microphones at a fixed distance from the cone.

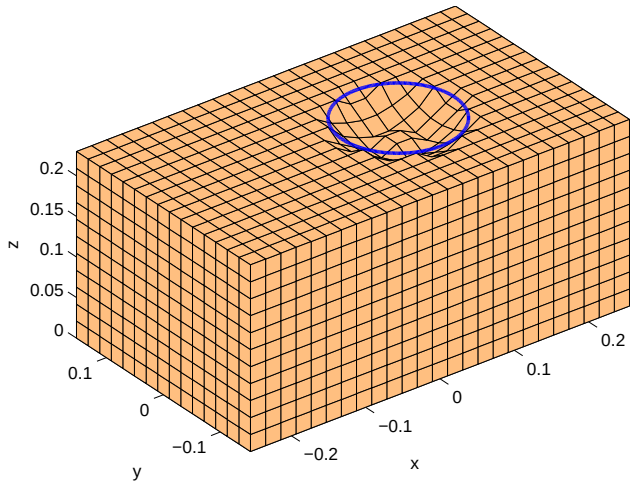

Figure 7.6: The loudspeaker geometry employed for the computational model.

To investigate the performance of the method of superposition for this inverse NAH problem, we test the model using a frequency range from 100 to 6800 Hz. The lower limit is taken as a result of the measured data being unreliable due to measurement noise below 100 Hz. The upper limit is at approximately twice the Nyquist frequency, and corresponds to a wavelength of approximately 5cm,

meaning that the measurement distance of 2cm always lies within one wavelength of the radiated acoustic wave. The results obtained utilizing the sparse reconstruction method are compared to the measured data from the laser vibrometer. The data fidelity parameter ϵ is chosen similarly to in equation (7.8), but the mean coherence of the measured data (given by the NAH experiments) is used in place of the added noise level w. The coherence value is calculated directly by the NAH measurement software and estimates the extent to which the measured data may be predicted using a least squares approximation. A coherence value close to 1 indicates ill-conditioned data and requires a much larger value of ϵ than when the coherence is significantly smaller than 1. The typical values of ϵ used in these experiments range from 50% of the ℓ^2 norm of the measured pressure data for low frequencies where the coherence is close to 1, down to around 7% of the ℓ^2 norm of the pressure data at higher frequencies where the coherence is lower.

Figure 7.7 demonstrates the comparison between the sparse reconstructed and the measured values for four approximately equally spaced frequencies between 100 Hz and 2550 Hz. These frequencies are all below the Nyquist frequency and the reconstructions show reasonably good correspondence to the normal velocities measured using the laser vibrometer, particularly for the higher frequency cases. We note that for frequencies below the Nyquist limit, traditional Tikhonov regularization with GCV should also work reasonably well. Figure 7.8 shows the results of using Tikhonov regularisation for the same set of experiments. We note that the sparse reconstructions are significantly more accurate and use only a fraction of the number of degrees of freedom in the numerical method; the plots in Figure 7.7 use between 19 (100 Hz) and 167 (2550 Hz) internal charge points from a total of 288. Clearly, the Tikhonov regularisation process has failed and the ill-conditioned nature of the problem has led to the results in Figure 7.8 being meaningless.

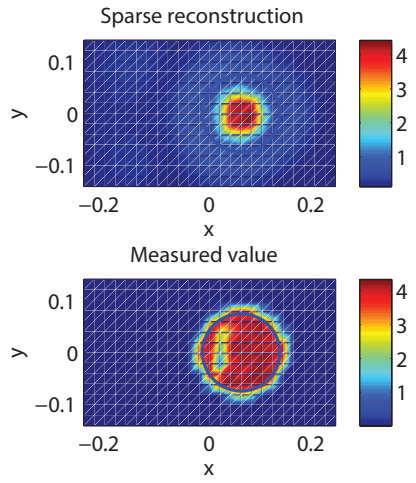

(a) $f = 100$ Hz

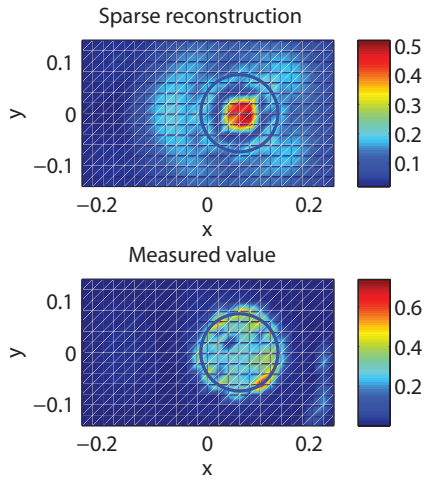

(b) $f = 900$ Hz

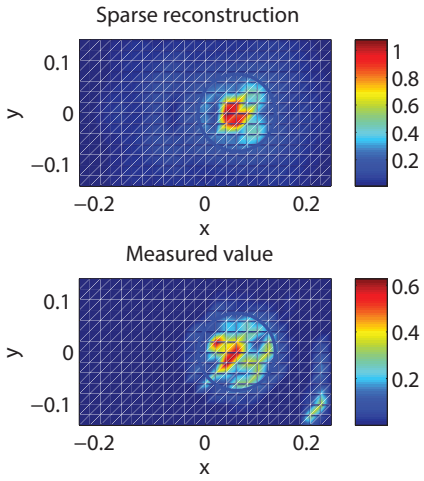

(c) $f = 1700$ Hz

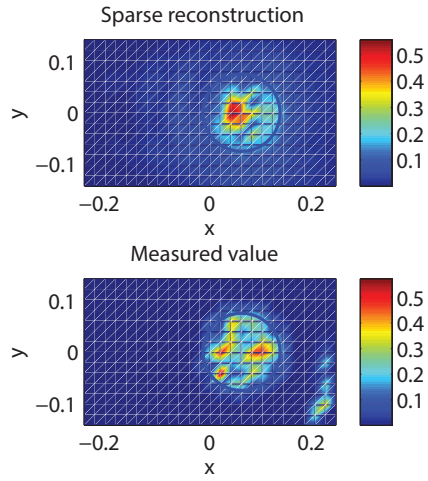

(d) $f = 2550$ Hz

Figure 7.7: The reconstructed results for the normal velocity using sparse regularisation compared to the measured data at different frequencies f below the Nyquist frequency.

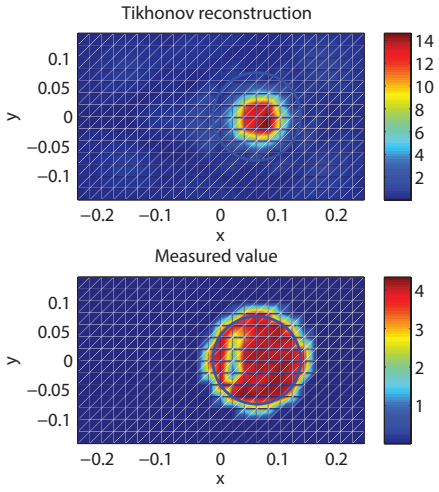

(a) $f = 100$ Hz

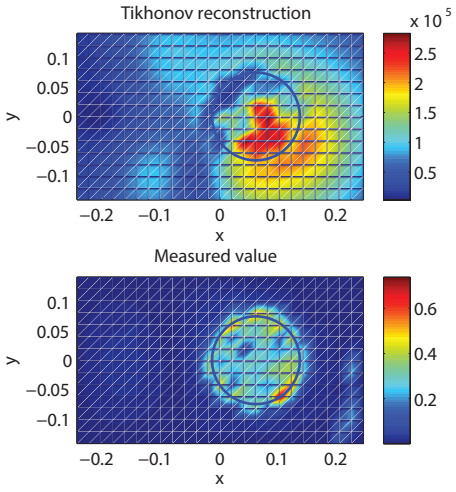

(b) $f = 900$ Hz

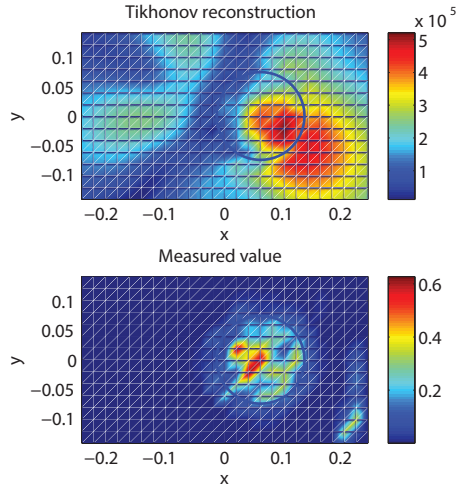

(c) $f = 1700$ Hz

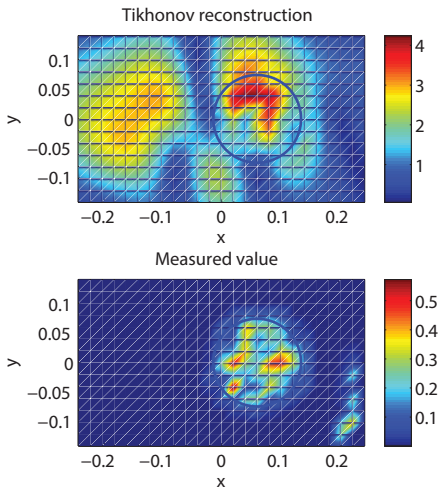

(d) $f = 2550$ Hz

Figure 7.8: The reconstructed results for the normal velocity using Tikhonov regularization compared to the measured data at different frequencies f below the Nyquist frequency.

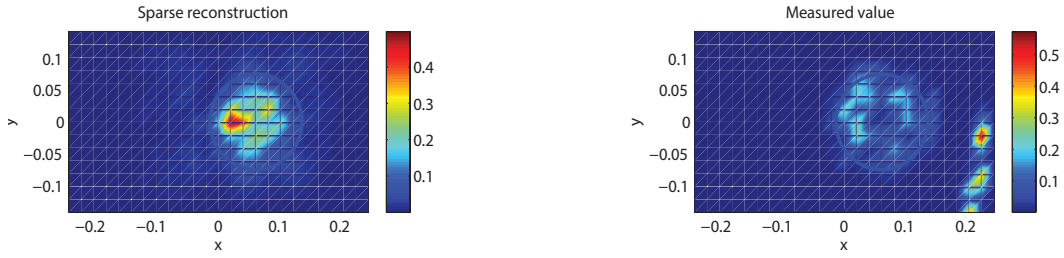

(a) $f = 3400$ Hz

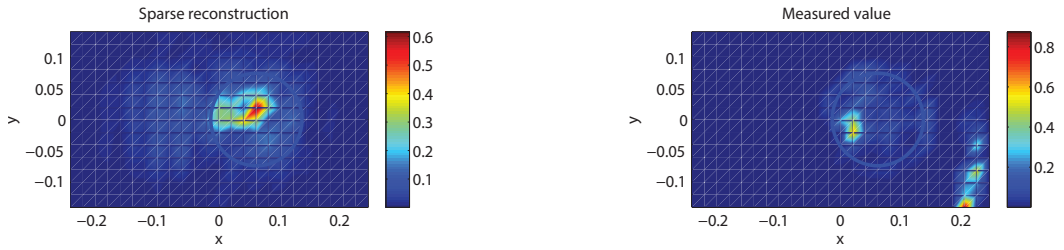

(b) $f = 4250$ Hz

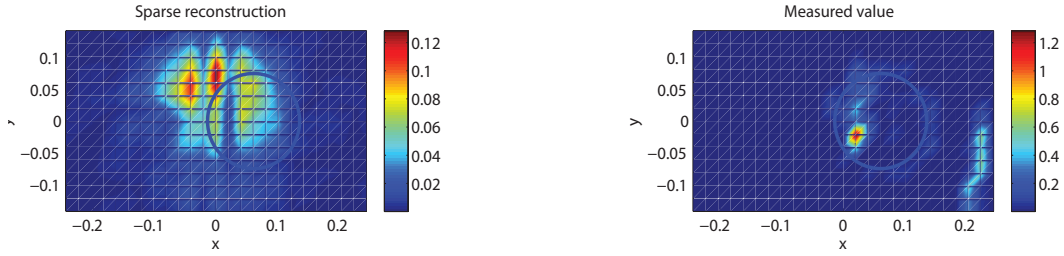

(c) $f = 6800$ Hz

Figure 7.9: The reconstructed results for the normal velocity using sparse regularisation compared to the measured data at different frequencies f around and above the Nyquist frequency.

Figure 7.9 shows the results of using the sparse reconstruction method for frequencies around and exceeding the Nyquist frequency (3400 Hz) up to a maximum of 6800 Hz. Whilst the reconstructed velocity at the Nyquist frequency is reasonably accurate, the more the frequency is increased above this level, the poorer the reconstructions become. From the results obtained previously in this section, we conclude that the sparse superposition method has good accuracy at frequencies up to and including the Nyquist rate. Beyond the Nyquist rate, the data sampling is not sufficient to produce an accurate reconstruction.

7.6 Sources of error

There are a number of factors that could influence the accuracy of the results presented in the previous sections and may account for some of the differences observed between the computational results and the measurements. In this chapter, all the numerical approximations will contain some degree of error as a result of both interpolating the solution over a discrete mesh and representing the measured pressure as a finite sum of Green's functions. Some possible additional sources of error for the case of loudspeaker modelling include:

Mesh geometry: The numerical model used for the loudspeaker geometry was generated using measurements when the loudspeaker was switched off. When the loudspeaker is switched on and operated, the cone raises up slightly due to switching on the magnetic field and then vibrates to radiate sound. Therefore the geometric data used in the model is only approximate and hence is subject to error.

Measurement noise: Even though the measurement of the sound pressure was per-

formed in a semi-anechoic chamber, there is still some reflected and exterior noise that could affect the accuracy of the measurement.

Inaccuracy of the measurement position: The position of the microphone utilized for the pressure measurements can only be given to within a few millimetres and consequently the exact points at which the measurements are taken are unknown.

Speed of sound: The speed of sound is very sensitive to the temperature. Thus, during the measurement, the temperature could be vary and hence the speed of sound may be different to the value of $c = 346\text{ms}^{-1}$ used in the simulations here.

7.7 Summary

In this chapter we described the experimental procedure for sampling the acoustic pressure in the near-field and the use of the laser vibrometer to measure the normal velocity on the surface of the loudspeaker. The method of superposition was then reformulated for NAH in an infinite half-space, in order to apply a mathematical model that more closely represents the experimental set up. The numerical results for the sparse regularisation approach were then computed for synthetic acoustic pressure data to test the reformulated model before applying it to the measured data. Next, the model was verified at different frequencies between 100 Hz and 2550 Hz. The results of the sparse regularisation procedure compared favourably with the values measured using the laser vibrometer. We also found that the sparse regularisation procedure considerably out-performed a standard Tikhonov based approach for these experiments. We then tested the sparse regularisation procedure for higher frequencies around and above the Nyquist frequency. Both the accuracy of the reconstruction and the level of sparsity were

degraded as the frequency was increased. The results obtained in the above experiments illustrated that the sparse inverse method of superposition has reasonably good accuracy for frequencies up to and including the Nyquist rate, and that the accuracy decreases above the Nyquist frequency. Finally, a summary of possible sources of error was given in order to explain the relative lack of precision in the results here, compared with those for the simpler test problems studied earlier in the thesis.

Chapter 8

Conclusions and further work

The work presented in this thesis aimed at developing a novel method for modelling near-field acoustic holography, where the acoustic field on the surface of a vibrating structure was recovered from measurements taken in the exterior field. To achieve this target, existing numerical techniques for NAH were surveyed and the study included Fourier acoustics based NAH, the inverse BEM and the inverse MoS. All these methods have been implemented, compared and discussed. The Fourier acoustics based NAH was used to solve the inverse problem of NAH on a flat plate, given acoustic pressure data in the near-field above the plate. The results showed that this method is simple to use and that fast, accurate numerical schemes can be applied using the fast Fourier transform. However, this method is limited to separable geometries such as spheres, cylinders and flat plates. The inverse boundary element method (IBEM) for near-field acoustic holography was applied to general three-dimensional geometries. The calculation was relatively slow and complicated, particularly if characteristic frequencies are to be properly treated. Next, the inverse method of superposition for NAH problems was formulated and applied to two geometrically different test problems (cuboid and sphere). The results demonstrated that the MoS for the inverse problem of NAH was simple

to implement, more accurate than the IBEM and had faster computational times. However, it is difficult to know (without heavy use of trial and error) what are the optimal internal charge point locations.

A sparse superposition method was developed and implemented for the inverse MoS. The method is able to reconstruct the normal velocity of a vibrating object using a very small number of charge points. Two primary reasons this is beneficial are firstly, one can potentially reduce the amount of measured data required, and secondly, we can also detect sources of noise when a small number of clustered charge points are identified. The sparse inverse MoS was then successfully applied to reconstruct the surface velocity of a loudspeaker from measurements of the sound pressure field taken in a semi-anechoic chamber. The development of the new sparse inverse MoS and its experimental verification form the primary contribution to knowledge of this thesis.

8.1 Conclusions

In Chapter 1 we described the background to this research, and gave a review of the literature related to numerical techniques for NAH. The general concept of interior and exterior problems was considered. Numerical techniques for NAH problems such as Fourier acoustics based NAH, and the inverse boundary element method were discussed. Then, a number of alternative methods to the IBEM that have been suggested for the numerical solution of NAH problems were also discussed. Finally, some regularisation procedures have been surveyed, such as the truncated singular value decomposition (SVD), Tikhonov regularization and sparse reconstruction methods.

The boundary element method for the solution of the Helmholtz equation in an unbounded exterior domain was presented in Chapter 2, and the surface Helmholtz

equation for the exterior acoustic problem of the Helmholtz equation was derived. Then, the application of the BEM for the forward Neumann problem has been described. The corresponding inverse problem is the NAH problem to determine the Neumann boundary condition given a set of pressure data in the exterior domain. Accurate numerical results were obtained for examples on a cuboid and a sphere.

The Fourier acoustics method for solving the inverse problem of NAH was introduced in Chapter 3, where the vibrational behaviour of a flat plate was reconstructed from acoustic pressure data in the near-field. The integral equation formulation for modelling acoustic radiation from an infinite plate using a modified Green's function given by the method of images was detailed. Fourier transforms and the convolution theorem were then applied to solve this problem for either the pressure or the Neumann data on the flat plate. The results of using the Fourier acoustics solution were compared against an exact solution for an infinite flat plate, and the effect of changing both the location of the prescribed pressure data, and the wavenumber have been investigated.

Chapter 4 gave a reformulation of the boundary integral equation for the Helmholtz equation given in Chapter 2, to solve the inverse problem of NAH. This inverse problem is ill-posed because the solution of the Neumann boundary data does not depend continuously on the given data. In order to overcome this problem, Tikhonov regularization was applied, and it was shown that subject to a suitable choice of the regularisation parameter λ, reasonably accurate reconstructions could be obtained. The behaviour of the method was investigated, given noisy acoustic pressure data in the exterior domain and two geometrically different test problems (a cuboid and sphere) were considered. In the both cases, numerical results were presented for pressure data generated by three different point sources and good agreement with the exact solution was obtained in each case.

In Chapter 5, the method of superposition and its numerical application to solve both the forward Neumann problem, and the inverse NAH problem were detailed. The numerical results with different values of wavenumber k and for different numbers of terms in the superposition were demonstrated. The results showed fast convergence leading to smaller errors than the corresponding numerical experiments using the BEM in Chapter 2. The results of the numerical experiments for the MoS for the inverse problem of NAH demonstrated that the MoS can give more accurate solutions than the inverse BEM with faster computational times.

In Chapter 6, the theory of compressive sampling was introduced, together with the key concepts of sparsity and incoherence. Then a sparse regularization procedure using ℓ^1 optimization was applied to solve the three dimensional inverse NAH problem. The behaviour of the method, in terms of the error and the sparsity of the reconstructions, was investigated for different wavenumbers and different types of noisy synthetic pressure data. The results suggested important potential applications of the sparse superposition method in both source identification and in reducing the number of measurements necessary to obtain an accurate reconstruction.

In Chapter 7, the sparse method of superposition for NAH was validated by utilizing measured pressure data for a loudspeaker in a semi-anechoic chamber. First, the set up details of the experimental procedure for sampling the acoustic pressure in the near-field, and the use of the laser vibrometer to measure the normal velocity on the surface of the loudspeaker were provided. Then, the method of superposition was detailed for NAH in an infinite half-space. Next, numerical results for the sparse regularisation approach were calculated for synthetic acoustic pressure data to test the reformulated model before applying it to the measured data. After that, the method was applied at different frequencies between 100 Hz and 6800 Hz, and the results of the sparse regularisation procedure were compared

with the values measured using the laser vibrometer. The results that were obtained from the experimental work demonstrated that the sparse inverse method of superposition was reasonably accurate for frequencies up to and including the Nyquist rate, but above the Nyquist frequency the accuracy reduced greatly.

8.2 Further work

8.2.1 Extension to other radiating objects

In this work, we developed a sparse inverse MoS numerical model for near-field acoustic holography, where the acoustic field on the surface of a vibrating structure is recovered from measurements taken in the exterior field. The model was applied to a loudspeaker in a semi-anechoic chamber. The loudspeaker is a complex, composite structure and the results showed a good agreement with sufficient accuracy for identifying the vibrating region of the loudspeaker. However, the sparse inverse MoS approach is applicable to general three-dimensional geometries and so, this model can be extended to other radiating objects such as musical instruments, other types of loudspeaker and car engines, for example, where the identification of the source region of the radiated noise is of interest. These applications would require further experimental work as well as optimisation of the charge points and the model parameters.

8.2.2 Reconstruction beyond the Nyquist limit

Hald [47] uses a pseudo-random microphone array to obtain accurate reconstructions at frequencies above the Nyquist rate. The microphone array has partial rotational symmetry, but is only for planar measurements. The design of a suitable pseudo-random array in three dimensions is an open question. In Chapter 6,

we reported that randomising the measurement locations by randomly removing data points did not enhance our results. This suggests that achieving accurate reconstructions beyond the Nyquist limit for general three-dimensional structures is an interesting challenge for future work.

8.2.3 Time-domain NAH

In this thesis the frequency domain was used to investigate the performance of the method of superposition for the inverse NAH problem. An alternative is to consider time-domain near-field acoustic holography (TNAH) for non-stationary sound fields [67]. The inverse NAH problem in the time domain is different from the frequency domain (it is based on the acoustic wave equation instead of the Helmholtz equation), but similar methods can be applied [67]. The development of sparse NAH methods in the time-domain is therefore a significant area where new research can be performed.

8.2.4 Compressed modal equivalent point source method

The sparse inverse method of superposition developed in this thesis was concerned with identifying the sound source of a vibrating structure, when the vibrations were localised on one small area, such as the conic region of a loudspeaker. Recently, the compressed modal equivalent point source method (CMESM) has been proposed [48] to reconstruct the vibrational behaviour of a globally vibrating structure. This method is also based on compressive sensing, but instead uses the eigenvalue decomposition matrix as the basis for computing the source strengths. The method is based on the idea that even though the vibrations are non-local, the number of structural modes excited may be relatively small.

8.2.5 New sparse optimisation methods

In Chapter 6, we reconstruct the solution of the NAH problem using the MoS with sparse regularization methods. Hald [49] reports that there are many more compressive sampling optimisation methods that have been developed in the field of imaging science, which could be applied to NAH problems. These methods include (a) single-step iterative shrinkage thresholding algorithms, (b) two-step iterative shrinkage thresholding algorithms, which converge faster than the single step methods, and (c) Iteratively Reweighted Least Squares (IRLS). The latter method solves for each iteration a Tikhonov regularized problem, and more weight is given to the highest source amplitudes. The results in Hald [49] suggest that method (c) IRLS, will be the best method for the NAH problem using the inverse MoS. The IRLS method would therefore our starting point for further research in this direction.

Bibliography

[1] Williams G. and Maynard J.D. Holographic imaging without the wavelength resolution limit. *Phys. Rev. Lett.*, 45:554–557, 1980.

[2] Chappell D.J. and Harris P.J. A Burton-Miller inverse boundary element method for near-field acoustic holography. *J. Acoust. Soc. Amer.*, 126(1):149–157, 2009.

[3] Grande E.F. *Near-field acoustic holography with sound pressure and particle velocity measurments.* PhD thesis, University of Denmark, Department of Electrical Engineering, Technical University of Denmark, 2012.

[4] Valdivia N. P. and Williams E.G. *Numerical Methods for Near-Field Acoustic Holography over Arbitrarily Shaped Surfaces, Holography - Different Fields of Application.* Dr. Freddy Monroy (Ed.), ISBN: 978-953-307-635-5, 2011.

[5] Borgiotti G.V., Sarkissian A., Williams E.G., and Schuetz L. Conformal generalized near-field acoustic holography for axisymmetric geometries. *J. Acoust. Soc. Amer.*, 88:199–209, 1990.

[6] Wu S.F. Techniques for implementing near-field acoustical holography. *Sound & Vibration*, 44:12–16, 2010.

[7] Williams E.G., Maynard J.D., and Skudrzky E. Sound source reconstructions using a microphone array. *J. Acoust. Soc. Amer.*, 68:340–344, 1980.

[8] Williams E.G., Dardy H. D., and Fink R. G. Near-field acoustical holography using an underwater automated scanner. *J. Acoust. Soc. Amer.*, 78:789–798, 1985.

[9] Williams E.G. Continuation of acoustic near-fields. *J. Acoust. Soc. Amer.*, 113:1273–1281, 2003.

[10] Visser R. *A Boundary Element Approach to Acoustic Radiation and Source Identification*. PhD thesis, University of Twente, Enschede, Wageningen, The Netherlands, 2004.

[11] Hodgson T.H. and Underwood R.L. BEM computations of a finite length acoustic horn and comparision with experiment. In *in Computational Acoustics and its Environmental Applications*, pages 213–222, 1997.

[12] Pederson J.A. and Munch G. Driver directivity control by sound redistribution. In *in 113th Convention of Audio Engineering Society*, Los Angeles, California, October 2002.

[13] Juhl P.M. *The boundary element method for sound field calculations*. PhD thesis, Technical University of Denmark, 1993.

[14] Chandler-Wilde S.N., Langdon S., and Ritter L. A high-wavenumber boundary-element method for an acoustic scattering problem. *Philos. Trans. R. Soc. London A*, 362:647–671, 2004.

[15] Tsynkov S.V. Numerical solution of problems on unbounded domains: a review. *J. Applied Numerical Mathematics.*, 27:465 – 532, 1998.

[16] Zienkiewicz O.C. and Taylor R.L. *The Finite Element Method*, volume 1: The Basics. Butterworth Heinemann, Spain, 2000.

[17] Bettess P. Infinite elements. *International Journal for Numerical Methods in Engineering*, 11:53–64, 1977.

[18] Gardner B.K. and Bernard R.J. A noise source identification technique using an inverse Helmholtz integral equation method. *ASME J. Vib. Ac., Str. and Rel. Des.*, 110:84–90, 1988.

[19] Bai R. Application of boundary element method based acoustic holography to radiation analysis of sound sources with arbitrarily shaped geometries. *J. Acoust. Soc. Amer.*, 92:533–549, 1992.

[20] Kim B-K. and Ih J-G. On the reconstruction of the vibro-acoustic field over the surface enclosing an interior space using the boundary element method. *J. Acoust. Soc. Amer.*, 100:3003–3016, 1996.

[21] Wu S.F. and Zhao X. Combined Helmholtz equation least squares CHELS method for reconstructing acoustic radiation,. *J. Acoust. Soc. Amer.*, 112:179 – 188, 2002.

[22] Wu S.F. Hybrid near-field acoustic holography. *J. Acoust. Soc. Amer.*, 115:207–217, 2004.

[23] Amini S., Harris P.J., and Wilton D. T. *Coupled Boundary and Finite Element Methods for the Solution of the Dynamic Fluid-Structure Interaction Problem.* Springer-Verlag, Berlin, 1992.

[24] Burton A.J. The solution of Helmholtz' equation in exterior domains using integral equations. Technical Report NAC 30, National Physical Laboratory, Division of Numerical Analysis and Computing, Teddington, Middlesex, UK, January 1973.

[25] Rong J., Wen L., and Xiao J. An efficient method for evaluating BEM singular integrals on curved elements with application in acoustic analysis. In *Cornell University Library, Computational Engineering*, pages 1–19, 2013.

[26] Wang Z. and Wu S.F. Helmholtz equation least-squares method for reconstructing the acoustic pressure field. *J. Acoust. Soc. Amer.*, 102:2020–2032, 1997.

[27] Wu S.F. On the reconstruction of acoustic pressure fields using the Helmholtz equation least-squares method. *J. Acoust. Soc. Amer.*, 107:2511, 2000.

[28] Sarkissian A. Method of superposition applied to patch nearfield acoustic holography. *J. Acoust. Soc. Amer.*, 118:671–678, 2005.

[29] Valdivia N.P. and Williams E.G. Study of the comparison of the methods of equivalent sources and boundary elements for nearfield acoustic holography. *J. Acoust. Soc. Amer.*, 120:3694–3705, 2006.

[30] Koopman G.H., Song L., and Fahnline J.B. A method of computing acoustic field based on the principle of wave superposition. *J. Acoust. Soc. Amer.*, 86:2433–2438, 1989.

[31] Benthien W. and Schenck A. Nonexistence and nonuniqueness problems associated with integral equation methods in acoustics. *Computers and Structures*, 65(3):295–305, 1997.

[32] Leblanc A., Ing R.K., and Lavie A. A wave superposition method based on monopole sources with unique solution for all wave numbers. *Acta Acustica united with Acustica*, 96(1):125, 2010.

[33] Barnett A.H. and Betcke T. Stability and convergence of the method of fundamental solutions for Helmholtz problems on analytic domains. *J. Comput. Phys.*, 227(14):7003, 2008.

[34] Fairweather G. and Karageorghis A. The method of fundamental solutions for elliptic boundary value problems. *Adv.Comp. Math.*, 9(1-2):69, 1998.

[35] Fairweather G., Karageorghis A., and Martin P.A. The method of fundamental solutions for scattering and radiation problems. *Eng. Anal. Boundary Elem.*, 27(7):759, 2003.

[36] Williams E.G. Regularization methods for near-field acoustical holography. *J. Acoust. Soc. Amer.*, 110:1976–1988, 2001.

[37] Hansen P.C. Analysis of discrete ill-posed problem by means of the L-curve. *SIAM Journal on Numerical Analysis*, 34:561–580, 1992.

[38] Donoho D. L. Compressed sensing. *IEEE Trans. Inf. Theor.*, 52(4):1289–1306, April 2006.

[39] Romberg J. Candes E. and Tao. T. Robust uncertainty principles : Exact signal frequency information. 52:489–509, 2006.

[40] Yonina C. E. Gitta K. Mark A. D., Marco F. D. *Compressed Sensing: Chapter 1 - Introduction to compressed sensing.* Cambridge University Press, Online ISBN: 9780511794308, 2012.

[41] Chardon G., Daudet L., Pellot A., Ollivier F., Bertin N., and Gribonval R. Nearfield acoustic holography using sparsity and compressive sampling principles. *J. Acoust. Soc. Amer.*, 132(2):1521, 2012.

[42] Fernandez-Grande E. and Xenaki A. The equivalent sourse method as a spars signal reconstruction. In *in Proceeding of Inter-Noise*, pages 9–12, San Francisco, AC, August 2015.

[43] Hald J. Wideband acoustical holography. In *in Proceeding of Inter-Noise*, pages 16–19, Melbourne, Australia, 2014.

[44] Abusag N. M. and Chappell D. J. On sparse reconstructions in near-field acoustic holography using the method of superposition. *Journal of Computational Acoustics*, 24:1650009, 2016.

[45] Fernandez-Grande E., Xenaki A., and Gerstoft P. A sparse equivalent source method for near-field acoustic holography. *J. Acoust. Soc. Amer.*, 141(1):532–542, 2017.

[46] Fernandez-Grande E. and Xenaki A. Compressive sensing with a spherical microphone array. *J. Acoust. Soc. Amer.*, 139(2):EL45–EL49, 2016.

[47] Hald J. Fast wideband acoustcal holography. *J. Acoust. Soc. Amer.*, 139(4):1508–1517, 2016.

[48] Xu L. Zhang Y-B. Bi C-X., Liu Y. Sound field reconstruction using compressed modal equivalent point source method. *J. Acoust. Soc. Amer.*, 141(1):73–79, 2017.

[49] Hald J. A comparison of iterative sparse equivalent source methods for near-field acoustical holography. *J. Acoust. Soc. Amer.*, 143(6):3758–3769, 2018.

[50] Coulson C.A. and Jeffrey A. *Waves: A mathematical approach to the common types of wave motion.* Longman Group, London, 1977.

[51] Colton D. and Kress R. *Integral Equation Methods In Scattering Theory.* John Wiley and Sons, New York, 1983.

[52] O'Neill P.V. *Advanced Calculus, Pure and Applied*. Macmillan Publishing Co., New York, 1977.

[53] Atkinson K.E. *The Numerical Solution of Integral Equations of the Second Kind*. Cambridge University Press, Cambridge, UK, 1997.

[54] Weyl H. Ausbreitung elektromagnetischer wellen uber einem ebenen leiter. *Ann. Physik*, 60:481–500, 1919.

[55] Williams E.G. *Fourier Acoustics: Sound Radiation and Nearfield Acoustical Holography*. Academic Press, London, 1999.

[56] Cremer L., Heckl M., and Petersson B.A.T. *Structure-Borne Sound*. Springer-Verlag, Berlin, 2005.

[57] Fahy F. and Gardonio P. *Sound and Structural Vibration: Radiation, Transmission and Response*. Academic Press, London, 2nd edition, 2006.

[58] Kupradze V. D. and Aleksidze M. A. The method of functional equations for the approximate solution of certain boundary value problems. *USSR Computational Mathematics and Mathematical Physics*, 4:82–126, 1964.

[59] Mathon R. and Johnston R.L. The approximate solution of elliptic boundary value problems by fundamental solutions. *SIAM Journal on Numerical Analysis.*, 14:638–650, 1977.

[60] Golub H. G, Heath M., and Wahba G. Generalized cross-validation as a method for choosing a good ridge parameter. *Technometrics*, 21:215–223, 1979.

[61] Hansen P.C. Regularization tools version 4.0 for matlab 7.3. *Numer. Algorithms*, 46:189–194, 2007.

[62] Candes E. J. and Wakin M. B. An introduction to compressive sampling. *IEEE Signal Processing Magazine*, 25(2):21–30, March 2008.

[63] Grant M. and Boyd S. CVX: Matlab software for disciplined convex programming, version 2.1. `http://cvxr.com/cvx`, 2015.

[64] Chen S. S., Donoho D. L., and Saunders M. A. Atomic decomposition by basis pursuit. *SIAM Journal on Scientific Computing*, 20(1):33–61, 1998.

[65] Mingsian R. Bai, Jia-Hong Lin, and Kwan-Liang Liu. Optimized microphone deployment for near-field acoustic holography: To be, or not to be random, that is the question. *Journal of Sound and Vibration*, 329(14):2809 – 2824, 2010.

[66] Chappell D.J. and Abusag N.M. The method of superposition for near-field acoustic holography in a semi-anechoic chamber. In C. Constanda, editor, *Proceedings of Integral Methods in Science and Engineering 2016*, volume 2, Boston, USA, 2017. Birkhauser.

[67] Bi C-X. Zhang Y-B.-Xu L. Zhang, X-Z. Transient nearfield acoustic holography based on an interpolated time-domain equivalent source method. *J. Acoust. Soc. Amer.*, 130(3):1430–1440, 2011.

[68] Astolfi A. *Optimization: An introduction. Imperial college.* Lecture notes, London, 2006.

[69] Weber R. *Optimization: Convexity. Section 1.4.* Cambridge notes, Cambridge, 2010.

Appendix A

The Fourier transform in two-dimensions

Let $f : \mathbb{R}^2 \to \mathbb{C}$. The *Fourier transformation* in two-dimensions is defined to be the map $\mathcal{F} : f \to \tilde{f}$:

$$\tilde{f}(\mathbf{k}) = \int_{-\infty}^{\infty}\int_{-\infty}^{\infty} f(\mathbf{x})e^{-i\mathbf{k}\cdot\mathbf{x}}dx\,dy,$$

where here we denote $\mathbf{x} = [x,\ y]^T$ and $\mathbf{k} = [k_x,\ k_y]^T$. If this integral exists, then $\tilde{f} = \mathcal{F}f$ is called the *Fourier transform* of f. In the case when $\mathcal{F}$ is bijective, the inverse transformation $\mathcal{F}^{-1} : \tilde{f} \to f$ is given by

$$f(\mathbf{x}) = \frac{1}{4\pi^2}\int_{-\infty}^{\infty}\int_{-\infty}^{\infty} \tilde{f}(\mathbf{k})e^{i\mathbf{k}\cdot\mathbf{x}}dk_x dk_y.$$

Lemma A.1 *(Differentiation).*

Let $f \in \mathcal{S}(\mathbb{R}^2)$, the Schwartz space of rapidly decreasing functions- infinitely differentiable functions f with $\|f\|_{\boldsymbol{\alpha},\,\mathbf{p}} := \sup_{\mathbf{x}\in\mathbb{R}^2}\left|x^\alpha y^\beta \frac{\partial^p f}{\partial x^p}\frac{\partial^q f}{\partial y^q}\right| < \infty$ for all vectors of non-negative integers $\boldsymbol{\alpha} = [\alpha,\ \beta]$, $\mathbf{p} = [p,\ q]$. Then for any $m = 0, 1, 2, \ldots$ and $\forall\, \mathbf{k} \in \mathbb{R}^2$ we have,

$$\left(\mathcal{F}\left[\frac{\partial^m f}{\partial x^m}\right]\right)(\mathbf{k}) = (ik_x)^m(\mathcal{F}f)(\mathbf{k}) \quad \textit{and} \quad \left(\mathcal{F}\left[\frac{\partial^m f}{\partial y^m}\right]\right)(\mathbf{k}) = (ik_y)^m(\mathcal{F}f)(\mathbf{k}). \tag{A.1}$$

Proof.

We give the proof for $m = 1$. For $m > 1$ the result follows by induction. For the first result one uses integration by parts for the integral with respect to x, and for the second result one instead integrates by parts in the y integral. We detail the first case only since, given the above, the procedure for the second is entirely analogous. Writing out the definition for $m = 1$ gives

$$\begin{aligned}\left(\mathcal{F}\left[\frac{\partial f}{\partial x}\right]\right)(\mathbf{k}) &= \int_{-\infty}^{\infty}\int_{-\infty}^{\infty}\frac{\partial f}{\partial x}e^{-i(k_x x+k_y y)}dxdy \\ &= \int_{-\infty}^{\infty}e^{-ik_y y}\int_{-\infty}^{\infty}\frac{\partial f}{\partial x}e^{-ik_x x}dxdy \\ &= \int_{-\infty}^{\infty}e^{-ik_y y}\left(\left[f(\mathbf{x})e^{-ik_x x}\right]_{-\infty}^{\infty}+\int_{-\infty}^{\infty}f(\mathbf{x})(ik_x)e^{-ik_x x}dx\right)dy.\end{aligned}$$

The first term in the integration by parts vanishes since $f \in \mathcal{S}(\mathbb{R}^2)$ decays rapidly to zero as $x \to \pm\infty$. We are left with

$$\left(\mathcal{F}\left[\frac{\partial f}{\partial x}\right]\right)(\mathbf{k}) = ik_x\int_{-\infty}^{\infty}\int_{-\infty}^{\infty}f(\mathbf{x})e^{-i(k_x x+k_y y)}dxdy = ik_x(\mathcal{F}f)(\mathbf{k}). \quad \square$$

Corollary A.1 *(Gradient and Laplacian operators).*

Let $f \in \mathcal{S}(\mathbb{R}^2)$, then $\forall\, \mathbf{k} \in \mathbb{R}^2$ we have,

$$\left(\mathcal{F}[\nabla f]\right)(\mathbf{k}) = i\mathbf{k}(\mathcal{F}f)(\mathbf{k}) \quad \textit{and} \quad \left(\mathcal{F}[\triangle f]\right)(\mathbf{k}) = -|\mathbf{k}|^2(\mathcal{F}f)(\mathbf{k}). \tag{A.2}$$

Proof.

Since $\nabla f = \left[\frac{\partial f}{\partial x},\ \frac{\partial f}{\partial y}\right]^T$, then

$$\left(\mathcal{F}[\nabla f]\right)(\mathbf{k}) = \begin{pmatrix}\mathcal{F}\left[\frac{\partial f}{\partial x}\right](\mathbf{k}) \\ \mathcal{F}\left[\frac{\partial f}{\partial y}\right](\mathbf{k})\end{pmatrix} = \begin{pmatrix}ik_x(\mathcal{F}f)(\mathbf{k}) \\ ik_y(\mathcal{F}f)(\mathbf{k})\end{pmatrix} = i\mathbf{k}(\mathcal{F}f)(\mathbf{k}).$$

Since $\triangle f = \dfrac{\partial^2 f}{\partial x^2} + \dfrac{\partial^2 f}{\partial y^2}$, then

$$\begin{aligned}
(\mathcal{F}[\triangle f])(\mathbf{k}) &= \mathcal{F}\left[\frac{\partial^2 f}{\partial x^2}\right](\mathbf{k}) + \mathcal{F}\left[\frac{\partial^2 f}{\partial y^2}\right](\mathbf{k}) \\
&= -k_x^2(\mathcal{F}f)(\mathbf{k}) - k_y^2(\mathcal{F}f)(\mathbf{k}) \\
&= -(k_x^2 + k_y^2)(\mathcal{F}f)(\mathbf{k}) \\
&= -|\mathbf{k}|^2(\mathcal{F}f)(\mathbf{k}). \quad \square
\end{aligned}$$

Note that analogous results to the above lemma and corollary also hold for $f \in \mathcal{S}(\mathbb{R}^n)$, where n is any positive integer.

For $f, g \in L^1(\mathbb{R}^2)$, (i.e. $\int_{\mathbb{R}^2} |f(\mathbf{x})| d\mathbf{x}, \int_{\mathbb{R}^2} |g(\mathbf{x})| d\mathbf{x} < \infty$) define their (two-dimensional) *convolution* as:

$$(f * g)(\mathbf{x}) = \int_{\mathbb{R}^2} f(\mathbf{x} - \mathbf{x}')g(\mathbf{x}')d\mathbf{x}',$$

where (in this appendix) $\mathbf{x}' = [x',\, y']^T$.

Theorem A.1 *(Convolution).*

Let $f, g \in L^1(\mathbb{R}^2)$, then

$$\mathcal{F}(f * g) = (\mathcal{F}f)(\mathcal{F}g). \tag{A.3}$$

Proof.

$$\begin{aligned}
\mathcal{F}[(f * g)(\mathbf{x})](\mathbf{k}) &= \int_{\mathbb{R}^2} e^{-i\mathbf{k}\cdot\mathbf{x}} \left(\int_{\mathbb{R}^2} f(\mathbf{x} - \mathbf{x}')g(\mathbf{x}')d\mathbf{x}' \right) d\mathbf{x} \\
&= \int_{\mathbb{R}^2} e^{-i\mathbf{k}\cdot\mathbf{x}'} g(\mathbf{x}') \left(\int_{\mathbb{R}^2} e^{-i\mathbf{k}\cdot(\mathbf{x}-\mathbf{x}')} f(\mathbf{x} - \mathbf{x}')d\mathbf{x} \right) d\mathbf{x}' \quad (\text{set } \mathbf{u} = \mathbf{x} - \mathbf{x}') \\
&= \int_{\mathbb{R}^2} e^{-i\mathbf{k}\cdot\mathbf{x}'} g(\mathbf{x}') \left(\int_{\mathbb{R}^2} e^{-i\mathbf{k}\cdot\mathbf{u}} f(\mathbf{u})d\mathbf{u} \right) d\mathbf{x}' \\
&= \left(\int_{\mathbb{R}^2} e^{-i\mathbf{k}\cdot\mathbf{x}'} g(\mathbf{x}')d\mathbf{x}' \right) \left(\int_{\mathbb{R}^2} e^{-i\mathbf{k}\cdot\mathbf{u}} f(\mathbf{u})d\mathbf{u} \right) \\
&= (\mathcal{F}f)(\mathbf{k})(\mathcal{F}g)(\mathbf{k}). \quad \square
\end{aligned}$$

Note also that this theorem can be directly generalised to $f,\ g \in L^1(\mathbb{R}^n)$, for any positive integer n.

Appendix B

Exact solution for plane wave radiation from an infinite plate

In this appendix we will describe how to determine the acoustic radiation into the half-space $z > z_I$ due to a flexural plane wave travelling through a thin plate at $z = z_I$. This is a classical problem in structural acoustics and similar derivations can be found in many texts; see for example Chapter 7 of Ref. [56] or Chapter 3 of Ref. [57]. We consider a periodic cell of an infinite plate in the plane $z = z_I$ as described in Section 3.4. We implement this by choosing a square cell in the $x - y$ plane with $(x, y) \in [-1,\ 1] \times [-1,\ 1]$ and considering a flexural plane wave directed parallel to the y-axis with wavenumber $k_B = n\pi$ for some $n = 1, 2, 3, \ldots$. Assuming that this flexural wave has amplitude u_0 leads to an expression for the displacement of the plate in the z-direction (i.e. the normal displacement) of the form $u = u_0 e^{ik_B y}$. Since time-harmonic waves of angular frequency ω have a time-dependent factor of the form $e^{-i\omega t}$, then we may write the normal velocity as

$$v = -i\omega u_0 e^{ik_B y} = v_0 e^{ik_B y}. \tag{B.1}$$

Applying continuity of the wave vector at the surface of the plate $z = z_I$, then the radiated acoustic pressure wave can be expressed in the form

$$\phi = \phi_0 e^{ik_B y} e^{ik_z z}. \tag{B.2}$$

Substituting the expression (B.2) for the sound pressure into the Helmholtz equation (2.3) we find that

$$\begin{aligned} \triangle\phi + k^2\phi &= 0 - k_B^2\phi_0 e^{ik_B y} e^{ik_z z} - k_z^2\phi_0 e^{ik_B y} e^{ik_z z} + k^2\phi_0 e^{ik_B y} e^{ik_z z} \\ &= (k^2 - k_B^2 - k_z^2)\phi = 0, \end{aligned}$$

and hence for non-trivial solutions $\phi \not\equiv 0$, the square of the acoustic wavenumber must satisfy $k^2 = k_B^2 + k_z^2$. Assuming that k_B and k are specified by the problem then we use this relation to obtain $k_z = \sqrt{k^2 - k_B^2}$.

The linearised Euler's equation

$$\frac{\partial\Phi}{\partial\hat{\mathbf{n}}} = -\rho\frac{dV}{dt} \tag{B.3}$$

can now be applied to find a relation for the amplitude coefficient ϕ_0 in Eq. (B.2), given an assumed value for the amplitude of the plate vibration velocity v_0 (see Eq. B.1). Here ρ is the density of the acoustic medium, $\Phi(\mathbf{x}, t)$ is the time-dependent sound pressure and $V(\mathbf{x}, t)$ is the velocity. Again, we consider time-harmonic waves of angular frequency ω so that Φ and V can be expressed in the form $\Phi(\mathbf{x}, t) = \phi(\mathbf{x})e^{-i\omega t}$ and $V(\mathbf{x}, t) = v(\mathbf{x})e^{-i\omega t}$, respectively. Hence

$$\frac{dV}{dt} = -i\omega V,$$

and we obtain the following frequency domain form of the linearised Euler's equation

$$\frac{\partial\phi}{\partial\hat{\mathbf{n}}} = i\omega\rho v. \tag{B.4}$$

For the case of our flat plate structure, then

$$\frac{\partial \phi}{\partial \hat{\mathbf{n}}} = \frac{\partial \phi}{\partial z}$$

evaluated at $z = z_I$. Hence using this fact and substituting the plane wave expressions Eq. (B.1) and Eq. (B.2) into Eq. (B.4) at $z = z_I$ leads to

$$ik_z \phi_0 \, e^{ik_B y} \, e^{ik_z z_I} = i\omega \rho v_0 e^{ik_B y}. \tag{B.5}$$

Using that $k_z = \sqrt{k^2 - k_B^2}$ and rearranging for the acoustic wave amplitude term ϕ_0 yields

$$\phi_0 = \frac{\omega \rho v_0}{\sqrt{k^2 - k_B^2}} e^{-i\sqrt{k^2 - k_B^2} z_I}. \tag{B.6}$$

As a result, we can substitute this expression into Eq. (B.2) to give the radiated sound pressure at a point $\mathbf{x} = (x, y, z)$ in the half-space $z > z_I$ as

$$\phi(\mathbf{x}) = \frac{\omega \rho v_0}{\sqrt{k^2 - k_B^2}} e^{i\sqrt{k^2 - k_B^2}(z - z_I)} e^{ik_B y}. \tag{B.7}$$

Hence given a flexural plane wave in the infinite plate at $z = z_I$ described by Eq. (B.1), we may use the formula (B.7) to calculate the radiated acoustic wave in the half-space $z > z_I$.

Appendix C

Sampling theory and the Nyquist limit

In this appendix we will describe Shannon's sampling theorem and some related topics. Sampling is the process of converting a signal (e.g., a function of continuous time or space) into a numerical sequence (e.g., a function of discrete time or space). Shannon's sampling theorem states that:
If a function $x(t)$ contains no frequencies f higher than B Hertz, then $x(t)$ can be completely determined from its values at a set of points spaced $1/(2B)$ seconds apart.

In order to ascertain a sufficient sample-rate therefore we must take at least $2B$ samples per second. Equivalently, a sample rate r would lead a perfect reconstruction for a bandlimit $B < r/2$.

For a signal whose bandlimit is too high (or when there is no bandlimit), the reconstruction exhibits imperfections known as aliasing. The two thresholds, $2B$ and $r/2$ are respectively called the Nyquist rate and the Nyquist frequency. The theorem would also be applicable to the functions of space, such as in the case

of a digitized image or the sampling problems we meet in NAH. The only change would be the units of measure applied to t, r, and B.

C.1 Shannon's Proof

Assume that $X(\omega)$ is the one dimensional Fourier transform of $x(t)$, then

$$x(t) = \frac{1}{2\pi}\int_{-\infty}^{\infty} X(\omega)e^{i\omega t}d\omega = \frac{1}{2\pi}\int_{-2\pi B}^{2\pi B} X(\omega)e^{i\omega t}d\omega. \tag{C.1}$$

Note the analogy with two-dimensional Fourier transform discussed in Appendix A. The final expression follows since $X(\omega)$ is presumed to be zero outside the band $|f| = |\frac{\omega}{2\pi}| < B$. Letting

$$t = \frac{n}{2B}$$

where n is any positive or negative integer, we obtain

$$x\left(\frac{n}{2B}\right) = \frac{1}{2\pi}\int_{-2\pi B}^{2\pi B} X(\omega)e^{i\omega\frac{n}{2B}}d\omega, \tag{C.2}$$

where the left-hand expression gives the values of x at the sampling points. The integral on the right can be identified as the n^{th} coefficient in a Fourier-series expansion of the function $X(\omega)$ with the interval $-B$ to B as the period. Consequently, this means the values of samples $x(\frac{n}{2B})$ can be determined by the Fourier coefficients in a series expansion of $X(\omega)$. Therefore they determine $X(\omega)$, since $X(\omega)$ is zero for frequencies greater than B, and for lower frequencies $X(\omega)$ is determined if its Fourier coefficients are determined. Since $X(\omega)$ determines the original function $x(t)$ completely, then the original samples determine the function $x(t)$ completely.

C.2 Application to spatial sampling in nearfield acoustic holography

In this thesis we consider the solution of the Helmholtz equation (2.3) with wavenumber, or spatial frequency, $k = 2\pi/\lambda$, where λ is the wavelength. We are therefore interested in how the Nyquist sampling limit applies in the context of measurements of an acoustic field, which is assumed to satisfy the Helmholtz equation.

In particular, for a given measurement surface with a separation between subsequent measurement points of distance h, we would like to know the Nyquist sampling rate, and consequently the corresponding maximum wavenumber k_{nyq} for which the classical sampling theory tells us we should be able to reconstruct solutions of the Helmholtz equation. If the sampling distance is h, then the maximum spatial frequency will therefore be $k_{\text{nyq}} = 2\pi/(2h) = \pi/h$ m^{-1}.

Appendix D

Convex optimization

In this appendix we will give a brief introduction to some concepts related to optimization. Optimization is the act of obtaining the best possible result under a given set of circumstances [68]. The main target of all such procedures is either to maximize benefit or to minimize effort. The benefit or the effort can be expressed as a function of some design variables. Therefore, optimization is the process of obtaining the condition that gives the maximum or the minimum value of a function. In what follows, we only focus on function minimization because the minimum value of a function f is also the maximum value of the function $-f$. Consequently, without loss of generality, optimization can be taken to mean the minimization of a function.

There are several methods available for solving optimization problems efficiently. The minimization problems described above are known as mathematical programming problems, which are a branch of operations research. In the general mathematical programming problem of minimizing a function f over a set S, there may be local minima of f which are not the global minimum. It is usually difficult to find the global minimum when there are lots of local minima. However, if the

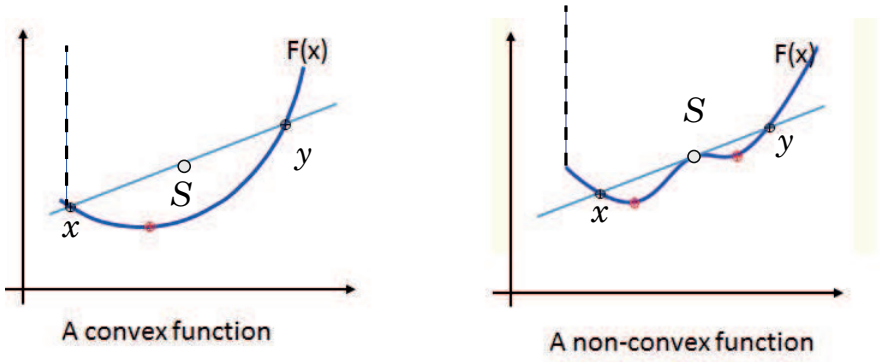

Figure D.1: Convex and non-convex functions on an interval.

function f is convex then the process is simplified considerably.

A set $S \subseteq \mathbb{R}^n$ is a convex set if $\lambda\mathbf{x} + (1-\lambda)\mathbf{y} \in S$ for all $\mathbf{x}, \mathbf{y} \in S$ and $0 \leq \lambda \leq 1$. In other words, the line segment joining $\mathbf{x}$ and $\mathbf{y}$ lies in S. A function $f : S \to \mathbb{R}^n$ is convex if the set above its graph is convex [69]. The difference between convex and non-convex functions is illustrated in Fig. D.1. Minimization of convex functions, or convex optimisation, is a much simpler problem than the general function minimization problems described above. This is because any local minimum of a convex function is also the global minimum [69], and so the problem is reduced to finding a single local minimum.